2013-03-25

Facile Synthesis and Improved Pore Structure Characterization of Mesoporous γ-Alumina Catalyst Supports with Tunable Pore Size

Baiyu Huang
Brigham Young University - Provo

Facile Synthesis and Improved Pore Structure Characterization of Mesoporous γ-Alumina Catalyst Supports with Tunable Pore Size

Baiyu Huang

A dissertation submitted to the faculty of
Brigham Young University
in partial fulfillment of the requirements for the degree of

Doctor of Philosophy

Brian F. Woodfield, Chair
Juliana Boerio-Goates
Calvin H. Bartholomew
Roger G. Harrison
Branton J. Campbell

Department of Chemistry and Biochemistry

Brigham Young University

March 2013

ABSTRACT

Facile Synthesis and Improved Pore Structure Characterization of Mesoporous γ-alumina Catalyst Supports with Tunable Pore Size

Baiyu Huang
Department of Chemistry and Biochemistry, BYU
Doctor of Philosophy

Mesoporous *γ*-alumina is the most extensively used catalysts support in a wide range of catalytic processes. The usefulness of *γ*-alumina relies on its favorable combination of physical, textural, thermal, and chemical properties. Pore structure properties are among the most important properties, since high surface area and large pore volume enable higher loading of active catalytic phases, while design of pore size and pore size distribution is critical to optimize pore diffusional transport and product selectivity. In addition, accurate determination of surface area (SA), pore volume (PV) and pore size distribution (PSD) of porous supports, catalysts, and nanomaterials is vital to successful design and optimization of these materials and to the development of robust models of pore diffusional resistance and catalyst deactivation.

In this dissertation, we report a simple, one-pot, solvent-deficient process to synthesize mesoporous *γ*-alumina without using external templates or surfactants. XRD, TEM, TGA and N_2 adsorption techniques are used to characterize the morphologies and structures of the prepared alumina nanomaterials. By varying the aluminum salts or the water to aluminum molar ratio in the hydrolysis of aluminum alkoxides, *γ*-alumina with different morphologies and pore structures are synthesized. The obtained alumina nanomaterials have surface areas ranging from 210 m^2/g to 340 m^2/g, pore volumes ranging from 0.4 cm^3/g to 1.7 cm^3/g, and average pore widths from 4 to 18 nm. By varying the alcohols used in the rinsing and gelation of boehmite/bayerite precursors derived from a controlled hydrolysis of aluminum alkoxides, the average pore width of the *γ*-aluminas can be tuned from 7 to 37 nm.

We also report improved calculations of PSD based on the Kelvin equation and a proposed Slit Pore Geometry model for slit-shaped mesopores of relatively large pore size (>10 nm). Two structural factors, α and β, are introduced to correct for non-ideal pore geometries. The volume density function for a log normal distribution is used to calculate the geometric mean pore diameter and standard deviation of the PSD. The Comparative Adsorption (α_s) Method is also employed to independently assess mesopore surface area and volume.

Keywords: mesoporous material, synthesis, solvent deficient method, γ-Al_2O_3, N_2 adsorption, surface area, pore volume, pore size distribution

ACKNOWLEDGEMENTS

I have enjoyed and appreciated the time I spent in our research group. I am fortunate to have the opportunity to working with a number of outstanding professors, who have had an invaluable impact on me both as a scientist and a person.

Thank you, Julie, for recruiting me as an international graduate student and letting me work on the new catalysis direction. The freedom and independence you gave me broadened my horizon and fostered my research ability. Thank you for all your guidance.

Thank you, Brian, for your mentoring and encouragement. Your broad knowledge catalyzed my progress in my research. Your passion and optimism inspired me when I encountered bottlenecks. I also want to thank you for teaching me how to be a good graduate student and a good father.

Thank you, Cal, for opening the world of catalysis for me. Thank you for countless hours you have devoted to tutoring me with your encyclopedical knowledge and experience. Thank you for your unexhausted patience and all your careful critiques of my work. From your pursuit of excellence and spirit of assiduous, I have learned how to become a better scientist and writer.

In addition to my advisors, I am grateful for the opportunity to work with a number of outstanding students in our group. Thank you, Stacey and Betsy, for your friendship and your help on the synthesis work and structural analysis, and for collaborating with me in a number of course work. Maryam, Jessie, Cameron, and Erika, thank you for your help in the lab.

Lastly and mostly, I owe my greatest gratitude to my wife, Rui. Thank you for your unswerving love and confidence in me. Thank you for your effort in raising Adeline. I couldn’t have accomplished anything without you.

Contents

Chapter 1

Introduction

Aluminum oxide, or alumina, is a material of great importance in our daily lives and in industry and is well known to have a number of polymorphs.[1, 2] The thermally stable form α-alumina, or corundum, is extensively used as a functional ceramic material in a wide range of applications due to its good electrical insulation, high mechanical and compressive strength, hardness, moderate thermal conductivity, high corrosion and wear resistance, good gliding properties, low density, high operating temperature, and relative chemical and biological inertness.[1-3] Transitional aluminas on the other hand, especially γ-alumina, are extensively used as catalyst supports due to their favorable textural properties and mechanical/thermal stability.[4] Some forms of mesoporous alumina are useful as catalysts or co-catalysts due to inherent Bronsted and/or Lewis acid site densities.

Mesoporous aluminas (MAs) are a relatively new class of tailored, high-surface-area support materials characterized by narrow mesopore size distributions and in selected cases ordered pore structures at the nanoscale.[5, 6] Average pore diameters are largely in the range of 3-7 nm, although pore diameters of 10-15 nm have also been prepared.[5, 6] Due to their higher specific surface area, the density of active sites in MAs is also higher; in addition to Bronsted and Lewis acid sites, these materials contain a relatively high density of basic sites relative to conventional aluminas. Basic sites enhance the strong interaction of metal oxides (used in oxidation and partial oxidation reactions) with the alumina support, thereby enhancing catalytic activity of oxide catalysts. Because of their higher surface areas, MAs can support higher loadings of metals, metal oxides, and metal sulfides while maintaining a high dispersion of the

active phase. For example, 30% Mo/MA is found to have higher activity than Mo supported on conventional aluminas.[7, 8] In the case of MAs with moderately large pores (e.g., 10-15 nm), the open pore structure also enhances the diffusion of reactant and product molecules. Therefore, MAs having highly desirable surface area and pore structural properties are likely to find application as supports or co-catalysts in a number of catalytic processes.

The key to developing and utilizing alumina materials lies in being able to efficiently produce such materials with desired properties. It is well known that the properties of aluminas are largely dependent on its preparation conditions.[1, 2, 5, 6, 9] Variations in synthetic route and corresponding experimental parameters can cause variations in the size, morphology, structure, and surface characteristics of resulting aluminas, thereby altering their physical properties and functionality. As a result, careful characterization of aluminas with different morphologies and structures are essential not only for determining their properties and appropriate applications, but also for understanding the chemistry involved in different preparation techniques.

This study reports the development of facile, solvent-deficient strategies to synthesize mesoporous aluminas with different morphologies and pore properties. We also report an improved calculation to characterize the pore structures of aluminas. In order to compare our method and understand the chemistry of alumina, it is important to provide an overview of the forms and types of aluminas and existing synthesis methods. Following this overview, a synopsis of the work reported in this dissertation is provided.

1.1 Nomenclature

The word “alumina” is derived from the word “Alumen” used by the Romans to describe materials with a styptic or astringent property, which may have included impure forms of aluminum sulfate and alum.[10] Currently, alumina is frequently used in the generic identification

Table 1.1 Nomenclature of crystallite aluminas [a]

Mineralogical name	Phase or form name					
	Symposium [b]	**Alcoa [c]**	**Haber**	**British**	**French**	**Other**
Hydroxides						
Gibbsite	$Al(OH)_3$	α-Al_2O_3•$3H_2O$	γ-$Al(OH)_3$	γ-Al_2O_3•$3H_2O$	-	-
Bayerite	$Al(OH)_3$	β-Al_2O_3•$3H_2O$	α-$Al(OH)_3$	α-Al_2O_3•$3H_2O$	-	-
Nordstrandite	$Al(OH)_3$	-	-	-	-	-
Bauxite	-	-	-	-	-	$Al(OH)_3$
Boehmite	AlOOH	α-Al_2O_3•H_2O	γ-AlOOH	γ-Al_2O_3•H_2O	-	-
Diaspore	AlOOH	β-Al_2O_3•H_2O	α-AlOOH	-	-	-
Aluminas						
	Chi	Chi	-	Chi + gamma	Chi + gamma	
	Eta	Eta	-	Gamma	Eta	
	Gamma	Gamma	Gamma	Delta	Gamma	
	Delta	Delta	-	Delta + theta	Delta	
	Theta	Theta	-	-	-	
	Kappa	Kappa, iota	-	Kappa + theta	Kappa + delta	
Corundum	Alpha	Alpha	Alpha	Alpha	Alpha	

a. Reproduced from Ref. 1.
b. Nomenclature from 1957 symposium in West Germany.
c. Nomenclature used by Aluminum Company of America (Alcoa).

of any of the several crystalline forms of aluminum oxides (Al_2O_3), aluminum hydroxides ($Al(OH)_3$), and aluminum oxide hydroxide (AlOOH).

Table 1.1 shows several different nomenclature systems for the various forms of aluminum hydroxides and oxides.[11] It is evident from Table 1.1 that due to historical origins and different language systems, different forms of aluminas may have similar-sounding names and a certain form of alumina may be assigned a Greek letter in one nomenclature system that refers to a different form in another system. It is difficult to say which system is most widely used and accepted. However, Alcoa, Symposium, and mineralogical nomenclatures and the mixture of these are commonly used in the United States. For the sake of clarity in this dissertation, the mineralogical definitions will be used for hydroxide forms and symposium identifications will be used for aluminum oxides.

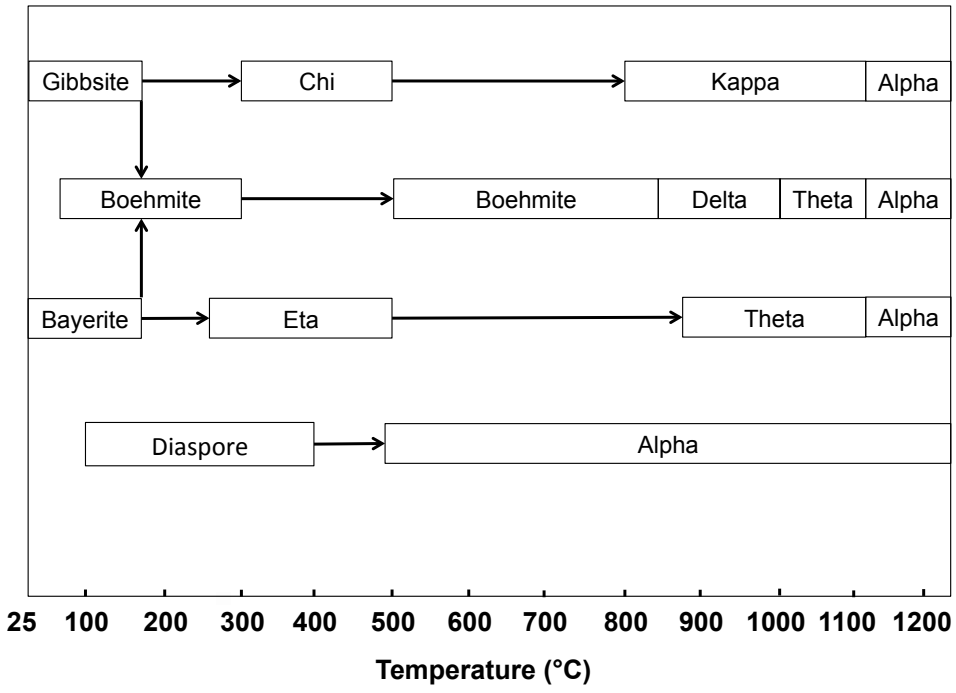

Figure 1.1 Decomposition sequences of alumina hydroxides, adapted from Ref. 2.

1.2 Forms and types aluminum hydroxides and oxy-hydroxides

Among the alumina family, only α-Al_2O_3 corundum is a stable oxide, while other derivatives, referred to as transitional aluminas, are considered to be metastable. They are formed upon the gradual dehydration of various hydroxides and oxyhydroxides,[12] and occur in the following transformation sequences shown in Figure 1.1. Therefore, it is important to understand the structures and properties of these aluminum hydroxides and oxyhydroxides.

1.2.1 Gibbsite

Gibbsite, as shown in Table 1.1, is one form of aluminum hydroxide, $Al(OH)_3$. It is the main constituent of bauxite found in tropical regions and North America. In industry, gibbsite is mainly produced via the Bayer process,[3] in which bauxites containing 40-70% of the aluminum minerals gibbsite, boehmite, or diaspore plus some other minor iron and titanium minerals, are digested with sodium hydroxide solution at 130 °C to 280 °C.

According to the reactions:

$$Al(OH)_3 + NaOH \rightleftarrows Al(OH)_4^- + Na^+ \qquad (1.1)$$

$$AlOOH + H_2O + NaOH \rightleftarrows Al(OH)_4^- + Na^+ \qquad (1.2)$$

aluminum minerals are leached and filtered. By reversing the temperature for Reaction 1.1 to 50 °C to 80 °C, precipitation of gibbsite occurs.

The gibbsite structure was first proposed by Pauling in 1930,[13] and subsequently confirmed by Megaw in 1934.[14] As shown in Figure 1.2, the basic structural elements of gibbsite are double layers of OH^- ions with Al cations occupying two-thirds of the octahedral interstices within the layers.[15] The hydroxides of adjacent layers are located opposite each other in a cubic packing arrangement. As a result, the packing sequence of OH^- ions in the direction perpendicular to the planes is AB-BA-AB-BA.

The gibbsite lattice is monoclinic, space group C_{2h}^5. The symmetry is derived from a hexagonal close packing of the hydroxide ions and can be described as a displacement of the double layers relative to each other in the direction of a-axis. However, triclinic gibbsite showing displacement along both a- and b-axis has also been reported.[16]

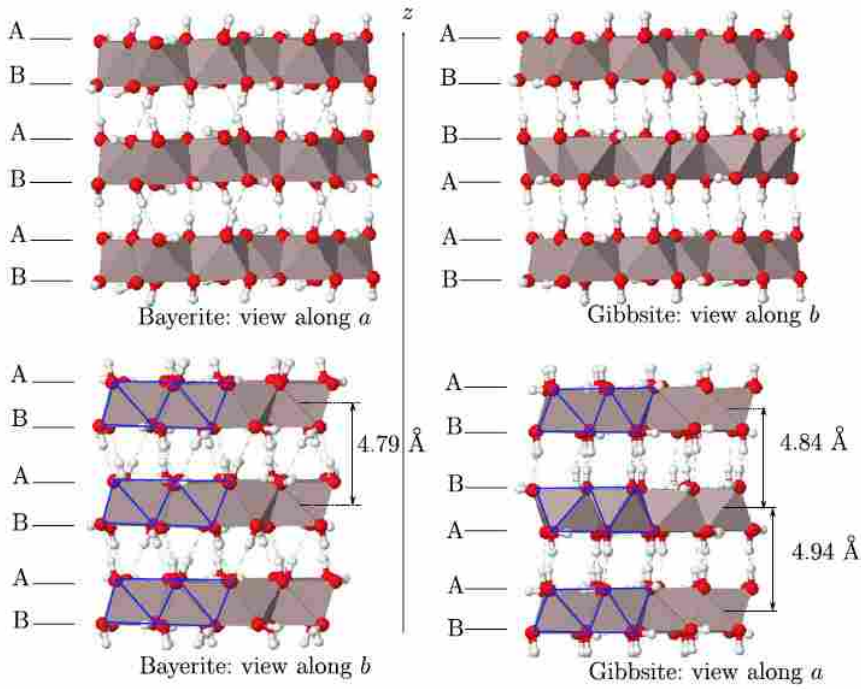

Figure 1.2 Structure of gibbsite and bayerite. (Red: Oxygen; White: Hydrogen). Adapted from Ref. 15.

Gibbsite is an important industry product. Most of the gibbsite is used as an intermediate to produce aluminum. Other applications are filler for paper, fireproofing and reinforcing agent for plastics and rubber, and raw material for the preparation of aluminum compounds.[2, 3]

1.2.2 Bayerite

Bayerite is another form of aluminum hydroxide. Unlike gibbsite, it is rarely found in natural minerals. Commercially available bayerite is mainly used for the preparation of catalysts and catalyst supports that required high purity alumina.

In the laboratory, bayerite can be prepared by immersing aluminum depassivated by amalgamation in pure water at room temperature,[17] neutralization of aluminum salt solutions by ammonium hydroxide below 50 °C, neutralization of sodium aluminate solution by carbon dioxide,[18] and hydrolysis of aluminum alkoxides with a large excess of water below 40 °C.[19]

As shown in Figure 1.2, the structure of bayerite is very similar to that of gibbsite. It is composed of the same basic layers of Al-OH octahedra. However, these layers are stacked in an AB-AB sequence, rather than AB-BA-AB-BA sequence observed in gibbsite, and linked by hydrogen bonds.

Due to the lack of large, single crystals of bayerite for structure determination, there is disagreement on the crystal system of bayerite. Montoro first proposed a brucite type of structure,[20] but a later study by Lippens concluded that the brucite structure is distorted since one-third of cation sites in bayerite are vacant.[12] According to later studies, the crystal system of bayerite is believed to be monoclinic.[21, 22]

1.2.3 Boehmite

Boehmite is the most important form of aluminum oxy-hydroxide, AlOOH. The mineral boehmite is often found together with gibbsite and bauxite deposited in the Tertiary and Upper Cretaceous age. However, in many bauxite of older Mesozoic strata, boehmite is the only constituent.[2] In industry, boehmite is an important precursor for activated aluminas used in the manufacture of catalysts and adsorbents.

In the laboratory, boehmite can be prepared by neutralization of aluminum salt solutions or sodium aluminate solution, or hydrothermally treating aluminum hydroxide at temperatures near or above 100 °C. It can also be obtained by heating coarse gibbsite or bayerite particles in air at temperatures ranging from 110 °C to 300 °C.[2]

As shown in Figure 1.3, the structure of boehmite consists of double layers in which the oxygen ions are arrayed in cubic stacking sequence and the symmetry is orthorhombic. However, there has been discussion about the actual positions of the hydrogens. Refinement studies by Hill et al. reported that the hydrogens are located asymmetrically between bonded oxygen ion pairs.[23] A subsequent study by Corbato et al. concluded that the hydrogens are located in two positions, being closer to one oxygen than to the corresponding oxygen in the next layer.[24] Given the information of the IR study by Russell et al., the space group of boehmite is C_{2v}^{12}.[25]

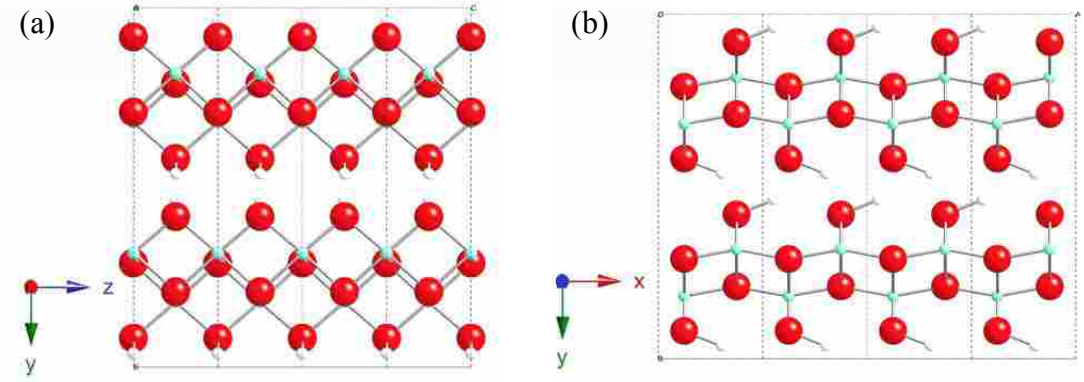

Figure 1.3 Views of the boehmite structure highlighting along the (a) x-axis and (b) z-axis. Red: Oxygen; White: Hydrogen; Green: Aluminum. Adapted from Ref. 2.

1.2.4 Other aluminum hydroxides and oxy-hydroxides

Gibbsite, bayerite and boehmite are the three most important forms of aluminum hydroxides and oxy-hydroxides. Other aluminum hydroxide and oxy-hydroxide types include nordstrandite, diaspora and tohdite. Due to their low abundance and relatively complicated preparation, they are not widely used in industry. There structural properties are listed in Table 1.2.

Table 1.2 Structural properties of aluminum hydroxides and oxy-hydroxides [a]

Phase	Formula	Crystal system	Space group	Molecules per unit cell	Unit axis length(nm)			Angle
					a	b	c	
Gibbsite	$Al(OH)_3$	Monoclinic	C_{2h}^5	4	0.8684	0.5078	0.9136	94° 34′
Gibbsite	$Al(OH)_3$	Triclinic	-	16	1.733	1.008	0.973	94° 10′ 92° 08′ 90° 00′
Bayerite	$Al(OH)_3$	Monoclinic	C_{2h}^5	2	0.5062	0.8671	0.4713	90° 27′
Nordstrandite	$Al(OH)_3$	Triclinic	C_1^1	2	0.5114	0.5082	0.5127	70° 16′ 74° 00′ 58° 28′
Boehmite	AlOOH	Orthorhombic	C_{2v}^{12}	2	0.2868	0.1223	0.3692	-
Diaspore	AlOOH	Orthorhombic	D_{2h}^{16}	2	0.4396	0.9426	0.2844	-
Tohdite	$5Al_2O_3 \cdot H_2O$	Hexagonal	C_{6v}^4	2	0.5576	-	0.8768	-

a. Adapted from Ref. 2

1.3 Forms of alumina

Based on the arrangement of oxygen anions, alumina structures can be divided into two categories (1) a face-centered cubic (fcc) structure and (2) a hexagonal close-packed (hcp) structure. The distribution of cations within each subgroup determines the different polymorphs.[2] The Al_2O_3 structures based on fcc packing include γ, η, δ and θ, whereas the Al_2O_3 structures based on hcp packing of oxygen include α, χ and κ.

1.3.1 Aluminas based on face-centered packed oxide anions

1.3.1.1 γ-alumina

γ-Al_2O_3 has been described as a defect spinel structure,[2] which are any of a class of minerals of general formulation $A_2B_2O_4$ which crystallizes in the cubic (isometric) crystal system. The oxide anions are arranged in a cubic close-packed lattice and the cations A and B occupying some or all of the octahedral and tetrahedral sites in the lattice.

Figure 1.4 shows the unit cell of γ-Al_2O_3. The commonly accepted structure of γ-Al_2O_3 is the ideal spinel (space group *F*d-3m), and it contains close packed oxygen ions in 32e Wyckoff positions, while 21 and a third aluminum cations are distributed over 16d octahedral and 8a tetrahedral sites.[26] Although a tetragonally distorted structure with a cation/anion ratio between 0.983 and 0.987 are reported by selected area diffraction (SAD),[12] the true symmetry of the tetragonally distorted structure is described by one of the tetragonal space groups, which is expected to be the maximal subgroup of *F*d-3m.

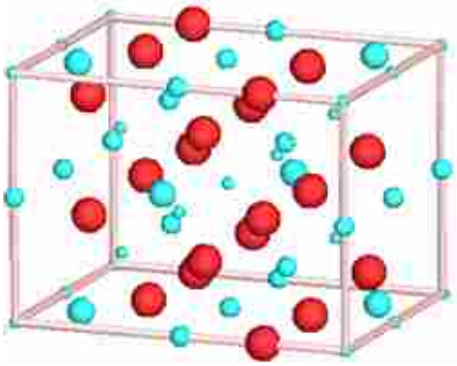

Figure 1.4 Unit cell of γ-alumina. (Red: Oxygen, Blue: Aluminum) Adapted from Ref. 26.

The greatest confusion surrounding γ-Al_2O_3 is the distribution of vacancies in the structure. Analysis of neutron and X-ray diffraction, and electron microscopy data show that the

vacancies are all placed on octahedral[27] or tetrahedral[28] sites, or distributed over both spinel site positions.[29, 30] Data of other methods also support these conclusions: the occupation of vacancies on octahedral sites is supported by several computational studies.[31, 32] Vacancy occupation on tetrahedral sites is supported by the nuclear magnetic resonance (NMR) study of John et al.[33] and the molecular dynamics simulation of Blonski and Garofalini et al.[34] However, the NMR and computational work of Lee et al.[35] showed vacancy distribution over both octahedral and tetrahedral positions. Based on powder XRD results, Shirasuka et al.[36] suggested that 62.5% of the aluminum ions occupy two 16-fold (16c and 16d) octahedral sites and assumed the remaining aluminum ions to be distributed equally over the eightfold and the 48-fold tetrahedral sites.

Among the transitional aluminas, γ-Al_2O_3 is the most widely used form in the filed of catalysis. It is mostly employed as catalyst supports due to its moderately high surface area, adequate pore volume for high metal loadings, tunable pore size, and high thermal stability over a wide range of temperatures. It is used, for example, as catalysts supports in alkene and benzene hydrogenation, catalytic reforming, hydrotreating, emission control, methanol synthesis, the water-gas-shift reaction, and oxychlorination.[1, 5] Because of its abundant Bronsted and/or Lewis acid sites, it can also be used as the active catalytic phase in applications requiring acid sites, e.g. alkylation, isomerization, polymerization, hydrogenation and Claus reaction to produce elemental sulfur.

1.3.1.2 *η*-alumina

η-Al_2O_3 also belongs to space group *F*d-3m. The structure of η-Al_2O_3 is almost identical to that of γ-Al_2O_3, except that no aluminum cations occupy the eightfold, tetrahedral sites.[37] SAD results reveal that η-Al_2O_3 formed from hydroxides is also tetragonally distorted, with a cation/anion ratio between 0.985 and 0.993.[12]

η-Al_2O_3 is also a material of great promise for catalytic applications such as petroleum refinement. For example, the exceptional activity of η-Al_2O_3 for isomerization of terminal olefins is attributed to the high acidity of the catalytically active sites,[38] which is also the reason why η-Al_2O_3 exhibits a higher catalytic activity than γ-Al_2O_3 in many reactions, including cracking of 2,4-dimethylpentane and isomerization of 1-pentene and p-xylene.[39]

1.3.1.3 δ-Alumina

δ-Al_2O_3 is a super-lattice of the spinel structure with ordered cation vacancies.[12, 37] The "super cell" of δ-Al_2O_3 consists of three spinel unit cells. However, two kinds of unit cells, tetragonal and orthorhombic, have been proposed for δ-Al_2O_3 obtained from different precursors.[12, 37] The former is derived from boehmite possesses a tetragonal δ unit cell with $a_\delta = b_\delta = a_\gamma$, and $c_\delta = 3a_\gamma$, whereas the latter has parameters $a_\delta = a_\gamma$, $b_\delta = 1.5a_\gamma$, and $c_\delta = 2a_\gamma$.[40]

Repelin and Husson et al. describe δ-Al_2O_3 as a P-4m2 space group, which contains 80 ions with 4 cation vacancies randomly distributed over octahedrally coordinated sites,[41] but no other results have been published to support the existence of this structure. $P2_12_12_1$ space group was also proposed for δ-Al_2O_3 by a convergent-beam electron diffraction (CBED) study.[42] However, no information was provided for the specific ionic positions.

In industry, δ-Al_2O_3 is mostly used as reinforcement in metal matrix composites. [43, 44]

1.3.1.4 θ-Alumina

As shown in Figure 1.5, θ-Al_2O_3 is a well-characterized structure with the monoclinic space group $C2/m$ and the aluminum cations are distributed equally between tetrahedral and octahedral sites.[45] It

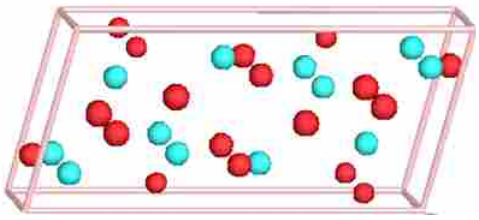

Figure 1.5 Unit cell of θ-alumina. (Red: Oxygen, Blue: Aluminum) Adapted from Ref. 45.

has been reported to be multiple twinned, mainly on the (001) plane. [46] Although the true symmetry of θ-Al_2O_3 is monoclinic, this phase may also appear orthorhombic as the result of polysynthetic twinning.[47]

1.3.2 Aluminas based on hexagonal close-packed oxygen anions

1.3.2.1 α-alumina

α-Al_2O_3 is well defined as having trigonal symmetry with rhombohedral Bravais centering (space group *R*-3c). The primitive cell contains two formula units of aluminum oxide. The oxygen ions form a slightly distorted hexagonal close-packed structure whereas aluminum ions fill two-thirds of the octahedral interstices. The oxygen anions occupy 18c Wyckoff positions with coordinates x, 0, 1/4 (x = 0.306), whereas the aluminum cations are at 12c positions with coordinates 0, 0, z (z = 0.347).[48] The aluminum cations are displaced along the [001] direction toward the neighboring empty octahedral sites. The hexagonal parameters for α-Al_2O_3 are c = 1.297 nm and a = 0.475 nm, with cation/anion ratio of 2.73.[49] As shown in Figure 1.6, the lattice roughly consists of alternating layers of oxygen and aluminum ions.[50]

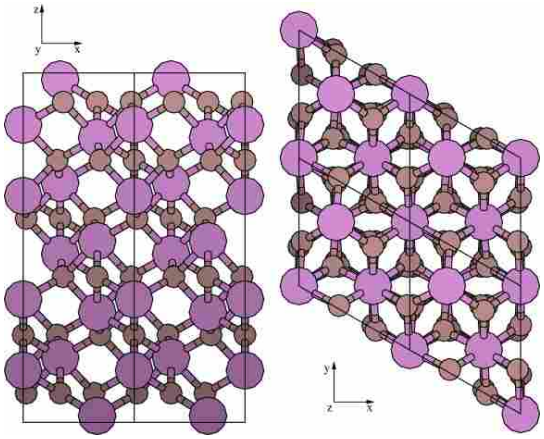

Figure 1.6 Structure of α-alumina. view of plane (0 1 -1 0) on the left and (0 0 0 1) on the right side. (Red: Aluminum, Grey: Oxygen) Adapted from Ref. 50.

1.3.2.2 χ-alumina

Three different structures have been proposed for χ-Al_2O_3. Stumpf et al.[51] suggested that χ-alumina has a cubic unit cell with a lattice parameter of 0.795 nm, whereas other researchers proposed hexagonal unit cells with either a = 0.556 nm and c = 1.344 nm (space group *P*6/mm)

or a = 0.557 nm and c = 0.864 nm.[52] It is reported that hexagonal χ-Al_2O_3 possesses a layered structure in which the hexagonal arrangement of oxygen is inherited from the structure of gibbsite and aluminum occupies octahedral sites within the hexagonal structure.[2] However, it is not clear whether all of the three exist.

1.3.2.3 κ -alumina

κ-Al_2O_3 is widely prepared in chemical vapor deposition (CVD) technology. Its structure was determined by convergent-beam electron diffraction (CBED).[53] The results showed that the structure is orthorhombic and the space group is $Pna2_1$ (lattice parameters: a = 0.469 nm, b = 0.818 nm, c = 0.887 nm). A study by Ollivier et al. concludes that the aluminum ions to be inserted between the oxygen layers in both octahedral and tetrahedral positions are in a 3:1 ratio,[54] which was confirmed by first principles calculations based on periodic density functional theory (DFT) with a plane wave basis set. [55]

1.4 Preparation of alumina

1.4.1 Al_2O_3-H_2O systems

Aluminum hydroxides are amphoteric. They are soluble in both strong bases and strong acids. The species in solution are mainly AlO_2^- anions at pH > 9, whereas $Al(H_2O)_6^{3+}$ is present at pH < 4. In the pH range between 4 and 9, precipitation of aluminum hydroxide takes place and produces a poorly ordered solid phase.

The precipitation of aluminum hydroxide often occurs in water or a mixture of water and an organic solvent. The freshly precipitated aluminum hydroxides and/or aluminum oxy-hydroxides often contain a significant amount of solvent molecules, forming a wide variety of two-phase systems that are referred to as alumina gel or gelatinous aluminas. Depending on the preparation method, the solid may be present as discrete particles ranging from a few nanometers

to micrometers, or it forms chemically bonded, three-dimensional polymeric networks. The formation of the gelatinous alumina can be described as polymerization/condensation of $Al(H_2O)_6^{3+}$ octahedrals.

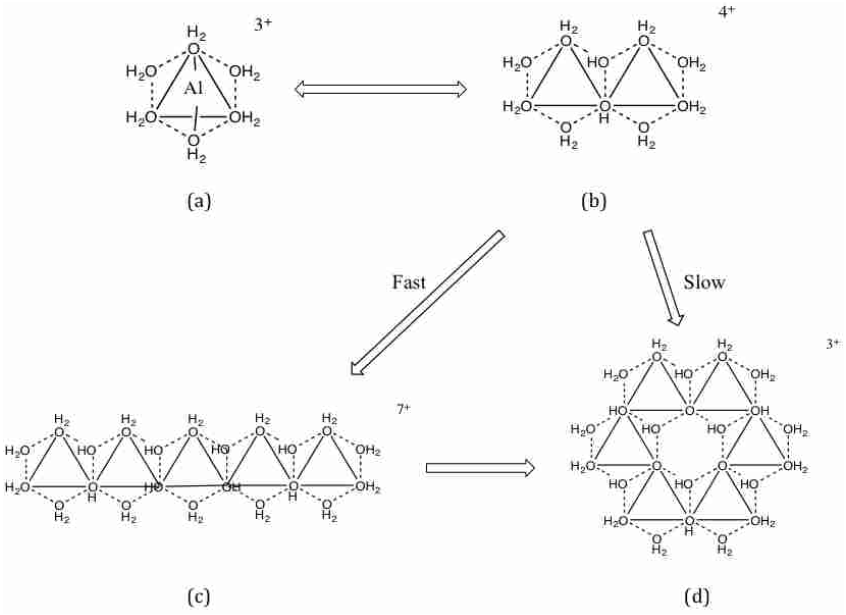

Figure 1.7 Polymerization of gelatinous alumina. (a) $Al(H_2O)_6^{3+}$, (b) $2Al(OH)(H_2O)_5^{2+}$, (c) chain-like boehmite polynuclear complex (d) plate-like boehmite polynuclear complex. Adapted from Ref. 2.

Due to polarization of the water molecules by Al^{3+} ions,[56] proton loss occurs as follows:

$$Al(H_2O)_6^{3+} \rightleftarrows 2Al(OH)(H_2O)_5^{2+} + H^+ \qquad (1.3)$$

The resultant complex will dimerize by condensation

$$2Al(OH)(H_2O)_5^{2+} \rightleftarrows Al(OH)_2(H_2O)_8^{4+} + 2H_2O \qquad (1.4)$$

As illustrated in Figure 1.7, further condensation/polymerization can proceed in one of two ways: (1) forming chains by linking octahedra through common edges or (2) forming hexagonal rings which further coalesce to large polynuclear complexes.[2] According to Baker et al.,[57] "fast" polymerization resulting from high concentration of the hydroxyl intermediate leads

to chain-like agglomeration whereas "slow" polymerization due to low hydroxide concentration or aging results in sheet-like aggregation.

The degree of crystalline order, particle size, and chemical composition of the gelatinous aluminas are determined by several factors, including temperature, rate of precipitation, final pH, ionic composition, concentration of starting solution, and aging time. So far, the most common aluminum hydroxides and oxy-hydroxides produced are gibbsite, bayerite and boehmite.

1.4.2 Current synthesis of mesoporous alumina

Preparations of mesoporous aluminas (MAs) have evolved from methods used in the synthesis of mesoporous molecular sieves and silicas using triblock copolymers as structure-directing agents.[58] For example, Huo et al. extended the method developed for synthesis of mesoporous molecular sieves to synthesis of non-silica-based materials.[59, 60] Subsequently, a number of methods were developed for synthesis of MAs. These can be divided into two categories: (1) Primary Synthesis, involving reaction of organic or inorganic Al-containing compounds with excess water or an aqueous base to precipitate a hydroxide or aluminum hydrate such as boehmite or bayerite; and (2) Secondary Synthesis, involving sol-gel formation from an aluminum hydrate (typically boehmite) followed by dehydration/calcination to γ- and other transitional-aluminas.

Methods for preparing mesoporous aluminas with unusually high surface areas (300-700 m^2/g), large pore volumes (0.6-1.6 cm^3/g), and narrow pore-size distributions have been summarized in recent representative reviews.[5, 6] They typically involve the *in-situ* sol-gel processing of aluminum ions from an aluminum salt or alkoxide to a crystalline aluminum hydroxide ($Al(OH)_3$ or bayerite) or oxide hydroxide (AlOOH or boehmite) in the presence of templates or structure-directing agents (SDAs) such as surfactants and large molecular weight

polymers through scaffolding,[61, 62] nanocasting,[63, 64] hydrothermal treatment,[65] precipitation,[66] and cation-anion double hydrolysis.[67, 68]

Table 1.3 Types of surfactants and interaction between surfactant head group and inorganic precursor

Surfacant type	Interaction type	Interaction pathway [a]	Examples
Cationic S^+	Electrostatic interaction	S^+I^-	CTAB,CPC, N-Dodecylpyridinium chloride
		$S^+X^-I^+$	
Anionic S^-	Electrostatic interaction	S^-I^+	alkylbenzene sulfonates, laurylsulfate, di-alkyl sulphosuccinate
		$S^-M^+I^-$	
Neutral S^0/N^0	H-bonding interaction	S^0I^0	Pluronic P123, F127
		N^0I^0	

a. S is the surfactant, I is the inorganic phase and X is the mediating anionic species, M is intermediate cation, S^0 is neutral amine, I^0 is hydrated inorganic oligomer and N^0 is non-ionic template. Adapted from Ref.69.

Depending upon the dissociation of surfactant molecule in aqueous media, there are three types of amphiphilic surfactants: cationic surfactants, anionic surfactants, and non-ionic surfactants. Based on the surfactant type and the interaction between metal and surfactant, six different synthesis pathways have been readily employed to prepare mesoporous materials under a wide range of pH, temperatures, and surfactant nature and their concentrations.[69] As listed in Table 1.3, the six pathways are S^+I^-, S^-I^+, $S^-M^+I^-$, $S^+X^-I^+$, S^0I^0 and N^0I^0, where S is the surfactant, I is the inorganic phase and X is the mediating anionic species, M is intermediate cation, S^0 is neutral amine, I^0 is hydrated inorganic oligomer and N^0 is non-ionic template.

1.4.2.1 Cationic surfactants

Although S^+I^- pathways have been widely used for the preparation of mesoporous silica, it is not the case in the synthesis of mesoporous alumina. For the synthesis carried out in aqueous solution at pH below the isoelectric point of alumina or by hydrolysis of aluminum alkoxides in organic media, the inorganic species in solution would be cationic. Therefore, $S^+X^-I^+$ pathways are more applicable.

The first reported synthesis of aluminum hydroxide-cationic surfactant mesophases was carried out by Acosta et al.[70] In their study, 20-50 wt% of alkyltrimethylammonium bromide was used as cationic surfactant in an aqueous solution. Aluminum chloride was used as starting material and precipitated by adding urea at pH close to 7. After removal of the surfactant at 450 °C in nitrogen and calcination in air, poorly crystalline mesoporous aluminas were obtained. In addition, the difference in the textural properties (surface area, pore volume and pore size) between the sample preparation with and without surfactant is very small, indicating alkyltrimethylammonium cation is not a good SDA. Subsequently, atrane complexes were used to improve the properties of aluminas obtained using cetyltrimethylammonium bromide (CTAB).[71, 72] Triethanolamine (TEA) was added to form complexes with aluminum *sec*-butoxide to control the hydrolysis reaction. By varying the water/TEA ratio, the pore size of the alumina was adjusted from 3.3 to 6.0 nm. The porosity was attributed to the voids created by the agglomeration of small alumina crystallites. Hydrothermal treatment was also reported for the synthesis of mesoporous alumina using cationic surfactants (CTAB) in the presence of alcohol using aluminum *sec*-butoxide as starting material.[65, 73, 74] Pore sizes of the obtained aluminas were reported to be controlled by adding formamide.[74]

1.4.2.2 Anionic surfactants

When anionic surfactants (S^-) are used, the reaction pathway can be S^-I^+ or $S^-M^+I^-$, depending on the pH. At pH < 5, a mesophase with direct interaction between the surfactant (S^-) and alumina species ($Al(H_2O)_6^{3+}$) was obtained. At pH > 8, cations (usually Na^+) are incorporated at the interface between the surfactant and anionic aluminate species.

The synthesis of mesoporous alumina using anionic surfactants was first carried out by precipitation of aluminum hydroxide.[6] An an aqueous solution of aluminum nitrate was added to

NaOH aqueous solutions containing alkylphosphates.[6] Subsequently, Yada et al. employed urea to obtain aluminum hydroxide from aluminum nitrate solutions containing sodium dodecyl sulfate (SDS). After surfactant removal with ethanol or acetone, the mesoporous structure of the obtained aluminas collapsed.[75] Later studies showed a strong interaction between the sulfate head groups and the alumina framework.[76, 77] The collapse of the mesoporous structure was attributed to the low Al-O-Al connectivity due to the high surfactant content (55 wt% of SDS).[78]

Valange et al. reported several synthesis strategies in aqueous mediums using different aluminum sources (aluminum nitrate and Al_{13} Keggin polycations) and anionic surfactants (carboxylic acids).[79] Aluminas with surface areas ranging from 110 to 810 m^2/g, pore volumes ranging from 0.08 to 0.89 cm^3/g and pore sizes ranging from 1 to 6 nm, were obtained. However, the pore structure collapses after calcination at 450 °C for 2 hours due to the strong interaction between sulfate groups and the positive charges of the alumina surface.

Aluminum alkoxides are also used in the preparation of mesoporous aluminas with anionic surfactants. Vaudry et al. used C_5 to C_{18} carboxylic acid surfactants to prepare mesoporous aluminas by hydrolysis of aluminum alkoxide in low molecular weight alcohol solutions.[80] The obtained aluminas showed a relatively narrow pore size distribution. Ray et al slightly modified the procedures by adding an aging step at 100 °C, and the surface area of the obtained alumina was increased from 360 to 410 m^2/g. Subsequently, by templating the aluminum hydroxide precursors with lauric and stearic acid in *n*-propanol solution, Cejka obtained aluminas with surface areas as high as 475 m^2/g and a pore size around 3.5 nm.[81-83] The effect of pH and water content on the textural properties of mesoporous aluminas using stearic acid was also reported.[84] Aluminas with relatively high surface area (370 to 390 m^2/g) and tunable pore sizes (3.5 to 7.7 nm) were obtained.

1.4.2.3 Non-ionic surfactants

Bagshaw et al. first reported the synthesis of non-inoic surfactant aluminas and was published in the middle 1990's.[85, 86] Since then, commonly used non-ionic surfactants are diblock R-$(EO)_n$ copolymers (Tergitol, Igepal, Triton) and triblock $(EO)_n(PO)_m(EO)_n$ copolymers (Pluronics). The former contains a hydrophilic poly (ethylene oxide) and a hydrophobic hydrocarbon moiety (R), while the latter contains a hydrophobic poly (propylene oxide) chain linked to two hydrophilic poly (ethylene oxide) chains. It is expected that the oxygen atoms of the PEO chain hydrogen bond with hydroxyl group on the aluminum hydroxide surface or even with bare aluminum having available coordination sites.[6] Aluminas with surface areas ranging from 420 to 535 m^2/g, pore volumes from ca. 0.2 to 0.7 cm^3/g and pore size from 2 to 5 nm were prepared by hydrolysis of aluminum alkoxides in *sec*-butanol solutions after calcination at 500 °C for 4 hours.[87-90] Compared to aluminas prepared from ionic surfactants, these non-ionic surfactant assisted aluminas exhibited more ordered pore structures and better thermal stability. It is reported that the thermal treatments in these syntheses have enormous influence on the final textural properties of the alumina. First, the surfactant content in these studies were relatively high and the combustion of these surfactants are highly exothermic, ramp rate and calcination temperature should be carefully controlled to avoid temperature overshoot and structure collapse. Second, further condensation of Al-O-Al bridges during the thermal treatment is critical to obtain stable mesoporous alumina.[6]

It is reported that the use of long chain *n*-alkylamines can increase the micelle size and therefore enlarge the pore size of siliceous molecular sieve MCM-41 since long chain *n*-alkylamines can penetrate into the interlayer space of layered compounds.[91] This strategy has also been employed in the synthesis of mesoporous aluminas. Gonzalez-Pena et al. synthesized mesoporous aluminas by hydrolyzing aluminum *sec*-butoxide in *sec*-butanol solutions in the

presence of amine and Triton type of surfactants.[92] Platelet-like alumina crystallites were observed and the pore size could be controlled from 3 to 8 nm by varying the surfactant content, which hydrogen bonds with aluminum hydroxides to limit their growth. Aluminas with larger pore sizes (up to 14 nm) were prepared by Yang et al. using the triblock copolymer Pluronic P123 as SDA.[93] Mesoporous aluminas with an ordered pore arrangement was first reported by Somorjai et al.[94] Aluminum *tert*-butoxide in a mixture of concentrated HCl and ethanol was mixed with Pluronic P123 in ethanol at 40 °C. The obtained alumina sol was then aged at 40 °C for 3 days and calcined at 400 °C. Hexagonal arrangement of mesopore channels with a pore diameter around 7 nm was observed.

1.4.2.4 Summary

As stated above, mesoporous aluminas with a wide range of pore properties were synthesized using a variety of SDAs under varying conditions. These methods, however, have several limitations: (1) these synthesis routes require use of toxic or expensive external structure-directing surfactants or templates, including cationic alkyltrimethylammonium (CTAB),[95] anionic lauric acid and steric acid,[84, 96] non-ionic diblock or triblock polymers,[62, 97] with water or alcohol as solvents. (2) These processes are often laborious and time-consuming, i.e., they generally consist of 10-15 steps, including reactions, digestion, washings, and separations such as solvent extraction, hydration, sol and gel formations, dehydration, drying and calcination. Since each step requires sophisticated control of experimental conditions over a significant time period, completion of the overall process may require many hours or even several days. Such complex, multi-day, labor-intensive synthesis processes, involving the use of toxic, expensive surfactants or templating agents and copious amounts of a solvent, are unlikely to find commercial application. If, however, a simple but cost effective synthetic methodology for

preparation of a high surface area mesoporous alumina with a narrow pore size distribution were developed, commercial development would be likely to proceed.

1.5 Overview of the dissertation

The dissertation is comprised of 6 chapters. Chapter 1 contains background information on the structure and properties of different types and forms of aluminum hydroxides, oxy-hydroxides and aluminum oxides. A review of the synthesis of mesoporous aluminas is also included. Chapter 2 describes the apparatus and experimental methods used to determine the structure and textural properties of the aluminas prepared in this dissertation. In Chapter 3, improved calculations of pore size distribution (PSD) based on the Kelvin equation and a proposed Slit Pore Geometry model for slit-shaped mesopores of relatively large pore size (>10 nm) are reported.

The next three chapters are focused on the synthesis of mesoporous γ-alumina catalyst supports. Chapter 4 reports a general one-pot, solvent-deficient synthesis of mesoporous aluminas using different aluminum sources without SDAs. Chapter 5 reports and discusses the control of morphology and pore structure of the aluminas by varying the water content in the controlled hydrolysis of aluminum alkoxides. In Chapter 6, we report another method to synthesize alumina catalyst supports with controlled morphology and pore structure. By varying the alcohols used in the rinsing and gelation of boehmite/bayerite precursors derived from a controlled hydrolysis of aluminum alkoxides, average pore sizes of γ-aluminas can be tuned from 7 to 37 nm.

References

1. Oberlander, R., Aluminas for catalysts-their preparation and properties. *Applied Industrial Catalysis* **1984,** *3*, 63-112.

2. Wefers, K.; Misra, C., Alcoa technical paper no.19. **1987**.

3. Hudson, L. K.; Misra, C.; Perrotta, A. J.; Wefers, K.; Williams, F. S., Aluminum oxide. In *Ullmann's encyclopedia of industrial chemistry*, Wiley-VCH Verlag GmbH & Co. KGaA: 2000.

4. Morterra, C.; Magnacca, G., A case study: Surface chemistry and surface structure of catalytic aluminas, as studied by vibrational spectroscopy of adsorbed species. *Catal. Today* **1996,** *27* (3-4), 497-532.

5. Cejka, J., Organized mesoporous alumina: Synthesis, structure and potential in catalysis. *Appl. Catal., A* **2003,** *254* (2), 327-338.

6. Marquez-Alvarez, C.; Zilkova, N.; Perez-Pariente, J.; Cejka, J., Synthesis, characterization and catalytic applications of organized mesoporous aluminas. *Catalysis Reviews-Science and Engineering* **2008,** *50* (2), 222-286.

7. Chianelli, R. R.; Daage, M.; Ledoux, M. J., Fundamental studies of transition-metal sulfide catalytic materials. *Adv. Catal.* **1994,** *40*, 177-232.

8. Lacroix, M.; Boutarfa, N.; Guillard, C.; Vrinat, M.; Breysse, M., Hydrogenating properties of unsupported transition metal sulfides. *J. Catal.* **1989,** *120* (2), 473-7.

9. Bartholomew, C. H.; Farrauto, R. J., *Fundamentals of industrial catalytic processes*. 2 ed.; Wiley-AICHE: 2005.

10. Beckmann, J., *A history of inventions, discoveries, and origins*. 4 ed.; H.G. Bohn: London, 1846.

11. Gitzen, W. H., *Alumina as a ceramic material*. 1 ed.; Wiley-American Ceramic Society: 1970.

12. Lippens, B. C.; de Boer, J. H., Study of phase transformations during calcination of aluminum hydroxides by selected area electron diffraction. *Acta Crystallogr.* **1964,** *17* (10), 1312-21.

13. Pauling, L., Structure of the micas and related minerals. *Proc. Natl. Acad. Sci. U. S. A.* **1930,** *16*, 123-9.

14. Megaw, H. D., The crystal structure of hydrargillite, $Al(OH)_3$. *Z. Kristallogr., Kristallgeom., Kristallphys., Kristallchem.* **1934,** *87*, 185-204.

15. Demichelis, R.; Civalleri, B.; Noel, Y.; Meyer, A.; Dovesi, R., Structure and stability of aluminium trihydroxides bayerite and gibbsite: A quantum mechanical ab initio study with the crystal06 code. *Chemical Physics Letters* **2008,** *465* (4–6), 220-225.

16. Saalfeld, H., The structures of gibbsite and of the intermediate products of its dehydration. *Neues Jahrb. Mineral., Abh.* **1960,** *95*, 1-87.

17. Schmah, H., Preparation, alkaline properties, aging, and solubility of extremely pure aluminum hydroxide and application in chromatography. *Z. Naturforsch.* **1946,** *1*, 322-3.

18. Fricke, R.; Wullhorst, B., Energy differences of different modifications of crystalline beryllium and aluminum hydroxides and heats of formation of crystalline zinc and beryllium hydroxides. *Z. Anorg. Allg. Chem.* **1932,** *205*, 127-44.

19. Fricke, R.; Jockers, K., Porosity and surface of various aluminum hydroxides and oxides. *Z. Anorg. Allg. Chem.* **1951,** *265*, 41-8.

20. Montoro, V., *Ricerca Sci. Prog. Teen. Roma,* **1942,** *13*, 565-571.

21. Rothbauer, R.; Zigan, F.; O'Daniel, H., Refinement of the structure of bayerite, $Al(OH)_3$. Proposed positions of hydrogen atoms. *Z. Kristallogr.* **1967,** *125* (1-6), 317-31.

22. Zigan, F.; Joswig, W.; Burger, N., The hydrogen position in bayerite, $Al(OH)_3$. *Z. Kristallogr.* **1978,** *148* (3-4), 255-73.

23. Hill, R. J., Hydrogen atoms in boehmite: A single crystal x-ray diffraction and molecular orbital study. *Clays Clay Miner.* **1981,** *29* (6), 435-45.

24. Corbato, C. E.; Tettenhorst, R. T.; Christoph, G. G., Structure refinement of deuterated boehmite. *Clays Clay Miner.* **1985,** *33* (1), 71-5.

25. Russell, J. D.; Farmer, V. C.; Lewis, D. G., Lattice vibrations of boehmite (γ-AlOOH): Evidence for a C_{2v}^{12} rather than a D_{2h}^{17} space group. *Spectrochim. Acta, Part A* **1978,** *34A* (12), 1151-3.

26. Hahn, T., *International tables of crystallography* Kluwer: London, 1995; Vol. A.

27. Wang, Y. G.; Bronsveld, P. M.; Dehosson, J. T. M.; Djuricic, B.; McGarry, D.; Pickering, S., Ordering of octahedral vacancies in transition aluminas. *J. Am. Ceram. Soc.* **1998,** *81* (6), 1655-1660.

28. Saalfeld, H., The dehydration of gibbsite and the structure of a tetragonal γ-Al_2O_3. *Clay Miner. Bull.* **1958,** *3*, 249-56.

29. Wilson, S. J., The dehydration of boehmite, γ-AlOOH, to γ-alumina. *J. Solid State Chem.* **1979,** *30* (2), 247-55.

30. Wang, J. A.; Bokhimi, X.; Morales, A.; Novaro, O.; Lopez, T.; Gomez, R., Aluminum local environment and defects in the crystalline structure of sol-gel alumina catalyst. *J. Phys. Chem. B* **1999,** *103* (2), 299-303.

31. Wolverton, C.; Hass, K. C., Phase stability and structure of spinel-based transition aluminas. *Phys. Rev. B Condens. Matter Mater. Phys.* **2001,** *63* (2), 024102/1-024102/16.

32. Gutierrez, G.; Taga, A.; Johansson, B., Theoretical structure determination of γ-Al_2O_3. *Phys. Rev. B Condens. Matter Mater. Phys.* **2002,** *65* (1), 012101/1-012101/4.

33. John, C. S.; Alma, N. C. M.; Hays, G. R., Characterization of transitional alumina by solid-state magic angle spinning aluminum nmr. *Appl. Catal.* **1983,** *6* (3), 341-6.

34. Blonski, S.; Garofalini, S. H., Molecular dynamics simulations of α-alumina and γ-alumina surfaces. *Surf. Sci.* **1993,** *295* (1-2), 263-74.

35. Lee, M. H.; Cheng, C.-F.; Heine, V.; Klinowski, J., Distribution of tetrahedral and octahedral al sites in gamma alumina. *Chem. Phys. Lett.* **1997,** *265* (6), 673-676.

36. Shirasuka, K.; Yanagida, H.; Yamaguchi, G., The preparation of η-alumina and its structure. *Yogyo Kyokai Shi* **1976,** *84* (12), 610-13.

37. Zhou, R. S.; Snyder, R. L., Structures and transformation mechanisms of the η, γ and θ transition aluminas. *Acta Crystallogr., Sect. B Struct. Sci.* **1991,** *B47* (5), 617-30.

38. Sohlberg, K.; Pantelides, S. T.; Pennycook, S. J., Surface reconstruction and the difference in surface acidity between γ- and η-alumina. *J. Am. Chem. Soc.* **2001,** *123* (1), 26-29.

39. MacIver, D. S.; Wilmot, W. H.; Bridges, J. M., Catalytic aluminas. Ii. Catalytic properties of η- and γ-alumina. *J. Catal.* **1964,** *3* (6), 502-11.

40. Jayaram, V.; Levi, C. G., The structure of δ-alumina evolved from the melt and the γ → δ transformation. *Acta Metall.* **1989,** *37* (2), 569-78.

41. Repelin, Y.; Husson, E., Studies of structural transition in aluminas. I. γ- and δ-aluminas. *Mater. Res. Bull.* **1990,** *25* (5), 611-21.

42. Bonevich, J. E.; Marks, L. D., The sintering behavior of ultrafine alumina particles. *J. Mater. Res.* **1992,** *7* (6), 1489-500.

43. Akbulut, H.; Durman, M., Temperature dependent strength analysis of short fiber reinforced Al-Si metal matrix composites. *Mater. Sci. Eng., A* **1999,** *A262* (1-2), 214-226.

44. Clyne, T. W.; Bader, M. G.; Cappleman, G. R.; Hubert, P. A., The use of a δ-alumina fiber for metal-matrix composites. *J. Mater. Sci.* **1985,** *20* (1), 85-96.

45. Cai, S.-H.; Rashkeev, S. N.; Pantelides, S. T.; Sohlberg, K., Phase transformation mechanism between γ- and θ-alumina. *Phys. Rev. B Condens. Matter Mater. Phys.* **2003,** *67* (22), 224104/1-224104/10.

46. Kohn, J. A.; Katz, G.; Broder, J. D., Characterization of β-Al_2O_3 and its alumina isomorph, θ-Al_2O_3. *Am. Mineral.* **1957,** *42*, 398-407.

47. Levin, I.; Brandon, D., Metastable alumina polymorphs: Crystal structures and transition sequences. *J. Am. Ceram. Soc.* **1998,** *81* (8), 1995-2012.

48. Waseda, Y.; Sugiyama, K.; Toguri, J. M., Direct determination of the local structure in molten alumina by high temperature x-ray diffraction. *Z. Naturforsch., A Phys. Sci.* **1995,** *50* (8), 770-4.

49. Bourdillon, A. J.; El-Mashri, S. M.; Forty, A. J., Application of tem extended electron energy loss fine structure to the study of aluminum oxide films. *Philos. Mag. A* **1984,** *49* (3), 341-52.

50. Luschtinetz, R.; Oliveira, A. F.; Frenzel, J.; Joswig, J.-O.; Seifert, G.; Duarte, H. A., Adsorption of phosphonic and ethylphosphonic acid on aluminum oxide surfaces. *Surface Science* **2008,** *602* (7), 1347-1359.

51. Stumpf, H. C.; Russell, A. S.; Newsome, J. W.; Tucker, C. M., Thermal transformations of aluminas and alumina hydrates. *J. Ind. Eng. Chem. (Washington, D. C.)* **1950,** *42*, 1398-1403.

52. Boer, J. H.; Linsen, B. G., *Physical and chemical aspects of adsorbents and catalysts: Dedicated to J. H. De boer on the occasion of his retirement from the technological university, delft, the netherlands*. Academic Press: 1970.

53. Liu, P.; Skogsmo, J., Space-group determination and structure model for κ-alumina by convergent-beam electron diffraction (cbed). *Acta Crystallogr., Sect. B Struct. Sci.* **1991,** *B47* (4), 425-33.

54. Ollivier, B.; Retoux, R.; Lacorre, P.; Massiot, D.; Ferey, G., Crystal structure of κ-alumina: An X-ray powder diffraction, TEM and NMR study. *J. Mater. Chem.* **1997,** *7* (6), 1049-1056.

55. Yourdshahyan, Y.; Ruberto, C.; Halvarsson, M.; Bengtsson, L.; Langer, V.; Lundqvist, B. I.; Ruppi, S.; Rolander, U., Theoretical structure determination of a complex material: κ-Al_2O_3. *J. Am. Ceram. Soc.* **1999,** *82* (6), 1365-1380.

56. Hem, J. D.; Roberson, C. E.; Lind, C. J.; Polzer, W. L. *Chemical interactions of aluminum with aqueous silica at 25.Deg*; United States Geol. Surv., Washington, DC, USA.: 1973; p 57 pp.

57. Baker, B. R.; Pearson, R. M., Water content of pseudoboehmite. New model for its structure. *J. Catal.* **1974,** *33* (2), 265-78.

58. Zhao, D.; Feng, J.; Huo, Q.; Melosh, N.; Fredrickson, G. H.; Chmelka, B. F.; Stucky, G. D., Triblock copolymer syntheses of mesoporous silica with periodic 50 to 300 angstrom pores. *Science* **1998,** *279* (23), 548-552.

59. Huo, Q.; Margolese, D. I.; Ciesla, U.; Demuth, D. G.; Feng, P.; Gier, T. E.; Sieger, P.; Firouzi, A.; Chmelka, B. F.; et al., Organization of organic molecules with inorganic molecular species into nanocomposite biphase arrays. *Chem. Mater.* **1994,** *6* (8), 1176-91.

60. Huo, Q.; Margolese, D. I.; Ciesla, U.; Feng, P.; Gier, T. E.; Sieger, P.; Leon, R.; Petroff, P. M.; Schueth, F.; Stucky, G. D., Generalized synthesis of periodic surfactant/inorganic composite materials. *Nature (London)* **1994,** *368* (6469), 317-21.

61. Zhang, Z.; Hicks, R. W.; Pauly, T. R.; Pinnavaia, T. J., Mesostructured forms of γ-Al_2O_3. *J. Am. Chem. Soc.* **2002,** *124* (8), 1592-1593.

62. Zhu, H. Y.; Gao, X. P.; Song, D. Y.; Bai, Y. Q.; Ringer, S. P.; Gao, Z.; Xi, Y. X.; Martens, W.; Riches, J. D.; Frost, R. L., Growth of boehmite nanoribers by assembling nanoparticles with surfactant micelles. *J. Phy. Chem.B* **2004,** *108* (14), 4245-4247.

63. Li, W.-C.; Lu, A.-H.; Schmidt, W.; Schuth, F., High surface area, mesoporous, glassy alumina with a controllable pore size by nanocasting from carbon aerogels. *Chemistry* **2005,** *11* (5), 1658-64.

64. Liu, Q.; Wang, A.; Wang, X.; Zhang, T., Ordered crystalline alumina molecular sieves synthesized via a nanocasting route. *Chem. Mater.* **2006,** *18* (22), 5153-5155.

65. Lee, H. C.; Kim, H. J.; Rhee, C. H.; Lee, K. H.; Lee, J. S.; Chung, S. H., Synthesis of nanostructured γ-alumina with a cationic surfactant and controlled amounts of water. *Micropor. Mesopor. Mater.* **2005,** *79* (1-3), 61-68.

66. Zhao, R.; Guo, F.; Hu, Y.; Zhao, H., Self-assembly synthesis of organized mesoporous alumina by precipitation method in aqueous solution. *Micropor. Mesopor. Mater.* **2006,** *93* (1-3), 212-216.

67. Bai, P.; Wu, P.; Yan, Z.; Zhao, X. S., A reverse cation-anion double hydrolysis approach to the synthesis of mesoporous gamma-alumina with a bimodal pore size distribution. *Micropor. Mesopor. Mater.* **2009,** *118*, 288-295.

68. Lesaint, C.; Kleppa, G.; Arla, D.; Glomm, W. R.; Oeye, G., Synthesis and characterization of mesoporous alumina materials with large pore size prepared by a double hydrolysis route. *Micropor. Mesopor. Mater.* **2009,** *119* (1-3), 245-251.

69. Tanev, P. T.; Pinnavaia, T. J., A neutral templating route to mesoporous molecular sieves. *Science (Washington, D. C.)* **1995,** *267* (5199), 865-7.

70. Acosta, S.; Ayral, A.; Guizard, C.; Cot, L., Synthesis of alumina gels in amphiphilic media. *J. Sol-Gel Sci. Technol.* **1997,** *8* (1/2/3), 195-199.

71. Cabrera, S.; El Haskouri, J.; Alamo, J.; Beltran, A.; Beltran, D.; Mendioroz, S.; Marcos, M. D.; Amoros, P., Surfactant-assisted synthesis of mesoporous alumina showing continuously adjustable pore sizes. *Adv. Mater. (Weinheim, Ger.)* **1999,** *11* (5), 379-381.

72. Cabrera, S.; El Haskouri, J.; Guillem, C.; Latorre, J.; Beltran-Porter, A.; Beltran-Porter, D.; Marcos, M. D.; Amoros, P., Generalized syntheses of ordered mesoporous oxides: The atrane route. *Solid State Sci.* **2000,** *2* (4), 405-420.

73. Kim, H. J.; Lee, H. C.; Choo, D. H.; Lee, H. C.; Chung, S. H.; Lee, K. H.; Lee, J. S., Synthesis and characterization of mesoporous alumina molecular sieves using cationic surfactants. *Stud. Surf. Sci. Catal.* **2003,** *146* (Nanotechnology in Mesostructured Materials), 213-216.

74. Lee, H. C.; Kim, H. J.; Choo, D. H.; Lee, H. C.; Chung, S. H.; Lee, K. H.; Lee, J. S., Synthesis and characterization of mesoporous alumina molecular sieves with cationic surfactants in the presence of formamide. *Stud. Surf. Sci. Catal.* **2003,** *146* (Nanotechnology in Mesostructured Materials), 217-220.

75. Yada, M.; Hiyoshi, H.; Ohe, K.; Machida, M.; Kijima, T., Synthesis of aluminum-based surfactant mesophases morphologically controlled through a layer to hexagonal transition. *Inorg. Chem.* **1997,** *36* (24), 5565-5569.

76. Sicard, L.; Llewellyn, P. L.; Patarin, J.; Kolenda, F., Investigation of the mechanism of the surfactant removal from a mesoporous alumina prepared in the presence of sodium dodecylsulfate. *Microporous Mesoporous Mater.* **2001,** *44-45*, 195-201.

77. Caragheorgheopol, A.; Caldararu, H.; Vasilescu, M.; Khan, A.; Angelescu, D.; Zilkova, N.; Cejka, J., Structural characterization of micellar aggregates in sodium dodecyl sulfate/aluminum nitrate/urea/water system in the synthesis of mesoporous alumina. *J. Phys. Chem. B* **2004,** *108* (23), 7735-7743.

78. Sicard, L.; Lebeau, B.; Patarin, J.; Zana, R., Study of the mechanism of formation of a mesostructured hexagonal alumina by means of fluorescence probing techniques. *Langmuir* **2002,** *18* (1), 74-82.

79. Valange, S.; Guth, J. L.; Kolenda, F.; Lacombe, S.; Gabelica, Z., Synthesis strategies leading to surfactant-assisted aluminas with controlled mesoporosity in aqueous media. *Microporous Mesoporous Mater.* **2000,** *35-36*, 597-607.

80. Vaudry, F.; Khodabandeh, S.; Davis, M. E., Synthesis of pure alumina mesoporous materials. *Chem. Mater.* **1996,** *8* (7), 1451-1464.

81. Cejka, J.; Kooyman, P. J.; Vesela, L.; Rathousky, J.; Zukal, A., High-temperature transformations of organised mesoporous alumina. *Phys. Chem. Chem. Phys.* **2002,** *4* (19), 4823-4829.

82. Cejka, J.; Zilkova, N.; Rathousky, J.; Zukal, A., Nitrogen adsorption study of organized mesoporous alumina. *Phys. Chem. Chem. Phys.* **2001,** *3* (22), 5076-5081.

83. Cejka, J.; Zilkova, N.; Rathousky, J.; Zukal, A.; Jagiello, J., High-resolution adsorption of nitrogen on mesoporous alumina. *Langmuir* **2004,** *20* (18), 7532-9.

84. Kim, Y.; Kim, C.; Kim, P.; Yi, J., Effect of preparation conditions on the phase transformation of mesoporous alumina. *J. Non-Cryst. Solids* **2005,** *351* (6-7), 550-556.

85. Bagshaw, S. A.; Pinnavaia, T. J., Mesoporous alumina molecular sieves. *Angew. Chem., Int. Ed. Engl.* **1996,** *35* (10), 1102-1105.

86. Bagshaw, S. A.; Prouzet, E.; Pinnavaia, T. J., Templating of mesoporous molecular sieves by nonionic polyethylene oxide surfactants. *Science (Washington, D. C.)* **1995,** *269* (5228), 1242-4.

87. Boissiere, C.; Nicole, L.; Gervais, C.; Babonneau, F.; Antonietti, M.; Amenitsch, H.; Sanchez, C.; Grosso, D., Nanocrystalline mesoporous γ-alumina powders "upmc1 material" gathers thermal and chemical stability with high surface area. *Chem. Mater.* **2006,** *18* (22), 5238-5243.

88. Hicks, R. W.; Pinnavaia, T. J., Nanoparticle assembly of mesoporous AlOOH (boehmite). *Chem. Mater.* **2003,** *15* (1), 78-82.

89. Ren, T.-Z.; Yuan, Z.-Y.; Su, B.-L., Microwave-assisted preparation of hierarchical mesoporous-macroporous boehmite alooh and γ-Al_2O_3. *Langmuir* **2004,** *20* (4), 1531-1534.

90. Zhu, H. Y.; Gao, X. P.; Song, D. Y.; Ringer, S. P.; Xi, Y. X.; Frost, R. L., Manipulating the size and morphology of aluminum hydrous oxide nanoparticles by soft-chemistry approaches. *Micropor. Mesopor. Mater.* **2005,** *85* (3), 226-233.

91. Sayari, A.; Yang, Y.; Kruk, M.; Jaroniec, M., Expanding the pore size of MCM-41 silicas: Use of amines as expanders in direct synthesis and postsynthesis procedures. *J. Phys. Chem. B* **1999,** *103* (18), 3651-3658.

92. Gonzalez-Pena, V.; Diaz, I.; Marquez-Alvarez, C.; Sastre, E.; Perez-Pariente, J., Thermally stable mesoporous alumina synthesized with non-ionic surfactants in the presence of amines. *Micropor. Mesopor. Mater.* **2001,** *44-45*, 203-210.

93. Yang, P.; Zhao, D.; Margolese, D. I.; Chmelka, B. F.; Stucky, G. D., Generalized syntheses of large-pore mesoporous metal oxides with semicrystalline frameworks. *Nature (London)* **1998,** *396* (6707), 152-155.

94. Niesz, K.; Yang, P.; Somorjai, G. A., Sol-gel synthesis of ordered mesoporous alumina. *Chem. Commun. (Cambridge, U. K.)* **2005,** (15), 1986-1987.

95. Deng, W.; Toepke, M. W.; Shanks, B. H., Surfactant-assisted synthesis of alumina with hierarchical nanopores. *Adv. Funct. Mater.* **2003,** *13* (1), 61-65.

96. Ray, J. C.; You, K.-S.; Ahn, J.-W.; Ahn, W.-S., Mesoporous alumina (i): Comparison of synthesis schemes using anionic, cationic, and non-ionic surfactants. *Micropor. Mesopor. Mater.* **2007,** *100* (1-3), 183-190.

97. Zhang, Z.; Pinnavaia, T. J., Mesostructured γ-Al_2O_3 with a lathlike framework morphology. *J. Am. Chem. Soc.* **2002,** *124* (41), 12294-12301.

Chapter 2

Structural Characterization Techniques

The physical properties of materials strongly depend on their structure. For nanoparticles with high surface to volume ratio, their properties are significantly influenced by several structural aspects including atomic arrangement, size and shape (morphology) of primary crystallite and their agglomerates, and available surface area of the particles and agglomerates. Therefore, accurate determination of nanoparticles structures and morphologies is critical to the design, preparation and applications of such materials.

In this dissertation, a combination of X-ray diffraction (XRD) and transmission electron microscopy (TEM) are used to study atomic arrangement, particle size, particle and agglomerate morphology of Al_2O_3 nanoparticles. Their surface area, pore volume and pore size distribution of porous materials are determined by nitrogen gas adsorption techniques. In this chapter, the basics of these techniques and the information gained are outlined and discussed.

2.1 X-ray diffraction (XRD)

X-ray diffraction (XRD) is a versatile, non-destructive technique that reveals detailed information about the chemical composition and crystallographic structure of natural and manufactured materials. It is provides valuable information about (1) average spacing between layers or rows of atoms, (2) orientation of a single crystal or grain, (3) crystal structure of an unknown materials and (4) size, shape and internal stress of small crystalline regions.

An electron can be described as an electromagnetic wave. In an alternating electromagnetic field having the same frequency, the electron will oscillate with the field. Similarly, when an X-ray beam hits an atom, electrons around the atom will oscillate with the

incident X-ray beam with the same frequency. For a single atom, this oscillation between the electron and the X-ray occurs in all direction. As a result, no energy is produced to leave the tom since the combining waves are out of phase due to destructive interference in all directions. However, in a crystal structure in which all the atoms are arranged in a regular pattern, constructive interference is observed in some directions where the scattering is on the same order of magnitude as the wavelength of the X-ray. In this case, well-defined X-ray beams are observed in different directions.

English physicists Sir W.H. Bragg and his son Sir W.L. Bragg developed a relationship in 1913 to explain why the cleavage faces of crystals appear to reflect X-ray beams at certain angles of incidence. As shown in Figure 2.1, parallel X-rays with an incident angle (θ) are reflected by the atomic planes consisting of periodic array of atoms. The variable *d* is the distance between atomic layers in a crystal, and the variable lambda (λ) is the wavelength of the incident X-ray beam. In order to obtain constructive interference of the reflected waves, the extra distance (2**d*sin(θ)) travelled by the lower X-ray penetrating deeper crystal plane must be an integral multiple of the wavelength. This relationship is known as Bragg's law, which is expressed in the Equation 2.1:

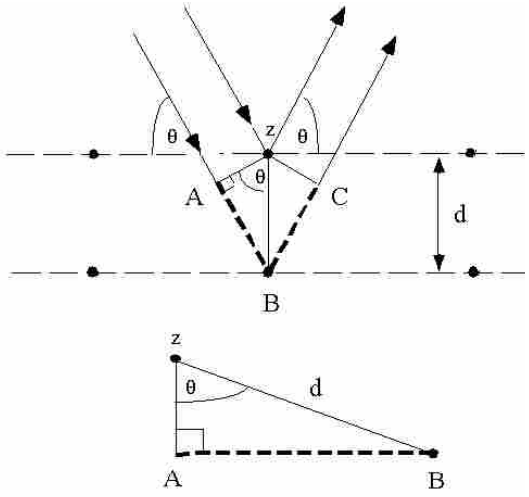

Figure 2.1 Reflection of X-rays by crystallographic planes of atoms and geometrical relationship leading to Bragg's law. Adapted from Ref. 1.

$$2d\sin(\theta) = n\lambda \qquad (2.1)$$

In crystallography, planes that give rise to such reflections are called lattice plane. The orientation relative to the lattice is defiend by Miller indices with the values *hkl*.

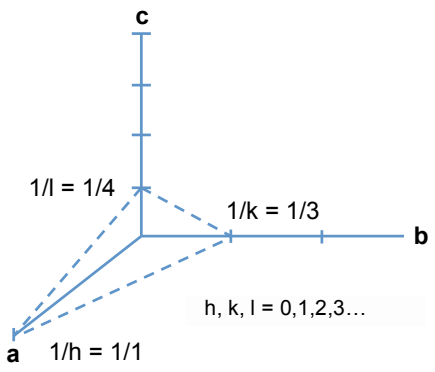

Figure 2.2 Definition of *hkl*-values in terms of intercepts on the axes. Adapted from Ref. 1.

As shown in Figure 2.2, for a given plane, the *hkl* indices are defined by determining the position relative to the nearest origin without passing through it.[1] Its intercepts on the *a*-, *b*- and *c*- axes of the unit cell will be $1/h$, $1/k$ and $1/l$. Therefore, the indices of the plane illustrated by dashed line in Figure 2.2 is (1 3 4).

Given the indices for each lattice plane, it is possible to construct all possible sets of lattice planes. However, it becomes complicated when many sets of lattice planes are presented in a single drawing of a crystal. Thus, a vector $\boldsymbol{d}$ is introduced to represent each set of planes. As illustrated in Figure 2.3, a vector $\boldsymbol{d_{hkl}}$ is defined to be the perpendicular distance from the origin of the unit cell to the nearest plane in the *hkl* family. For an orthorhombic crystal, the distance can be calculated using Equation 2.2:

$$\frac{1}{d^2} = \frac{h^2}{a^2} + \frac{k^2}{b^2} + \frac{l^2}{c^2} \qquad (2.2)$$

The direction of $\boldsymbol{d_{hkl}}$ is not simple to construct since the plane intercepts a/h, b/k and c/l. However, this can be simplified if the units $\boldsymbol{d}$, $\boldsymbol{a}$, $\boldsymbol{b}$, $\boldsymbol{c}$ are replaced by reciprocal entities $\boldsymbol{d}^*$, $\boldsymbol{a}^*$, $\boldsymbol{b}^*$ and $\boldsymbol{c}^*$. For an orthorhombic crystal, the relationship between the direct lattice and the reciprocal parameters are simply defined:

$$d^* = \frac{1}{d} \qquad a^* = \frac{1}{a} \qquad b^* = \frac{1}{b} \qquad c^* = \frac{1}{c} \qquad (2.3)$$

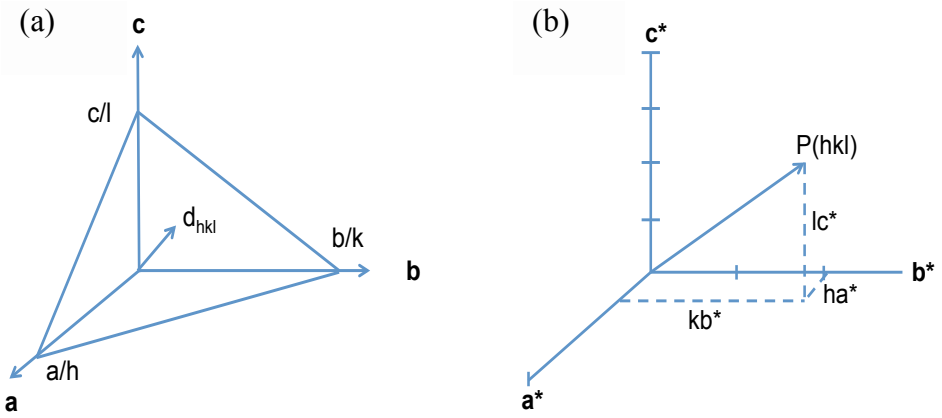

Figure 2.3 (a) ***d***-Vector in the direct lattice. (b) ***d****-Vector in the reciprocal lattice. Adapted from Ref. 1.

Similar to the Cartesian coordinate system, the plane spacing vector ***d**** can be easily defined by the reciprocal vectors ***a****, ***b**** and ***c****. A comparison of the ***d*** and ***d**** vectors in the direct system and reciprocal system are shown in Figure 2.4. It is evident that the reciprocal lattice is a useful construction for demonstrating the lattice planes of a crystal.

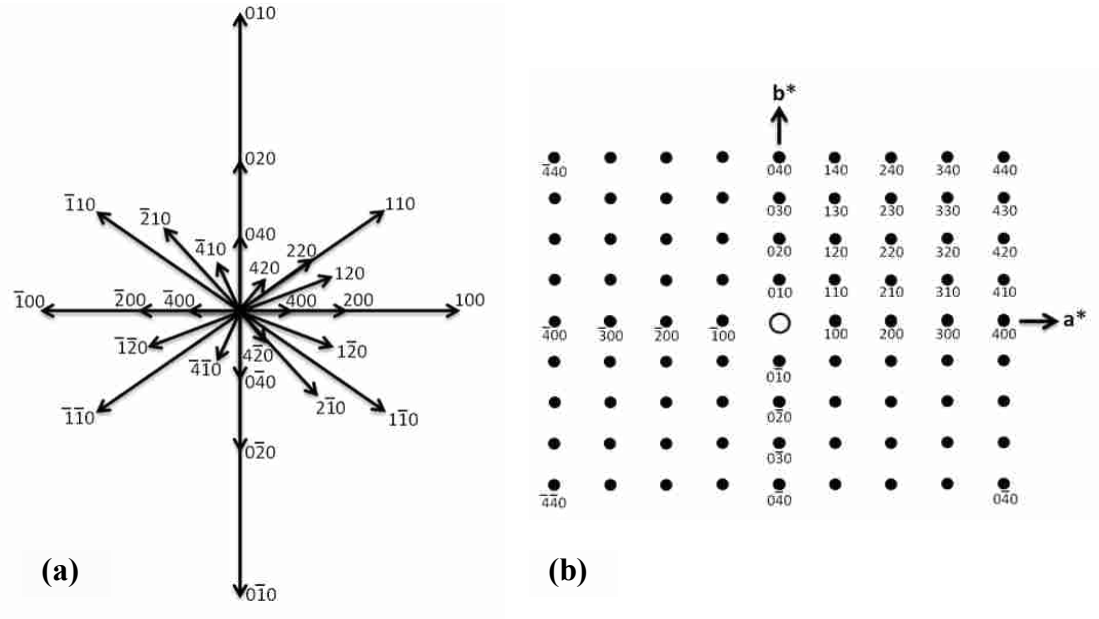

Figure 2.4 (a) Two-dimensional slice (the ab-plane) of the sphere of d_{hkl} vectors showing that the vectors approach the origin as $1/d$. (b) Plot of the $1/d = d^*_{hkl}$ vectors (from the ab-plane) where the vectors are represented as points. Adapted from Jenkins and Snyder.[2]

Based on the idea of reciprocal lattices, Ewald constructed an imaginary sphere, called an Ewald sphere, for visualizing the diffraction process in three dimensions. As illustrated in Figure 2.5, the Ewald sphere is centered on the real crystal, while the origin of reciprocal lattice is placed on the sphere's edge at the point of the undiffracted beam. If the incident angle (θ) equals that required by the Bragg equation for ***d***, a constructive interference of the reflected beam will occur and a diffracted beam can be observed at the angle 2θ. In the reciprocal lattice, the Bragg equation can be written as:

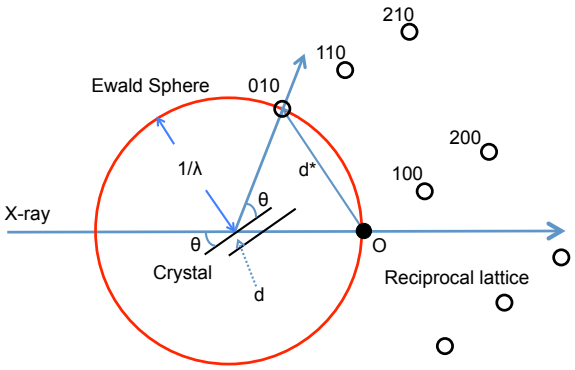

Figure 2.5 Relationship of the Ewald sphere (radius = 1/λ) to the reciprocal lattice. Adapted from Ref. 1.

$$\sin\theta = \frac{d^*/2}{1/\lambda} \qquad (2.4)$$

As the crystal rotates, the corresponding reciprocal lattice rotates as well. When the crystal is rotated so that one or more of the $\boldsymbol{d^*_{hkl}}$ points reach the Ewald sphere, the diffracted beam will pass through the sphere at the point of the reciprocal lattice. Accordingly, the intensity of this specific diffracted beam can be recorded by a detector placed tangent to the sphere at that point in real space.

For a well-ordered single crystal in the size rang from 100 to 500 μm, crystallographic analysis can provide invaluable information about the location of each atom in the crystal structure. Unfortunately, in the case of nanoparticles, they are comprised of powders consisting of small crystallites with sizes in the range from several to hundreds of nanometers oriented in all possible directions. As shown in Figure 2.6, a concentric cone is created by the $\boldsymbol{d^*_{hkl}}$ vectors touching the Ewald sphere in all directions. If a two-dimension detector is used, a concentric ring

pattern will be observed. The intensity of each ring can be integrated and plotted as a function of the scattering angle (2θ). If a small detector is used, it records a slice of the ring pattern and produces a pattern shown as Figure 2.6e. The powder X-ray diffraction pattern is unique for every compound and therefore can be used as standards to check the identity of an unknown sample.

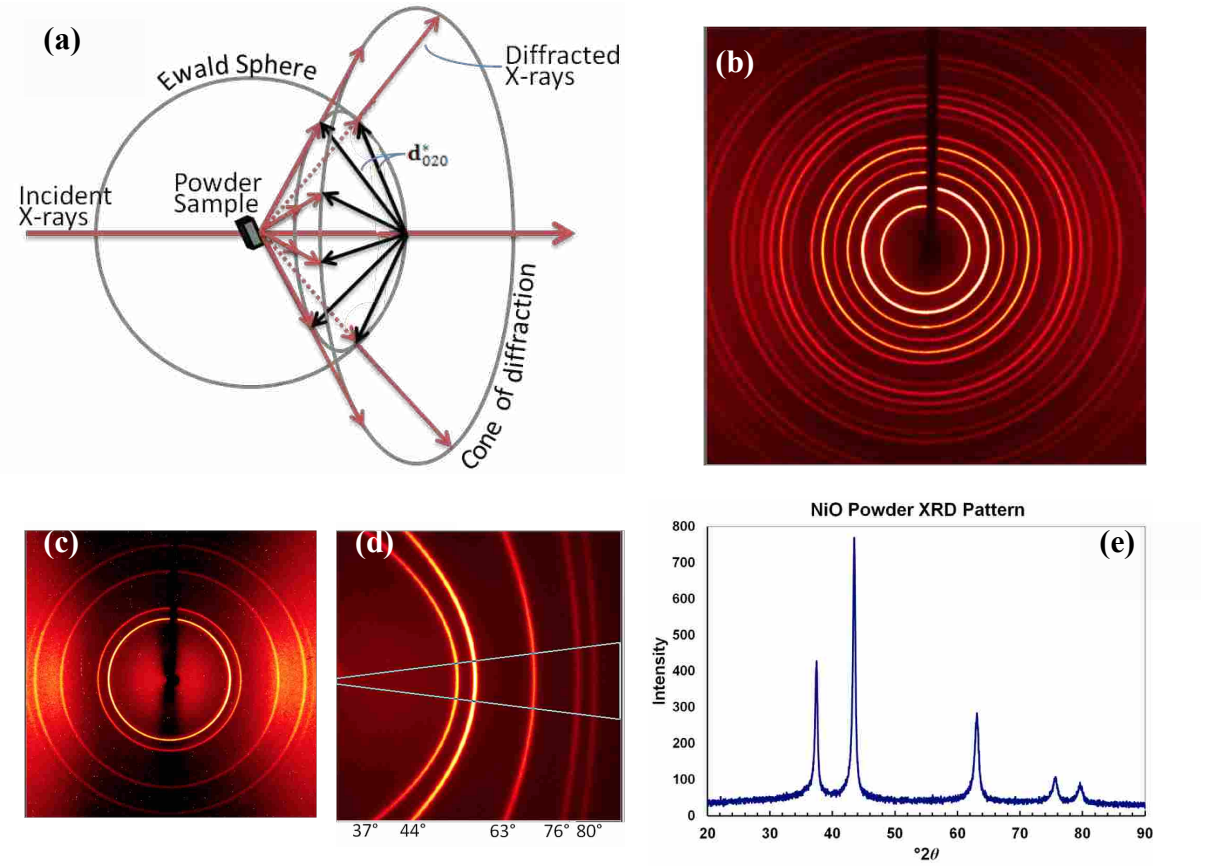

Figure 2.6 Illustartion of diffraction pattern produced by powdered samples. (a) Conceptual illustartion; (b) powder XRD ring pattern of (LaB_6); (c) Powder XRD ring pattern of NiO sample; A slice of the rings can be integrated as shown in (d) to give the 2-D XRD pattern shown in (e). Image (a) is adapted from Jenkins and Snyder,[2] (b) to (e) are adapted from Smith's dissertation[3]

Peak broadening is often observed for nanoparticles mainly due to the small crystallite size. Unlike well ordered single crystals, fewer unit cells are presented in the small crystallite. As a result, the destructive interference of the reflected beams is incomplete at angles near the Bragg angles. The smaller the crystallites, the more profound the braodened peaks. However, when size

related peak broadening is predominent compared to instrumental broadening, the average crystallite size and shape can be estimated using the Scherrer formula for each peak,[4]

$$d = \frac{0.9\lambda}{w\cos(\theta)} \qquad (2.5)$$

where d is the average crystallite diameter, λ is the wavelength of the incident X-rays, w is the peak width at half of the maximun height, and θ is the angle of that particular reflection.

2.2 Transmission Electron Microscopy (TEM)

Although X-ray diffraction can provide valuable structural information for nanomaterials, direct visible images of nanoparticles can only be obtained by transmission electron microscopy. Nowadays, due to the small de Broglie wavelength of electrons, TEMs are capable of producing extremely high quality images with significantly higher resolution (up to a few nanometers) than light microscopes. This capability greatly enhanced the visibility of materials in the nanoscale. Consequently, TEMs are extensively used in a wide range of applications, including cancer research, virology, material science, cell biology, pollution, nanotechnology, and semiconductor research.

2.2.1 Structure of TEM

The layout of a TEM is shown in Figure 2.7.[5] From the top down, a basic transmission electron microscope consists of an electron source, several sets of apertures and lens, and a detector screen.

The emission source is made of a tungsten filament or lanthanum hexaboride (LaB_6). When a high voltage (typically from 100 to 500 kV) is applied, electrons are emitted and accelerated into the vacuum by thermionic or field electron emission. A condenser lens consisting of electromagnetic rings is used to align the electron beam and control the current

density, size and focal point of the beam. Subsequently, objective lenses are used to focus the beam coming through the specimen and projector lenses are used to expand the beam onto imaging devices. Quad or hexapole lenses may also be used to correct asymmetrical beam distortions, or astigmatism. Finally, images produced by the elastic and inelastic scattered electrons are recorded using different modes, i.e. direct exposure or a digital CCD camera coupled with a fluorescent screen, depending on the required quality of the images.

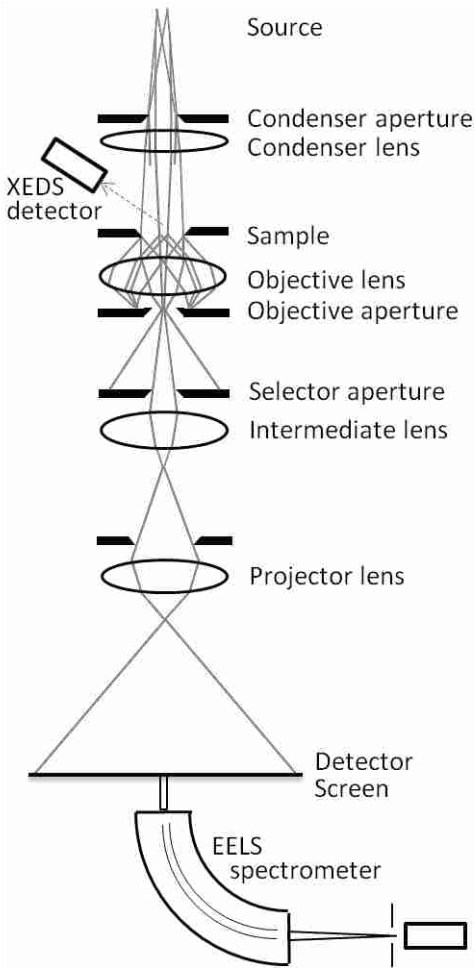

Figure 2.7 Diagram of a transmission electron microscope, adapted from Ref.5.

2.2.2 Modes of TEM

By changing how the beam is focused after the beam passes through the specimen, an image or a diffraction pattern similar to XRD can be collected.[6] Three imaging modes, i.e. bright field, dark field and selected area electron diffraction (SAED), are shown in Figure 2.8.

The most widely used mode of operation for a TEM is the bright field imaging mode. In this mode, the contrast formation is formed directly by blocking the scattered and/or diffracted electrons with a constricted objective aperture (Figure 2.8a). In this mode, regions have thicker sample or materials having a higher atomic number will appear dark, whereas regions with no sample (background) will appear bright. Bright field mode is very popular in the characterization

of nanoparticles due to its simplicity and relatively good contrast. However, it has low contrast with most of the biological samples.

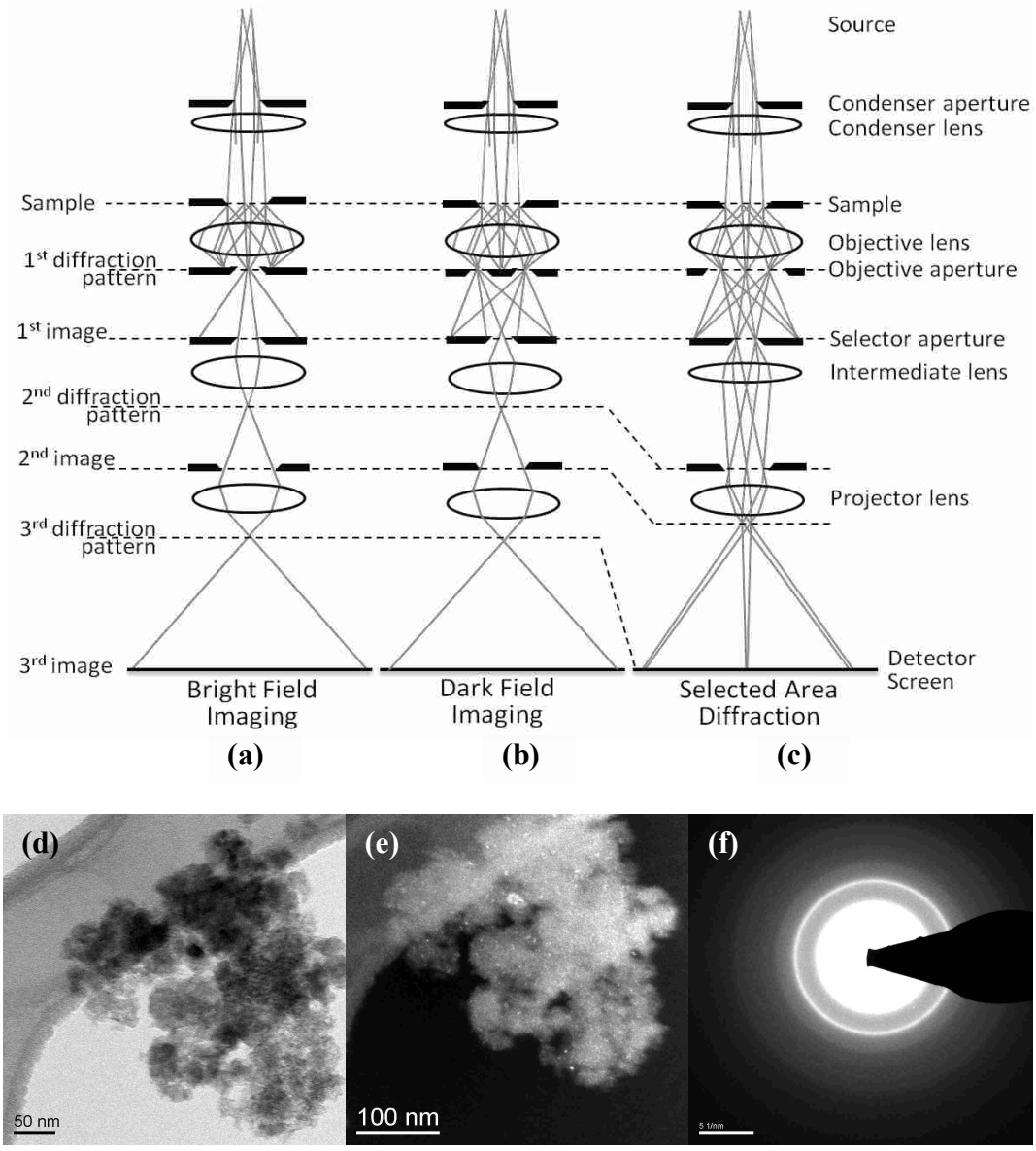

Figure 2.8 Ray diagrams for the (a) bright field, (b) dark field, and (c) selected area electron diffraction (SAED) modes of TEM imaging, adapted from Reimer.[5] (d), (e) and (f) are bright field, dark field and SAED images of Pt/La-Al_2O_3 nanoparticles, respectively.

In contrast to bright field mode, dark field mode is realized by blocking the primary electron beam while letting scattered and/or diffracted electrons pass through the objective lens (Figure 2.8b). This causes the particles that strongly scatter/diffract the electrons to be very

bright, whereas all others are very dim. Dark field microscope is ideal for viewing samples that are unstained, transparent and absorb little or no light. It has been used for examining biomolecules, organisms and thin polymers. However, its applicability is limited due to the high intensity required to illuminate the sample, which may cause damage to the sample.

Other than the two direct imaging modes, selected area electron diffraction (SAED) mode will produce point or ring diffraction pattern similar to those obtained by XRD. Since the wavelength of high-energy electrons is only a few thousands of a nanometer, the atoms will act as a diffraction grating to the electrons. By placing the apertures in the back focal plane, the desired Bragg reflections can be selected. In this mode (Figure 2.8c), a selected area aperture with different size holes is inserted. The holes allow a small fraction of the primary beam to pass through and contribute to the diffraction pattern on the screen. As a diffraction technique, SAED can be used to obtain information about crystal structures and lattice parameters on nanoparticles.

Besides the three imaging modes, elemental analysis can also be realized by X-ray energy-dispersive spectroscopy (XEDS) and electron energy loss spectrum (EELS). The principle of XEDS is shown in Figure 2.9a.[7] In XEDS, the high-energy beam of electrons is focused on the sample and may excite an electron in an inner shell. Subsequently, an electron from an outer, high-energy shell fills the hole created by the escaped high-energy electron. The difference between the higher energy shell and the lower energy shell may be released in the form of an X-ray, which is detected by an X-ray energy-dispersive spectrometer.[8] Since the atomic structure is unique for every element, the obtained spectrum can be used for qualitative and quantitative elemental analysis (Figure 2.9b). However, due to the small size of nanoparticles and the small solid angle inside the TEM, the signal of XEDS is likely to be

relatively low. In addition, the accuracy can be affected by the possibility of overlapping peaks from different elements and the homogeneity of the sample.

On the other hand, EELS has been used as a complimentary technique to XEDS for elemental analysis. In EELS, a beam of electrons with known, narrow range of kinetic energies is employed to pass through a sample. During the process, some of the electrons experience inelastic scattering, leading to loss of energy, which is measured by an electron spectrometer. The data is interpreted in terms of the cause of the energy loss, including phonon excitations, inter and intra band transitions, plasmon excitations, inner shell ionizations, and Čerenkov radiation.[9] Materials with low atomic numbers, e.g. from carbon through the 3d transition metals, are preferred in EELS, since the excitation edges tend to be sharp, well defined, and at experimentally accessible energy losses.[10]

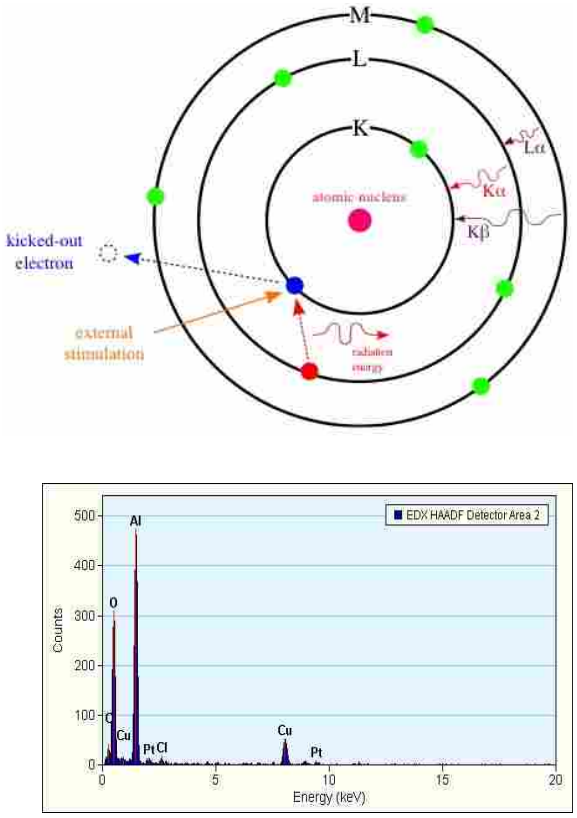

Figure 2.9 (a) Principle of X-ray energy-dispersive spectroscopy (XEDS), (b) XEDS spectrum of Pt/La-Al_2O_3 sample. Adapted from Ref. 7.

2.3 Gas adsorption methods

Adsorption, defined as the enrichment of materials or increase in the density of the liquid in the vicinity of an interface, occurs whenever a solid surface is exposed to a gas or a liquid.[11] Gas and liquid molecules are physically or chemically adsorbed on to the surface of the solid,

resulting in an enhancement in the concentration of a particular component at the interface of solid/liquid or solid/gas.

Based on the interaction between the adsorbent and the adsorbate, various mathematical methods have been proposed to describe the adsorption process, which can provide valuable information about surface structure, surface area (SA), pore volume (PV) and pore size distribution (PSD) of the adsorbent. Therefore, adsorption techniques, especially gas adsorption measurements, are widely used for the characterization of a variety of porous solids, including oxides, carbons, zeolites, and organic polymers.

2.3.1 Adsorption isotherms

Porosity of a material strongly influences the adsorption of a particular gas. Based on the pore size, porous materials are categorized into three groups: microporous (pore diameter < 2 nm), mesoporous (pore diameter between 2 and 50 nm) and macroporous (pore diameter > 50 nm).

For a given solid, the quantity of gas adsorbed is dependent on the temperature, the equilibrium pressure and the nature of solid-gas system. For a given gas adsorbed on a particular solid at a constant temperature, we have

$$\frac{n_a}{m_s} = f(p / p_0)_T \qquad (2.6)$$

The graphical illustration of this relationship is defined as an adsorption isotherm.

Though the adsorption isotherms of each material are unique, they are conveniently grouped into six classes of IUPAC classification shown in Figure 2.10 based on the common features for different solid-gas systems.[11, 12]

As shown in Figure 2.10, a Type I isotherm is concave to the P/P_0 axis. It rises sharply at low relative pressures and reaches a plateau. This type of isotherm is often observed from

microporous materials with relatively small external surface area. As for the Type II isotherm, it is concave to the P/P_0 axis in the low relative pressure range, then is almost linear and then

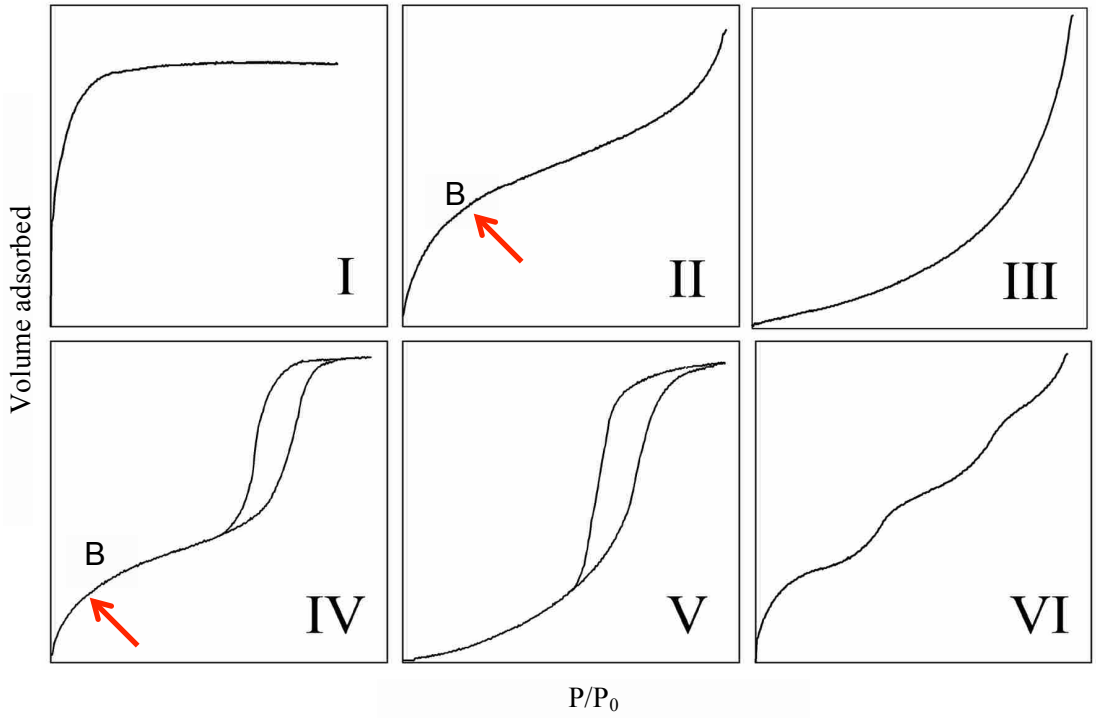

Figure 2.10 The six types (I, II, III, IV, V, and VI) of gas adsorption isotherms, adapted from Ref. 10.

convex to the P/P_0 axis in the high relative pressure range. It is associated with multilayer physisorption on the flat surface of nonporous or macroporous materials. If the knee of the isotherm is sharp, the uptake point B located at the beginning of the middle quasi-linear section is usually considered to represent the completion of the monolayer adsorption and the beginning of multilayer adsorption. It provides an estimation of the amount of absorbate required to cover the unit mass of solid surface with a complete monolayer, which is very useful in the calculation of surface area. A Type III isotherm is convex to the P/P_0 axis in the high relative pressure range and has no point B, indicating a weak adsorbate-adsorbent interaction. As for the Type IV isotherm, its initial region is similar to the Type II isotherm. However, the isotherm tends to level off and forms a hysteresis loop in the higher relative pressure range. This type of isotherm is

typical for mesoporous materials (silicas, titanias and aluminas); the hysteresis loop is associated with filling and emptying of the mesopores by capillary condensation. The Type V isotherm is

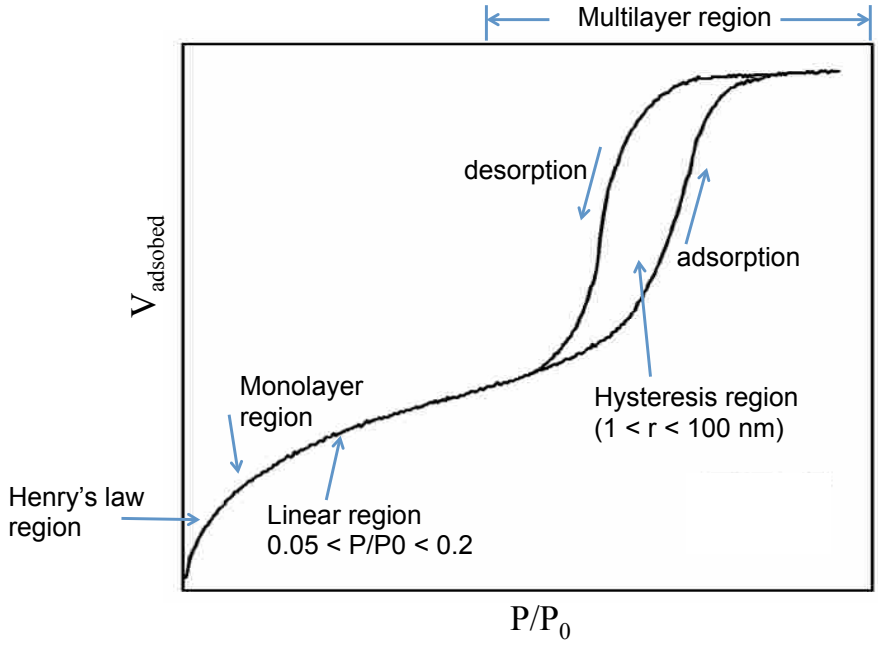

Figure 2.11 Full range type IV isotherm with adsorption and desorption branches.

similar to the Type IV, but the lack of point B indicates the interaction between the adsorbate and the adsorbent is weak. The Type VI isotherm is relatively rare and is associated with layer-by-layer adsorption on a highly uniform surface.

As shown in Figure 2.11, valuale information (Table 2.1) about the pore structures can be obtained from the full range of adsorption and desorption isotherm.[13] The method used to determine the pore structures (SA) is outlined in the following sections.

Various procedures have been developed to measure the amount of gas adsorbed. Volumetric methods are generally employed for measuring nitrogen at -196 °C. The isotherm is usually constructed in a point-by-point manner by the introduction and withdrawal of known amounts of gas with adequate equilibrium time. For the determination of surface area and pore

size distribution, the sample is degassed at a relatively high temperature (typically 150 to 200 °C) under nitrogen flow to remove water and air molecules adsorbed before measurements.

Table 2.1 Information available from full range isotherm

Region	Pressure range	Information obtained
Henry's law region	$P/P_0 < 0.01$	SA can be obtianed if Henry's law constant is known
Monolayer region	$0.05 < P/P_0 < 0.20$[a]	SA can be calculated using BET equantion
Multilayer region	$0.20 < P/P_0 < 1.0$	PV can be obtained at $P/P_0 = 1$ Pore structure can be inferred from the shape of hysteresis loop, PSD can be calculated using Kelvin equation

a. Linear region varies depending on the shape of isotherm and the type of gas

2.3.2 Determination of surface area

In 1916, Langmuir derived an equation for the adsorption of a unimolecular layer or monolayer. However, it is evident that the Langmuir equation is not applicable for mesoporous materials with a Type IV isotherm, in which multilayer adsorption and capillary condensation are observed. In 1938, Brunauer, Emmett, and Teller (BET) extended the concept of Langmuir equation to multilayer adsorption.

It should be stressed that a number of assumptions are made to derive the BET equation. (1) The surface of the adsorbent is viewed as an array of equivalent sites to which gas molecules are randomly adsorbed. (2) There is no lateral interaction between adsorbed molecules in the same layer. (3) The probability that a site will be occupied is independent to its local environment. (4) The adsorbed layer acts as the same surface as the adsorbent for the gas molecules to form the next layer. (5) The rate of adsorption of the i^{th} layer is equal to the rate of desorption of the $(i + 1)^{th}$ layer. (6) The heat of the condensation of the gas is the same for all the layers.

Based on these assumptions, BET equation can be derived as:

$$\frac{n}{n_m} = \frac{C_x}{(1-x)(1-x+C_x)} \tag{2.7}$$

where n is the moles of gas adsorbed at the equilibrium pressure p, n_m are the moles of gas required to form a complete monolayer, x is the relative pressure (P/P_0), and C was assumed to be a constant.

For the purpose of calculating surface area, Equation 2.7 can be written as:

$$\frac{P}{n(P^0-P)} = \frac{1}{n_m C} + \frac{C-1}{n_m C} \times \frac{P}{P^0} \tag{2.8}$$

According to Equation 2.8, a linear relationship is obtained when $P/n(P^0-P)$ is plotted against P/P_0. In the linear region, this plot will be a straight line, whose slope and intercept can be used to obtain n_m and the BET constant C. Subsequently, the specific surface area S_{BET}, can be calculated using:

$$S_{BET} = n_m L \sigma \tag{2.9}$$

where L is the Avogadro number and σ is the cross-sectional area occupied by each molecule.

For different gas adsorbates, their corresponding cross-sectional areas are different due to their size and packing (Table 2.2).[12, 14]

Table 2.2 Molecular areas of some adsobates

Adsorbate	Temperature (K)	Linear range[a]	Cross-sectional area (nm^2)
Nitrogen	77	0.13-0.20	0.162
Argon	77	0.10-0.19	0.138
Krypton	77	0.14-0.24	0.202
Xenon	77	0.16-0.25	0.170
Oxygen	77	0.13-0.20	0.141
Carbon dioxide	195	0.14-0.22	0.210

a. Linear range is adapted from Ref 14.

As for the C value, it is used as an indication of the goodness of the monolayer formation. A high C (> 100) for low temperature adsorption is a sign of a well-localized monolayer.

2.3.3 Characterization of pore structure

2.3.3.1 Pore shape and pore arrangement

As mentioned in Table 2.1, pore shape and pore arrangement can be inferred from the shape of the hysteresis loop observed in the Type IV isotherm. According to IUPAC classification, there are four major types of hysteresis loops, namely, H1, H2, H3 and H4.[12, 13] The shapes of these four hysteresis loops are shown in Figure 2.12.

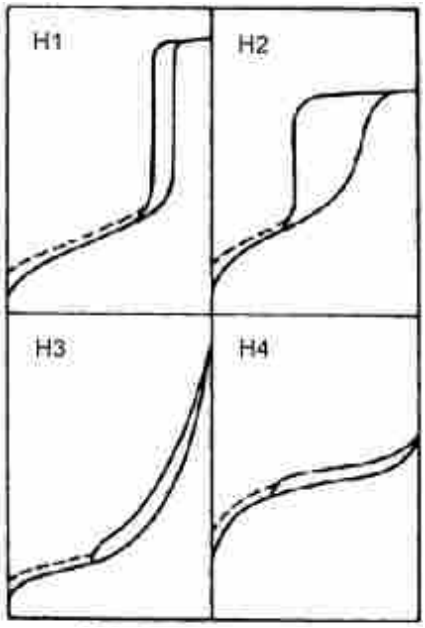

Figure 2.12 The IUPAC classification of hysteresis loops, adapted from Ref. 9.

As can be seen from Figure 2.12, Type H1 shows a narrow loop consisting of steep and nearly parallel adsorption and desorption branches. In contrast, for Type H2, a broad loop with a long plateau and a sharp desorption branch is observed. For Type H3 and H4, the loops do not close and a plateau is not formed until high P/P_0 range.

Since the hysteresis loops arise from capillary condensation in mesopores, the characteristics of each type of hysteresis are indications of the pore shape and pore arrangement. Accordingly, Type H1 hysteresis is generally observed from adsorbents with a narrow pore size distribution of uniform pores, whereas Type H2 hysteresis loop usually results from closely packed spherical particles with uniform size or from complex, interconnected pore network. As for Type H3 hysteresis loop, it is often given by the aggregates of plate-like particles or adsorbents with slit-like pores. For a Type H4 hysteresis loop, it is often observed from adsorbents with slit-like pores in the micropore range.

2.3.3.2 Calculation of pore size

As shown in Figure 2.13, a liquid/gas or liquid/liquid interface contained within a pore will tend to assume a shape of uniform mean curvature, which is dependent on the wettability of the pore wall and the size and shape of the pore. In a uniform cylindrical or parallel sided slit pores, the relationship between the radius of the curvature (r_k) and the nature of the liquid at a given relative pressure (P/P_0) can be calculated by the Kelvin equation:

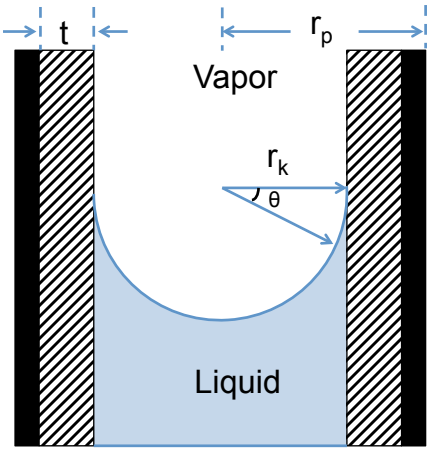

Figure 2.13 Cylindrical pore with adsorbed and condensed layers. Adapted from Ref. 12.

$$\ln(\frac{P}{P_0}) = -\frac{2\gamma v^l}{r_k RT}$$

where γ is the surface tension of the liquid and v^l is the molar volume of the liquid.

For nitrogen adsorbed at 77.35 K, we can use γ = 8.85 m/Nm, v^l = 34.71 cm^3/mol and obtain:

$$\frac{r_k}{nm} = -\frac{0.415}{\log_{10}(P/P_0)} \qquad (2.10)$$

Currently, the most widely used method is a model derived by Barrett, Joyner, and Halenda (BJH) in 1951,[15] which is based on the Kelvin Equation.

The computational procedure proceeds in a step-by-step manner. Like the desorption process, each step involves the removal of condensate from the core of a group of pores and the thinning of the multilayer in the larger pores. If the adsorption branch of an isotherm is used, then the process is reversed in the computation.

In the first desorption step, the initial volume removed is only from the capillary evaporation. In a simple cylindrical pore as shown in Figure 2.13, the relationship between the core volume ($v_{k,1}$) and the pore volume ($v_{p,1}$) is given by

$$v_{p,1} = \left(\frac{r_{p,1}^2}{r_{k,1}^2} \right) v_{k,1} \tag{2.11}$$

However, in the following desorption steps, the volume removed is the sum of the volumes from capillary evaporation (v_k) and thinning (v_t). Therefore, for step j:

$$\Delta v_j = \Delta v_{k,j} + \Delta v_{t,j} \tag{2.12}$$

The volume from the emptied condensate in step j is given by

$$v_{p,1} = \frac{r_{p,j}^2}{(r_{k,j} + \Delta t_j)^2} v_{k,1} \tag{2.13}$$

where $r_{k,j}$ and $r_{p,j}$ are the mean radius for the core and the pore for the step j.

For simple cylindrical pores with a length of L, its volume (V) and surface area (S) is given by $V = \pi r^2 L, S = 2\pi r L$. Therefore, we have

$$\Delta S_{p,j} = 2\Delta v_{p,j} / r_{p,j} \tag{2.14}$$

and

$$\Delta S_{k,j} = 2\Delta v_{k,j} / r_{k,j} \tag{2.15}$$

where $\Delta S_{p,j}$ and $\Delta S_{k,j}$ are the surface areas converted from successive condensate volume removed from the pore and the core, respectively.

In addition, in step j, the multilayer thickness t can be calculated by Halsey's equation[16]

$$t = -0.354 \left[\frac{5.00}{\ln(P / P_0)} \right]^{1/3} \tag{2.16}$$

Using Equation 2.10 through 2.16, we can obtain all the successive contributions from each step to the total pore volume. Subsequently, a pore size distribution is obtained by plotting the $\Delta v_{p,j}$ against $r_{p,j}$.

Although the BJH model provides reasonable estimates of the PSD for certain materials, its universal applicability due to the oversimplification in the theoretical model is questionable.

For example, its assumption of simple cylindrical pore geometry is not valid for materials with slit like pores, such as the mesoporous aluminas reported in this dissertation. In addition, it does not take the inhomogeneity, i.e. surface atoms and vacancies, into consideration. To solve these issues, an improved calculation of the PSD based on the slit-pore geometry for mesoporous materials with slit-like pores is reported in Chapter 3.

References

1. Massa, W., *Crystal structure determination*. Springer: 2004.
2. Jenkins, R.; Snyder, R., *Introduction to x-ray powder diffractometry*. Wiley: 2012.
3. Smith, J. S. The synthesis and structural characterization of metal oxide nanoparticles having catalytic applications. Dissertation, Brigham Young University, 2012.
4. Patterson, A. L., The scherrer formula for x-ray particle-size determination. *Phys. Rev.* **1939,** *56*, 978-82.
5. Reimer, L.; Kohl, H., *Transmission electron microscopy: Physics of image formation*. Springer: 2008.
6. Williams, D. B.; Carter, C. B., *Transmission electron microscopy: A textbook for materials science*. Springer London, Limited: 2009.
7. Muso Priciple of edx. Wikipedia.
8. Egerton, R. F., *Physical principles of electron microscopy: An introduction to TEM, SEM, and AEM*. Springer: 2005.
9. Brydson, R.; Society, R. M., *Electron energy loss spectroscopy*. Bios: 2001.
10. Ahn, C. C., *Transmission electron energy loss spectrometry in materials science and the eels atlas*. Wiley: 2006.
11. Rouquerol, J.; Avnir, D.; Fairbridge, C. W.; Everett, D. H.; Haynes, J. H.; Pernicone, N.; Ramsay, J. D. F.; Sing, K. S. W.; Unger, K. K., Recommendations for the characterization of porous solids. *Pure Appl. Chem.* **1994,** *66* (8), 1739-58.
12. Rouquerol, F.; Rouquerol, J.; Sing, K., *Adsorption by powders and porous solids*. Academic Press: London, 1999.
13. Bartholomew, C. H.; Farrauto, R. J., *Fundamentals of industrial catalytic processes*. 2 ed.; Wiley-AICHE: 2005.
14. Gregg, S. J.; Sing, K. S. W., *Adsorption, surface area and porosity*. 2 ed.; Academic Press: London, 1982.
15. Barrett, E. P.; Joyner, L. G.; Halenda, P. P., The determination of pore volume and area distribution in porous substance. I. Computations from nitrogen isotherms. *J. Am. Chem.Soc.* **1951,** *73*, 373-380.

16. Halsey, G., Physical adsorption on nonuniform surfaces. *J. Chem. Phys.* **1948,** *16*, 931-7.

Chapter 3

Improved calculations of pore size distribution for relatively large, irregular slit-shaped mesopore structure

3.1 Introduction

Accurate determination of BET surface area (SA), pore size distribution (PSD) and pore volume (PV) of porous supports, catalysts, and nanomaterials is vital to successful design and optimization of these materials and to the development of robust models of pore diffusional resistance and catalyst deactivation which are incorporated in catalytic reactor and process models.[1-4] Nitrogen adsorption at 77 K is used routinely to measure SA, PSD, and PV in mesoporous solids because of (1) its relative simplicity; (2) ease of measuring and analyzing data to obtain quantitative results; (3) accessibility of the gas to real pore structures, and (4) non-destructive application.[4] Mercury porosimetry is a useful complementary method to quantitatively determining meso and macroporosity in porous solids, although it is destructive and the operation, upkeep, and safety aspects of the instrumentation are not routine. While other experimental techniques, such as X-ray diffraction (XRD), small angle x-ray and neutron scattering (SAXS and SANS), transmission electron microscopy (TEM) provide additional insights into structural features of mesoporous solids, they are principally supplementary techniques due to their complexity and the relatively limited quantitative information provided by these methods regarding PSD and PV. In recent years, advanced theoretical approaches based on statistical mechanics, such as non-local density functional theory (NLDFT) and molecular simulation, have been developed to provide valuable structural information for porous networks.

However, their applicability is limited to well-organized pore structures with excellent structural and chemical uniformity. Furthermore, there is also a risk of oversimplification through the introduction of required functions; moreover, the accuracy of pore size estimates is typically no better than 15-20%.[3]

Fundamentals of multilayer adsorption applied to the assessment of mesoporosity are discussed in detail in books by Greg and Sing,[1] Rouquerol et al.,[4] Thomas & Thomas,[5] Hunter[6] and Lowell[7] and in reviews by Kaneko,[8] Groen et al.,[9] and Jaroniec and Kruk.[10] Several methods have been developed to calculate PV and PSD using data obtained from either adsorption or desorption branches of a full range nitrogen adsorption isotherm. In most classical pore models, data are analyzed using the Kelvin equation that relates partial pressure to pore radius in cylindrical pores. The volume of nitrogen adsorbed or desorbed as a function of P/P_0 (P_0 is the vapor pressure of liquid N_2 at liquid N_2 temperature) is corrected for the thickness of the adsorbed layer (which correction was originally proposed by Barrett, Joyner and Halenda[11]) and incrementally converted to obtain the PSD in the form of dV/dr as a function of r, where r is the pore radius. In principle, adsorption and desorption processes should be in equilibrium. However, in practice results obtained from adsorption and desorption branches differ due to non-ideal differences in capillary formation and evaporation leading to an observed hysteresis. Adsorption and desorption branches of the hysteresis loop can provide complementary information, although for specific hysteresis types one branch may be preferred over another.[12, 13]

One of the earliest and most widely used methods for calculating PV, PSD, and APD was proposed by Barrett, Joyner and Halenda[11] and is generally called the BJH method. This method is based on Wheeler's concept of a pore size distribution function L(r) and assumes cylindrical pore geometry. Pore radius rather than relative pressure is chosen as the independent

variable, and empirical corrections, including the assumption of an average pore radius in each pore size range, are made to the pore size distribution and in calculations of differential pore volume and area. While the BJH method appears to estimate pore volume well, it is well known that BJH analysis underestimate pore sizes by up to 20-30% when compared with either NLDFT or TEM determinations.[7, 14]

In general PV and PSD measurements obtained via the BJH and other typical methods are often in error because of flawed methods of data analysis based on simplistic assumptions and approximations. Moreover, these methods do not, in general, allow the extent of experimental error, precision, and accuracy to be readily assessed. For example, average pore radius determined from a typical dV/dr versus r distribution is likely to be significantly in error due to: (1) an inappropriate choice of the hysteresis branch (adsorption or desorption) for PSD analysis; (2) an incorrect form of the Kelvin equation based on an unrepresentative pore geometry, especially for irregular mesoporous materials; (3) inaccuracies in the geometric equations relating mesoporous surface area, pore volume and pore radius; and (4) asymmetry and tailing of the curves in the dV/dr PSD plot. Irregular pore structure is defined in the present context as nonparallel pores of varying size and shape, interrupted by structural defects.

Nevertheless, in principle, rational, careful consideration of the fundamental adsorption processes should provide a basis for accurate fitting of the distribution and for choices of the adsorption branch and form of the Kelvin equation in irregular mesoporous materials. In addition, validation by independent measurements (e.g. mercury porosimetry), the use of standard materials, and/or alternate methods of analysis, can ensure quantitative characterization of PV, PSD, and APD.

Indeed, a simple, useful, and accurate complementary method, namely the Comparative Adsorption (a_s) Method (CAM), can be used to independently assess mesopore surface area and volume. CAM is based on the comparison of the adsorption isotherm for the porous solid under study with that for an appropriate reference solid with similar surface properties.[1, 4, 15] Usually, a macroporous reference is chosen with surface properties similar to the material under study with respect to the adsorbate used. Adsorption on the macroporous reference proceeds via multilayer formation, whereas that of the porous solid under study includes both multilayer adsorption and condensation in the pores; this latter process is greatly influenced by pore size. To determine the pore size range in the sample under study (i.e. micro, meso, or macroporous), one can plot the amount adsorbed on the solid under study as a function of the amount adsorbed on the reference solid. If the adsorption on both solids proceeds via the same mechanism (multilayer formation), the comparative plot is linear in the applicable pressure range. Differences in the comparative plot can be attributed to different mechanisms, such as micropore filling or capillary condensation. Therefore, CAM can be used to check BET area against mesopore area and also to identify the individual adsorption and pore filling mechanisms.[15-18]

More sophisticated models for pore size calculations include the classical Broekhoff-de Boer (BDB) approach[19-23] which uses model porous materials (e.g. M41S and SBA-15) to calibrate the thickness relationship and the Kruk-Jaroniec-Sayari (KJS) model [24-26] which enables calibration of the Kelvin equation using a series of highly ordered MSM-silicas of known pore diameter obtained from SAXS. However, the application of calibration standards with the KJS model is only valid in the pore diameter range of 2 to 10 nm,[24, 27] Moreover, the BDB and KJS models are reliable only for highly-ordered cylindrical pores of very similar or the same diameter Thus, the BDB and KJS models are not applicable to the large class of irregular mesoporous

materials having noncylindrical pores of different sizes or constrictions, and/or pore diameters larger than 10 nm.

This chapter introduces an improved, rational approach (the SPG model) to the measurement of PSDs for mesoporous solids composed of slab-like particles. The SPG model comprises (1) the classical Kelvin equation adapted to the a slit geometry and (2) thinning corrections and calculations of differential surface area and volume according to the fundamental approach of Pierce, Orr, and Dalla Valle.[28, 29] The analysis is applied in the present study to large pore alumina supports, including two commercial aluminas and two novel wide-pore alumina supports developed in a previous work,[30] all four of which are clearly composed of slab-like materials but arranged in different geometries. Basic principles and critical assumptions are enumerated and discussed. Fundamentally based criteria are provided for making decisions at each step in the process, including: (1) selection of the appropriate form of the Kelvin equation based on knowledge of primary particle and pore geometries obtained from TEM and other techniques; (2) experimental determination of the appropriate structural factors relating pore radius to pore volume and surface area which account for differences in geometrical arrangements of the primary slab crystallites; and (3) use of the log-mean pore-size distribution with its inherent advantages of symmetry and well-defined error analysis.

3.2 Experimental Section

3.2.1 Materials

Reference material Aluminumoxid C Degussa (denote as DC) was purchased from Sigma-Aldrich and used as received. Two commercial alumina samples were obtained from Alfa Aesar (1/4 ring, Catalog No. 43858) and Saint Gobein (Trilobe, Catalog No. SA 6*78), denoted as Al-AA and Al-SG, respectively. Aluminum *iso*-propoxide ($Al(OCH(CH_3)_2)_3$), aluminum *sec*-

butoxide ($Al(OCH(CH_3)CH_2CH_3)_3$) were purchased from Alfa Aesar and used as received without purification. Deionized water was used in all the synthesis.

The synthesis procedure for large pore alumina materials was described elsewhere.[31-33] A typical synthesis involved formation of precursors followed by thermal treatment. For example, 24.158 g of aluminum sec-butoxide was mixed with 8.83 ml of distilled water (water to aluminum ratio 5:1) using a mortar and pestle for 15 minutes. The resultant white gel-like intermediate, or precursor, was subsequently thermally treated in a muffle furnace in air at 700 °C for 2 hours at a ramp rate of 2.33 °C/min. For aluminum *iso*-propoxide, the sample was prepared using the same procedure except for using a water to aluminum molar ratio of 7:1.

The final samples are labeled, starting with a prefix of Al followed by the type of aluminum salts (Iprop and Sbuto, which refer to aluminum *iso*-propoxide and aluminum *sec*-butoxide, respectively). Thus, Al-Iprop refers to alumina prepared from Aluminum sec-butoxide calcined at 700°C for 2 hours in air.

3.2.2 Measurements

The structure of each sample was determined by powder X-ray diffraction (XRD) using a Panalytical X'Pert Pro X-ray diffractometer with Cu Kα radiation (λ=0.15418 nm) at a scanning rate of 0.02°s^{-1} in the 2θ ranges from 10° to 80°. A fixed power source was used (40 kV, 40 mA). All alumina precursors were dried at room temperature overnight before the measurements. Crystallite sizes were estimated using the Scherrer formula for size-related peak broadening.

The morphology of each sample was observed with a FEI Philips Technai F30 transmission electron microscope (TEM) operating at 300 kV or a FEI Philips Technai F20 Analytical STEM operating at 200 kV. Specimens were prepared by dispersing samples in

ethanol, sonicating in a water bath for 1 hour, and then placing a drop of the diluted solution on a carbon film supported by a 400 mesh Cu grid (Ted-Pella Inc.).

Nitrogen adsorption analysis was carried out using a Micromeritics Tristar 3020 apparatus at -196 °C. Samples were degassed at 200 °C with nitrogen flow for 24 hours prior to measurements. Specific surface area (SA) was calculated by the Brunauner-Emmett-Teller (BET) method, using a P/P_0 range between 0.05 and 0.2.[1] The single point pore volume is obtained at $P/P_0 = 0.990$. The pore size and pore size distribution are calculated via both BJH model and SPG model described in the following sections for comparison.

3.2.3 Selection of isotherm branch for calculations of PSD

It is well known that hysteresis loops are associated with capillary condensation and evaporation. Moreover, the shape of the hysteresis loop can be correlated with the nanoscale structure of the adsorbent. In principle, the calculation of pore size distribution from either isotherm branch may provide useful and uniquely different results. However, in practice either the adsorption or desorption branch of the hysteresis could be affected by non-equilibrium deviations from the Kelvin equation, depending upon the pore geometry and heterogeneity of the adsorbent. Therefore, caution is needed in the choice of isotherm for PSD calculations, since either the adsorption or desorption branch of the isotherm may be unreliable and provide misleading results depending upon the structure of the solid and the pores [1, 4, 5, 34]. In the case of slit-like pores having an H1 hysteresis, the onset of capillary condensation during adsorption is typically considerably delayed by metastable adsorption films and hindered nucleation of liquid bridges [35-38]. As a result, the adsorption branch is shifted to a higher P/P_o value, which causes the pore size to be over-estimated. On the other hand, in uniform slit pores of finite length, open at both ends and already filled with liquid following the adsorption process, evaporation occurs

without such artifacts and in accordance with the Kelvin equation; thus, the desorption branch is the clear choice for calculation of the pore size distribution [4, 39]. By contrast, in complex pore systems with a wide range of pore sizes, including constrictions characteristic of H2 hysteresis, the desorption branch is significantly steeper than the adsorption branch; evaporation of the condensate is significantly constrained by the pore necks in an "ink-bottle" pore geometry and the connectivity of the network [40-43]. In this case, the desorption branch is unreliable and the adsorption branch is the correct choice for calculations of PSD.

3.2.4 Methods of calculation in the SPG Model

We use the following process to calculate PV, PSD, and APD from N_2 adsorption data. The observed hysteresis for a full range N_2 adsorption/desorption Type IV isotherm (see Figure 3.1) is a consequence of capillary condensation of liquid N_2 in complex mesopore networks during adsorption and of evaporation during desorption, each of these two processes having a different dependence of vapor pressure on pore radius. Traversing the adsorption branch with increasing relative pressure P/P_0 from about 0.40 to 0.70 a multilayer is formed in mesopores by physical adsorption of N_2 to a thickness t (see Figure 3.1). At a P/P_0 of about 0.70-0.80, condensation is initiated due to accumulating van der Waals interactions between the vapor phase molecules inside the confined space of a capillary; a meniscus is immediately formed. The mechanical equilibrium

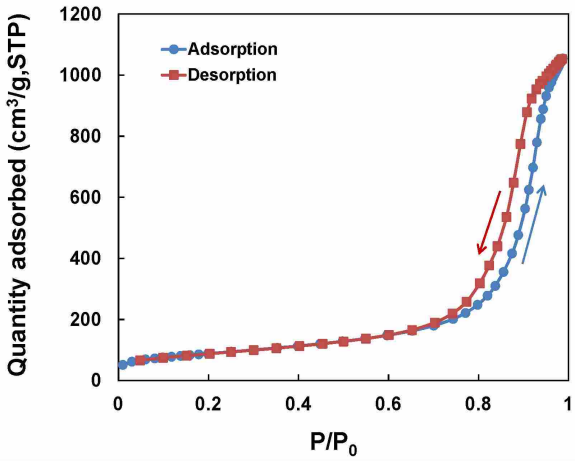

Figure 3.1. Type IV isotherm for large mesopore alumina

between two fluids at the opposite sides of the meniscus at different pressures is given by the Kelvin equation:

$$\ln(\frac{P}{P_0}) = -\frac{2\gamma(\cos\theta)V_L}{r_k RT} \qquad (3.1)$$

where γ is the surface tension and r_k is the radius of the curvature of the meniscus, θ is the contact angle between the liquid and the adsorbed layer on the wall, and V_L is the molar volume of the liquid.

The form of r_k, the radius of the curvature of the meniscus in the Kelvin equation, is fundamentally different for different geometries and in some cases for the different hysteresis branches. This is best understood from the Young-Laplace equation:

$$P_{vap} - P_{liq} = \frac{\gamma}{r_k} = \frac{\gamma}{2}(\frac{1}{r_1} + \frac{1}{r_2}) \quad \text{or} \quad \frac{2}{r_k} = \frac{1}{r_1} + \frac{1}{r_2} \qquad (3.2)$$

where P_{vap} and P_{liq} are the pressures of each side of the membrane, γ is the surface tension, and r_1 and r_2 are the radii of the curvature (see Figure 3.2a).

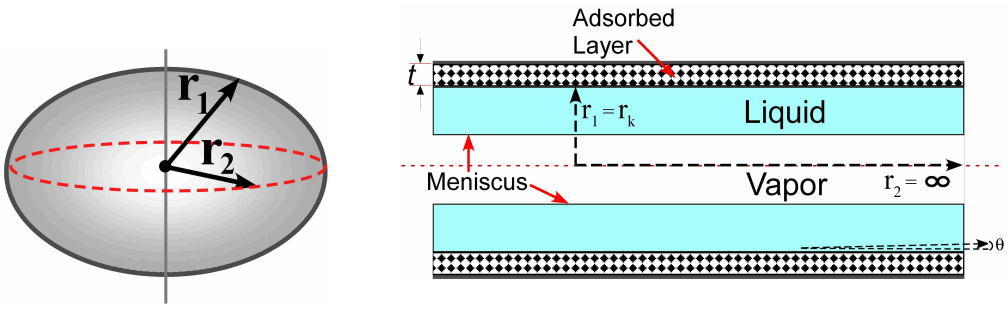

Figure 3.2. Different shapes of meniscus. (a) Two radii for an ellipsoidal meniscus; (b) Two radii for a cylindrical meniscus formed during adsorption in a slit open at both ends

For condensation or evaporation in a cylindrical pore (one end open) having a hemispherical meniscus, $r_1 = r_2 = r_k$. The hemispherical meniscus is formed inside a single,

cylindrical adsorbed layer of thickness t. Therefore, for a cylindrical pore with a meniscus of hemispherical radius r_k, adsorbed multilayer thickness t and r_k add to give the pore radius, r_p:

$$r_p = r_k + t \tag{3.3}$$

For condensation in a cylindrical pore open at both ends, the meniscus is a cylindrical annulus for which $r_1 = r_k$ and $r_2 = \infty$; thus, $r_m = 2\,r_k$ (see Eqn. 3.2 and Figure 3.2b). Similarly, in the case of a slit-shaped pore, $r_m = 2\,r_k = w_k$, where w_k is the pore width (note that Figure 3.2b also applies for slit geometry). For a slip-shaped pore there are two adsorbed layers of thickness t on either side of the cylindrical meniscus (Figure 3.2b). Thus, the effective pore width of slit-shaped pore w_p is given by:

$$w_p = r_k + 2t \tag{3.4}$$

The thickness t of the adsorbed layer can be calculated using Halsey's equation[44] in terms of the volume V absorbed at a given P/P_0 divided by the monolayer volume V_m times σ, the effective height of a layer, for which σ is 0.354 nm assuming hexagonal close packing of the adsorbed layer:

$$t = -0.354\left[\frac{5.00}{\ln(P/P_0)}\right]^{1/3} \tag{3.5}$$

In the classical calculation of pore size and pore size distribution by Pierce, Orr, and Dalla Valle,[28, 29] the decrement in adsorbed volume ΔV_p during desorption consists of the decrement in gas volume from the adsorbed layer ΔV_f and the volume ΔV_k attributed to desorption from pores containing liquid condensate. For a parallel plate model and a rectangular-shaped pore, the relationship between ΔV_p and ΔV_k can be defined by:

$$\Delta V_p = \Delta V_k\left(\frac{w_p}{r_k}\right) = \Delta V_k\left(\frac{w_p}{w_p - 2t}\right) \tag{3.6}$$

In the original slit model according to Innes,[45] the calculation assumes a regular (all angles of 90°) rectangular volume. However, in a real system of semi-parallel slabs or randomly piled slabs, the slabs are not regular and hence the spaces between them (slit pores) are irregular rectangular spaces of monoclinic or triclinic geometry and may even be of a triangular solid geometry. Furthermore, the surface of the porous sample is not smooth as commonly assumed but contains defects, e.g. vacancies and atoms; in fact, γ-alumina is a defect spinel structure. Therefore, in the present study, we introduce a structural factor β to account for irregular slit pores (e.g., wide on one end and narrow at the other) and surface roughness such that the calculated pore volume closely matches the experimentally measured value. The corrected form of conversion is then given by:

$$\Delta V_p = \Delta V_k \left(\frac{w_p}{w_p - 2t}\right) \tag{3.7}$$

The specific surface area ΔS corresponding to a ΔV_p contained by parallel plates can be calculated by

$$\Delta S_p = \frac{2\Delta V_p}{w_p} \tag{3.8}$$

However, it is expected that the V_p/S_p ratio will vary with pore geometry and pore radius. Changes in the structure factor with pore radius occur mainly in small mesopores for which surface/volume ratio is higher. The correction to α for geometry can be calculated using a semi-empirical equation for average pore radius derived by Wheeler [46]:

$$w_p = (\tau\varepsilon)\left(\frac{2\Delta V_p}{\Delta S_p}\right) = \alpha\left(\frac{2\Delta V_p}{\Delta S_p}\right) \tag{3.9}$$

where τ is the roughness factor (assumed by Wheeler to be 2), which is defined as the experimental surface area of a rough surface divided by its projected geometric surface, and ε is

the void fraction for a specified packing, thus, $\alpha = \tau\ \varepsilon$. In the present study, this α value is calculated by taking the ratio of the calculated surface area and experimental BET surface area.

To better estimate PSD and APD, and given (1) the typically observed asymmetry and tailing of the dV/dr vs r curves and (2) substantial evidence that pore size distributions are log normal, we have long since adopted a log normal distribution as defined by Hald[47] and as originally applied to pore size distributions by Nobe et al.[48]:

$$f = \frac{1}{(2\pi)^{1/2}\sigma D}\exp\left[-\frac{(\ln D - \mu)}{2\sigma^2}\right] \qquad (3.10)$$

where D is the pore diameter, μ and σ are the mean value and standard deviation, respectively. In our calculation of PSD, the experimental pore volume (dV) is plotted versus pore width in log scale ($d\ln(x_p)$) and normalized. For data points of the PSD peak, a calculated function based on the log normal distribution is normalized and compared with the experimental value. The sum of the differences between calculated and experimental volume density functions are minimized to obtain the best fit of the data, from which we get statistical values of average pore size and its standard deviation σ. The complete computational procedure is provided for one of the alumina samples in the form of a spreadsheet in the supporting information.

3.2.5 CAM method

To independently assess mesopore surface area and volume, we use the CAM method to get total surface area, external surface area, and mesopore volume based on a non-porous reference material.[18] Since the aluminas in the present study are calcined at 700 °C, Degussa Aluminumoxid C have been found suitable for the analysis of isotherms on porous γ-alumina because of its similar surface chemistry.[16, 17, 34]

The adsorption data in a low-pressure range can be used to determine the total surface area S_{tot} and the micro

$$v = v_{mi} + \mu_1 \alpha_s \tag{3.11}$$

where μ_1 is the slope of linear part of the α_s plot, and v_{mi} is the intercept with the adsorbed amount axis providing the amount adsorbed in micropores. The total surface area S_{tot} is given by:

$$S_{tot} = \mu_1 S_{BET,ref} / v_{0.4,ref} \tag{3.12}$$

where $S_{BET,ref}$ and $v_{0.4,ref}$ are the BET surface area and the amount absorbed at P/P_0=0.4 for the reference adsorbent. The micropore volume V_{mi} can be calculated by

$$V_{mi} = v_{mi} c \tag{3.13}$$

where c is the conversion factor between the volume in gas and liquid nitrogen adsorbate. If V_{mi} and v_{mi} are expressed in cm^3/g and cm^3 STP/g, respectively, c = 0.0015468.

External surface area S_{ext} and primary mesopore volume V_p can be assessed using the high-pressure adsorption data based on the relation:

$$v = v_p + \mu_2 \alpha_s \tag{3.14}$$

where μ_2 is the slope of the linear part of the high-pressure range of the α_s plot, and v_p is the intercept with the adsorbed amout axis. Then S_{ext} can be calculated using Eq. 3.12 with μ_2, whereas V_p is given by

$$V_p = v_p c - V_{mi} \tag{3.15}$$

3.3 Results

The XRD patterns of alumina samples are shown in Figure 3.3. Characteristic peaks of γ-alumina (JCPDS card 00-029-0063) are clearly seen. The seven peaks of gamma alumina can

be indexed to the (1 1 1), (2 2 0), (3 1 1), (2 2 2), (4 0 0), (5 1 1), (4 4 0) reflections. The average diameters of Al-Iprop and Al-Sbuto calculated by the Scherrer formula based on the (440) peaks are about 4 nm, whereas the average values of Al-AA and Al-SG are about 5 nm.

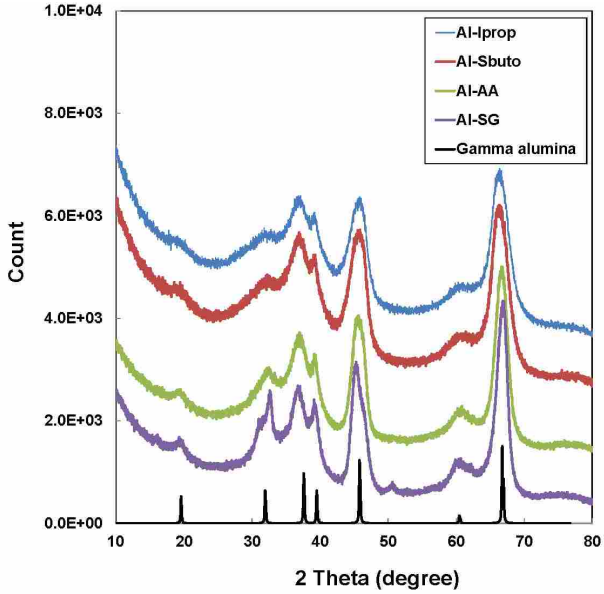

Figure 3.3. XRD patterns of different alumina samples.

Figure 3.4 shows the TEM images of alumina samples. A careful examination of the images for Al-Iprop and Al-Sbuto samples is consistent with overlapping platelets in the plane and others normal to the plane of the micro graph, showing a three-dimensional open packing order. These platelets are roughly 30-50 nm long, 15-20 nm wide, and 4-5 nm thick, which is consistent with the particle size calculated from the XRD results. For Al-AA and Al-SG samples, primary particles consist of overlapping platelets in one plane; platelets have dimensions similar to those of samples prepared from aluminum alkoxides (see Figure 3.4c and 3.4d).

Nitrogen adsorption-desorption isotherms of the different alumina supports are shown in Figure 3.5. According to IUPAC, all the isotherms are Type IV, indicating the presence of mesopores. The N_2 adsorption capacities of Al-AA and Al-SG are in the range of 400 to 500 cm^3/g STP, whereas those for aluminas prepared from aluminum alkoxides are in the range of 800 to 1100 cm^3/g STP. It is well known that the N_2 adsorption capacity is proportional to pore volume.[1] Thus, the extraordinarily large nitrogen adsorption uptakes by the alumina samples

synthesized from aluminum alkoxides are consistent with their large pore volumes observed in this study (Table 3.1).

Table 3.1 Structural parameters of different Al_2O_3 samples

Sample	S_{BET} [a] (m^2/g)	C [a]	$S_{me,cal}$ [b] (m^2/g)	$S_{tot,a}$ [c] (m^2/g)	$S_{ext,a}$ [c] (m^2/g)	$S_{p,a}$ [c] (m^2/g)	$V_{p,a}$ [c] (cm^3/g)	$V_{me.cal}$ [b] (cm^3/g)	V_{sp} [d] (cm^3/g)
Al-Sbuto	300	166	216	297	75	222	1.42	1.47	1.62
Al-Iprop	288	165	246	285	35	250	1.34	1.36	1.49
Al-AA	175	159	122	173	47	126	0.63	0.68	0.76
Al-SG	162	165	113	160	46	114	0.56	0.61	0.68

a. S_{BET}, C denote BET SA and BET constant determined by N_2 adsorption at 77 K and calculated from the BET equation using P/P_0 ranges form 0.05-0.20.
b. $S_{me,cal}$, $V_{me.cal}$, denote mesopore surface area and volume calculated from SPG model over pore width range of 2 to 50 nm.
c. $S_{tot,a}$, $S_{ext,a}$, $S_{p,a}$, $V_{p,a}$, denote total surface area, external surface area, mesopore area, mesoporous volume calculated using α_s method.
d. V_{sp} is pore volume obtained from single point method at $P/P_0 = 0.99$

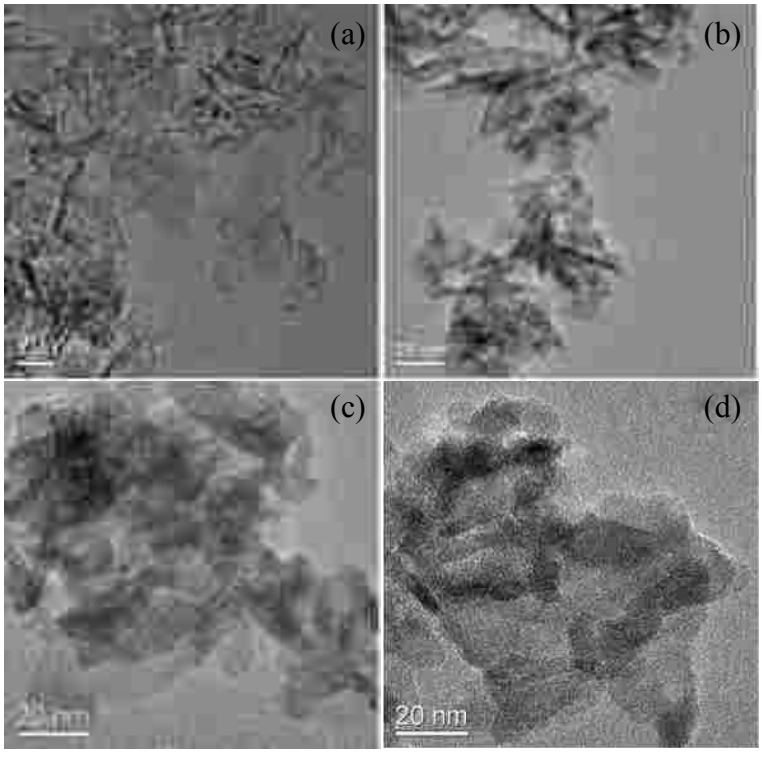

Figure 3.4. TEM images of different alumina samples: (a) Al-Iprop; (b) Al-Sbuto; (c) Al-AA (d) Al-SG

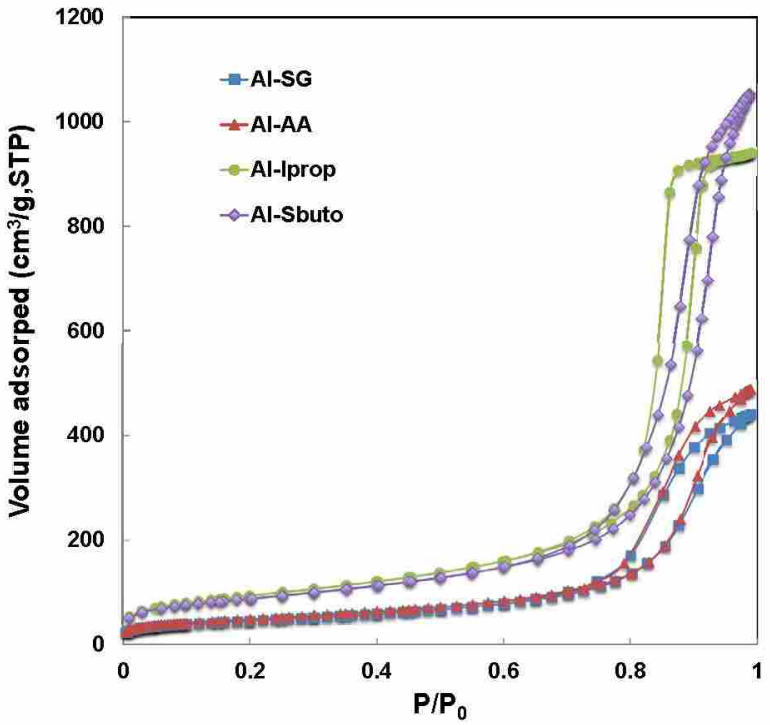

Figure 3.5. N_2 adsorption/desorption isotherms of different alumina samples.

Figure 3.6 shows the α_s plots for the four different alumina samples. The low-pressure part of these plots exhibits excellent linearity starting from the lowest adsorbed quantity, indicating the absence of micropores. This linearity is also observed for organized mesoporous aluminas.[17] The subsequent steep increase at higher a_s values is due to capillary condensation of nitrogen in the mesopores. From the slope of the linear portion of the comparative plot, total surface area and external surface area of these four samples are obtained. As evident in Table 3.1, values of total surface area S_{tot} and BET surface area S_{BET} are in excellent agreement for each sample, e.g. 297 and 300 m^2/g for Al-Sbuto. Given that S_{tot} corresponds to the area of mesopores only, the agreement of S_{tot} and S_{BET} further confirms the absence of detectable micropores in all four samples. It is also worth noting that the BET constants (C values) for all alumina samples are greater than 100, indicating a well-defined localized monolayer,[4] which is

indicative of the validity of the BET data. Furthermore, the calculated mesopore areas from CAM, agree within 3% of the areas obtained from the SPG model, while mesopore volumes agree within 3-8%, confirming that the proposed SPG model provides accurate assessments of these two pore properties.

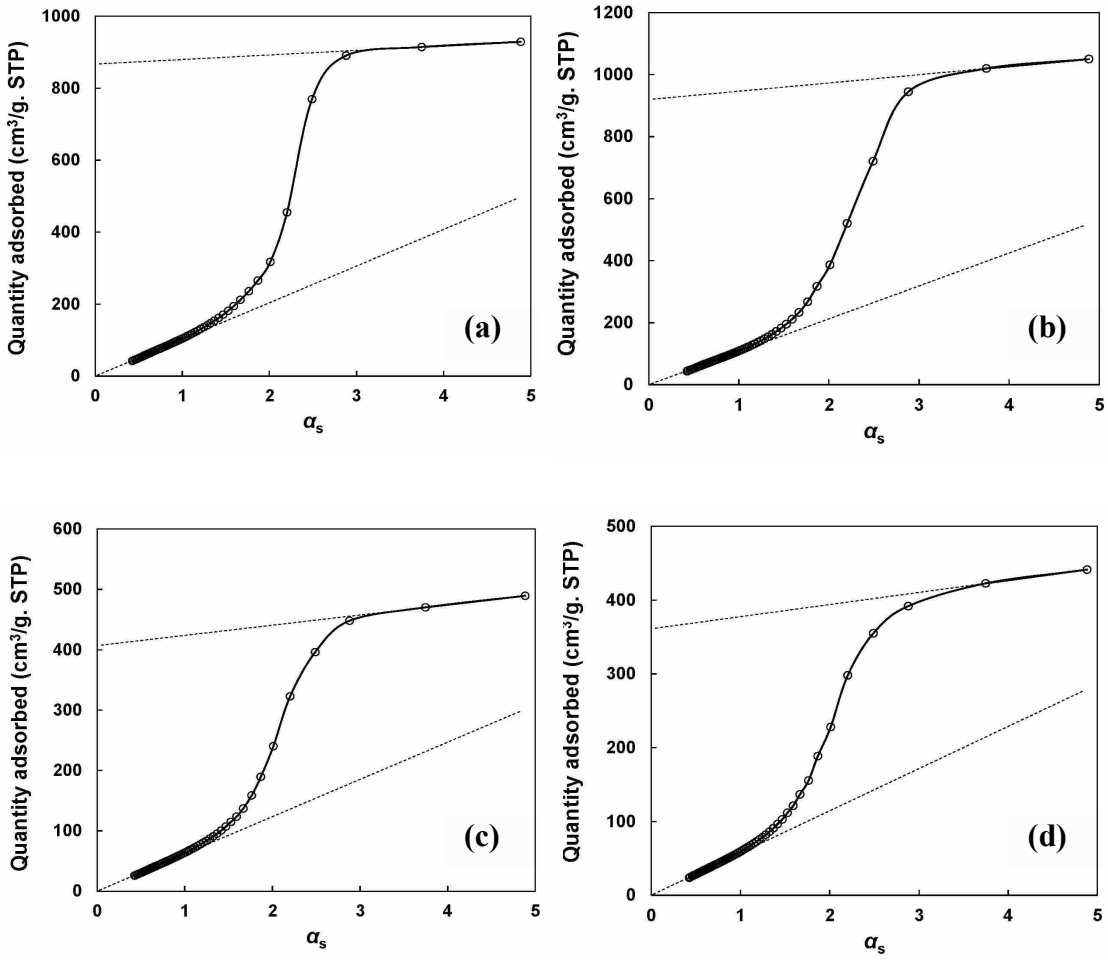

Figure 3.6 α_s Plots of different alumina samples: (a) Al-Iprop; (b) Al-Sbuto; (c) Al-AA (d) Al-SG

The pore size distributions of the alumina samples devived from both BJH and SPG models are shown in Figure 3.7. Pore widths, standard deviation, and the coefficient of determination for the fitting of log normal distribution, calculated from BJH and SPG model using both adsorption and desorption branches, are listed in Table 3.2. All four samples have

Table 3.2 Pore widths & standard deviations for Al_2O_3 samples

Sample	W_{BJH} [a] (nm)		W_{SPG} [b] (nm)		σ [c]		R^2	
	Adsorp	Desorp.	Adsorp.	Desorp.	Adsorp.	Desorp.	Adsorp.	Desorp.
Al-Sbuto	18.3	14.5	30.1	18.3	1.66	1.48	0.914	0.990
Al-Iprop	14.5	12.0	19.8	13.8	1.21	1.08	0.963	0.986
Al-AA	14.9	12.7	24.0	13.5	1.64	1.27	0.947	0.959
Al-SG	14.2	12.0	21.4	13.1	1.62	1.26	0.918	0.934

a. Average slit width calculated using BJH method
b. Average slit width calculated using SPG slit model
c. Standard deviation calculated using slit (SPG) model

large

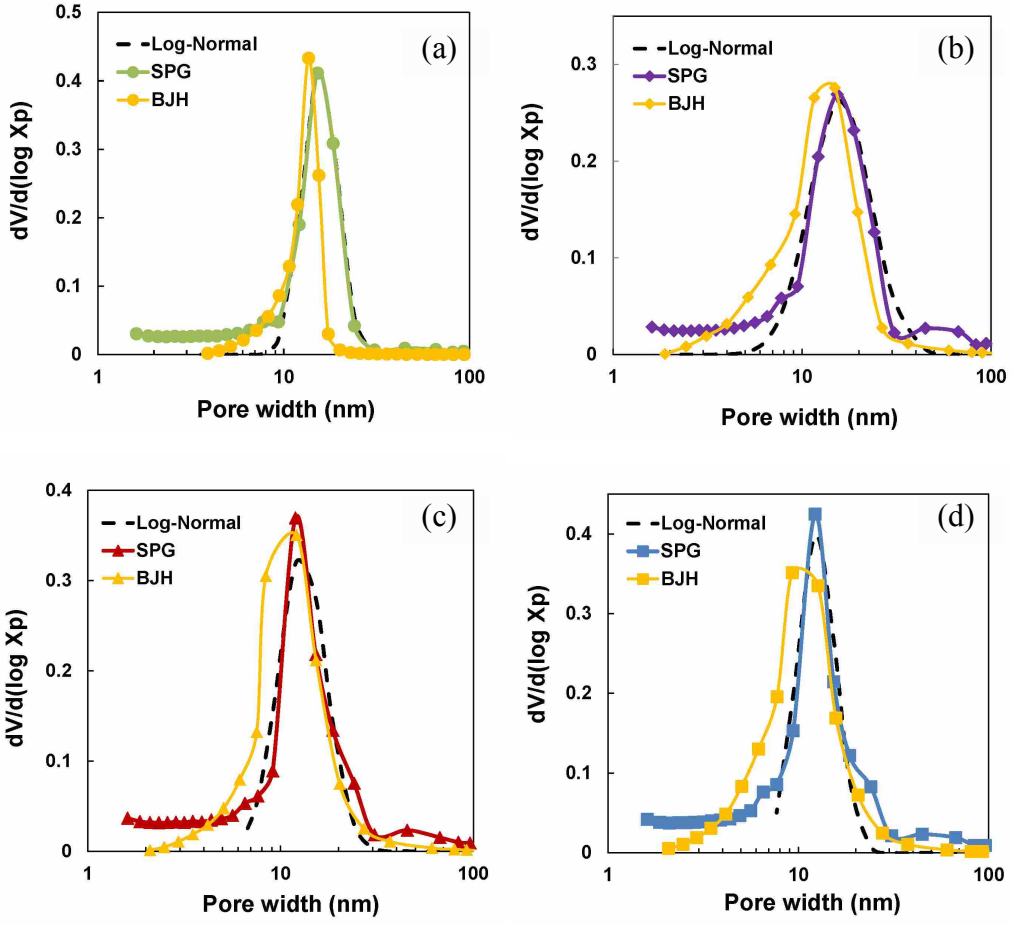

Figure 3.7 Pore size distributions of different alumina samples: (a) Al-Iprop; (b) Al-Sbuto; (c) Al-AA (d) Al-SG

mesopore (APD > 10 nm) and relatively narrow PSD. The standard deviation obtained from the fitted log normal distribution of each sample follows the trends: Al-Sbuto > Al-SG ≈ Al-AA > Al-Iprop.

The two proposed structural factors derived from the SPG model, α for the surface to volume ratio, and β for the conversion from core pore volume V_k to adsorbed volume V_p, as well as the determination of coefficient (R^2) are listed in Table 3.3. For all four samples, α values are close to 1, indicating experimental surface areas of a rough surface are in good agreement with their projected geometric surface. On the other hand, the structural factor β is approximately 0.9 for all four samples.

Table 3.3 Structural factors for Al_2O_3 samples

Sample	α		β	
	Adsorp	Desorp.	Adsorp.	Desorp.
Al-Sbuto	0.936	0.908	0.900	0.900
Al-Iprop	1.057	0.944	0.885	0.877
Al-AA	0.993	0.975	0.893	0.893
Al-SG	0.982	0.963	0.893	0.893

3.4 Discussion

3.4.1 Pore geometry of alumina samples

It is well known that the transformation from boehmite to γ-alumina is topotactic[49] and, therefore, γ-alumina is likely to maintain the original morphology of the boehmite precursors. Depending on the preparation method and conditions, plate-like or lath-like boehmite crystallites are obtained.[50, 51] For alumina samples prepared from aluminum alkoxides (Al-Iprop and Al-Sbuto, Figure 3.4a and 3.4b), the observed morphology is consistent with the structure of the

boehmite precursor described in our previous studies.[30] Moreover, the 3D open scaffold structures observed for Al-Iprop and Al-Sbuto, are similar to those of the aluminas prepared by block copolymer templates[52] and room temperature ionic liquids,[53] although the structures of alkoxide-derived materials of this study are less regular. Apparently, an irregular porous system consisting of interpolate voids is formed in calcined Al-Iprop and Al-Sbuto solids having a random distribution of platelets of varying dimensions. The pore volumes obtained from N_2 adsorption measurements provide further evidence for the open stacking order observed in TEM images. Indeed, the extraordinarily large pore volumes of Al-Iprop and Al-Sbuto of 1.5 and 1.6 cm^3/g, are comparable to those of ordered mesoporous alumina prepared by Zhu et al.[52] via surfactant-induced fiber formation (SIFF). Zhu et al. attributed their large pore volumes to intercrystalline voids created by randomly stacked fibers. The large pore volumes in the present study for aluminas prepared from aluminum alkoxides can be attributed to similar open 3D stacking of alumina nanoslabs. On the other hand, for the two commercial alumina samples (Al-AA and Al-SG, Figures 3c and 3d), the more closely packed morphologies give rise to smaller fractions of intercrystalline voids, as confirmed by the relatively small pore volumes obtained in the N_2 adsorption measurements. In addition, according to IUPAC classification, the hysteresis loops for all four alumina samples are apparently composites of H1 and H3, indicating these alumina samples consist of plate-like particles and slit-like pores, consistent with the morphology observed in TEM micrographs. Therefore, for this particular porous system (generally typical of porous gamma aluminas), the proposed SPG model, based on the slit pore geometry constructed by parallel plates, is fundamentally more appropriate than the cylindrical model of the BJH method.

3.4.2 Pore size distribution of alumina samples

In the present study, no H2 behavior was observed; rather, the hysteresis observed for Al-Iprop (Figure 3.5) is almost identical to type H1, indicating relatively uniform pores are present in this solid. Isotherms of the other three alumina samples are apparently a composite of H1 and H3 (Figure 3.5), since the adsorption and desorption branches are parallel and the hysteresis loop isn't closed until P/P_0 approaches 1. These isotherm shapes are consistent with pores formed by the interstices between plate-like aggregates, consistent with the observations in the TEM micrographs. Given a slit geometry, condensation during adsorption is likely to be delayed. Thus, the adsorption branch is most probably not appropriate for PSD analysis of the samples in this study, while the desorption branch is the one of choice. Accordingly, the desorption branch was selected for PSD calculations for all four samples in the present study.

PSDs for all four alumina samples show well-defined peak shapes with good symmetry (Figure 3.7). Given its inherent advantages of symmetry and easy error analysis, the log normal distribution enables estimation of average pore size and pore size distribution for alumina samples. For all four samples, the calculated log normal distribution is fitted very well with the experimental data; indeed, the coefficient of determination (R^2) values are very close to 1 (Table 3.2). The relatively large mean pore widths (> 10 nm) are consistent with the results from a_s plots (Figure 3.6), i.e., at the high-pressure end of a_s plots, the slope continues to be relatively steep, indicating the presence of relatively large mesopores. As shown in the PSD plots (Figure 3.7), the width of the PSD peaks from BJH model and those from the SPG model are similar, indicating approximately the same pore size span. However, the centers of the peaks from the BJH model are all smaller than those from SPG model. According to the pore width values in Table 3.2, pore widths calculated from the BJH model are roughly 6-40% smaller than those

obtained by SPG model on both adsorption and desorption isotherm branches, consistent with the observation that the BJH model generally underestimates pore size [7, 14]. It is worth noting that with larger pore widths, the difference between the values from BJH and SPG models for each sample become more significant. Based on the APDs calculated using the desorption branch (Table 3.2), the relative difference is 20.7% for Al-Sbuto, while for the other three samples, the relative difference ranges from 6% to 13%.

The trend of the standard deviation on slit width calculated from the log normal distribution for all four samples (Table 3.2) is consistent with that of the corresponding nitrogen adsorption isotherm shape (Figure 3.5). The hysteresis loop of Al-Sbuto spans a wide range of relative pressure P/P_0 from ca. 0.65 to 0.99, suggesting that capillary condensation occurs over a wide range of pore sizes. In contrast, the hysteresis loop of Al-Iprop ranges from ca. 0.75 to 0.85, indicating that the capillary condensation takes place in mesopores with a fairly narrow distribution. For Al-AA and Al-SG, although their adsorption capacities are different, the starting and ending point of their hysteresis loops are essentially the same. As a result, the standard deviations of the pore size distributions are almost identical.

3.4.3 Structural factors

Values of α in the SPG model, the structural factor which accounts for deviations in the surface to volume ratio from that of a slab, are close to 1 for all four alumina samples (Table 3.3), indicating that the pore shapes of alumina samples in the present study are close to the ideal slit pore geometry in the proposed SPG model. It is important to note that the α values obtained during desorption from Al-AA and Al-SG are 0.975 and 0.963, respectively, showing excellent agreement between the experimental surface area of a rough surface and its projected geometric surface. This could be explained by the morphology observed in the TEM micrographs (Figure

3.2). Since Al-AA and Al-SG consists of overlapping platelets along one direction, pore walls are expected to be parallel. While somewhat random 3D stacking is observed from TEM for Al-Iprop, its α value of 0.944 is nevertheless consistent with largely parallel plates in all 3 dimensions; this result is consistent with the observation from TEM of uniformly thick slabs arranged perpendicular to those in the micrograph plane. The stacking for Al-Sbuto is apparently somewhat more random in three dimensions given its lower α value of 0.908. The more random stacking is also consistent with the TEM results and the wide PSD observed in Al-Sbuto sample (Figure 3.7b).

Values of the structural factor β, which accounts for effects of geometry and surface roughness in converting the core pore volume V_k to the adsorbed volume V_p, are close to 0.9 and thus for 3 samples 4-10% lower than for the corresponding α value but nevertheless close enough to 1 to be consistent with the proposed SPG model. It is worth noting that β value for each sample is smaller than its corresponding α value, which is explained by their respective physical meaning. Since β corrects for surface roughness in addition to the pore geometry, the 4-10% smaller values (relative to α) may provide a measure of the contribution from surface roughness. Indeed, the commonly accepted structure of γ-Al_2O_3 is the ideal spinel (space group Fd3m), and it contains oxygen ions in the 32e Wyckoff positions, which are approximately close packed, while twenty-one and a third aluminum cations and 8/3 aluminum vacancies are distributed over 16d octahedral and 8a tetrahedral sites.[54] Since three-fourths of the 16d octahedral sites in the Fd3m group are on the surface of the unit cell, these vacancies likely contribute measurably to surface roughness, especially in the case of materials at the nanoscale. That β values of the four alumina samples are approximately the same, suggesting their surface properties are very nearly the same, a reasonable conclusion considering that all four samples are

shown from XRD to be γ-alumina. This consistency also further supports the validity of the SPG model.

3.5 Conclusion

An new model for calculating the average pore size (APS), pore size distribution (PSD) and pore volume (PV) of large-pore (> 10 nm), mesoporous gamma aluminas, i.e. the Slit Pore Geometry (SPG) Model, is presented and validated from a comprehensive analysis of N_2 adsorption, XRD, and TEM data for four representative large-pore aluminas. Surface area from BET analysis and pore volume obtained using SPG analysis are in good agreement with values obtained via the CAM method. Average pore widths calculated from the SPG model are 10-30% larger than those from BJH model based on cylindrical pore geometry from analysis in both cases from the desorption branch. Thus, the BJH method is not appropriate for determination of PSD for large slit-like pores or for pores whose geometry varies significantly from cylinders.

The SPG model is recommended as the model of choice for PSD analysis of aluminas having large mesopores (d_{pore} > 10 nm). It may also be useful in general for PSD analysis of all mesoporous solids having slit-like pores (d_{pore} > 5 nm). Moreover, the use in the SPG model of the log normal PSD function provides inherent advantages of symmetry enabling accurate determination of APS and PSD and easy, standardized error analysis; moreover, it is applicable to any pore geometry. Furthermore, two structural factors derived from the SPG model, α and β, provide further insights in assessing structure and roughness of pores. The principal of using structural factors also has general application to all mesoporous geometries.

Based on the results of this and other recent studies, fundamentally based criteria are proposed for accurately determining pore volume, average pore size, and pore size distribution of a mesoporous material:

(1) Selection of an appropriate method for calculating PSD and of the appropriate form of the Kelvin equation should rely on knowledge of the primary particle and pore geometries obtained from other techniques, including XRD and TEM and from available literature on appropriate methods for solids of different pore geometry, e.g. BJH method for cylindrical pores, the SPG method for slit pores.

(2) Surface areas and pore volumes should be determined independently via a comparative adsorption method, e.g. CAM method.

(3) Selection of the appropriate hysteresis branch for PSD analysis should be based on accumulated knowledge from the literature of the known limitations of such analysis as dictated by isotherm type, hysteresis shape, solid type, and pore size range.

(4) Use in PSD calculations of appropriate structural factors relating pore radius to pore volume and surface area, which can provide greater insights into structural analysis of mesoporous materials of all geometries

(5) Use in PSD calculations of the volumetric log pore size distribution function, noting its advantages already mentioned and its almost universal application to mesoporous solids.

References

1. Gregg, S. J.; Sing, K. S. W., *Adsorption, surface area and porosity*. 2 ed.; Acanedic Press: London, 1982.
2. Thomas, J. M.; Thomas, W. J., *Principles and practice of heterogeneous catalysis*. 1 ed.; Wiley-VCH: New York 1996; p 676.
3. Lastoskie, C. M.; Quirke, N.; Gubbins, K. E., Structure of porous adsorbents: Analysis using density functional theory and molecular simulation. *Stud. Surf. Sci. Catal.* **1997,** *104* (Equilibria and Dynamics of Gas Adsorption on Heterogeneous Solid Surfaces), 745-775.
4. Rouquerol, F.; Rouquerol, J.; Sing, K., *Adsorption by powders and porous solids*. Academic Press: London, 1999.

5. Thomas, J. M.; Thomas, W. J., *Principles and practice of heterogeneous catalysis*. 1 ed.; Wiley-VCH: New York, 1996.

6. Hunter, R. J., *Foundations of colloid science*. 2 ed.; Oxford Press: U.S.A, 1990.

7. Lowell, S.; Shields, J. E.; Thomas, M. A.; Thomas, A., *Characterization of porous solids and powders*. Springer: 2006.

8. Kaneko, K., Determination of pore size and pore size distribution 1. Adsorbents and catalysts. *J. Membr. Sci.* **1994,** *96* (1+2), 59-89.

9. Groen, J. C.; Peffer, L. A. A.; Perez-Ramirez, J., Pore size determination in modified micro- and mesoporous materials. Pitfalls and limitations in gas adsorption data analysis. *Micropor. Mesopor. Mater.* **2003,** *60* (1-3), 1-17.

10. Jaroniec, M.; Kruk, M., Gas adsorption: A valuable tool for the pore size analysis and pore structure elucidation of ordered mesoporous materials. *Stud. Surf. Sci. Catal.* **2003,** *146* (Nanotechnology in Mesostructured Materials), 263-269.

11. Barrett, E. P.; Joyner, L. G.; Halenda, P. P., The determination of pore volume and area distribution in porous substance. I. Computations from nitrogen isotherms. *J. Am. Chem.Soc.* **1951,** *73*, 373-380.

12. Luisa Ojeda, M.; Marcos Esparza, J.; Campero, A.; Cordero, S.; Kornhauser, I.; Rojas, F., On comparing BJH and NLDFT pore-size distributions determined from N_2 sorption on sba-15 substrata. *Phys. Chem. Chem. Phys.* **2003,** *5* (9), 1859-1866.

13. Cranston, R. W.; Inkley, F. A., The determination of pure structures from nitrogen adsorption isotherms. *Adv. Catal.* **1957,** *9*, 143-54.

14. Groen, J. C.; Perez-Ramirez, J., Critical appraisal of mesopore characterization by adsorption analysis. *Appl. Catal., A* **2004,** *268* (1-2), 121-125.

15. Jaroniec, M.; Kruk, M.; Olivier, J. P., Standard nitrogen adsorption data for characterization of nanoporous silicas. *Langmuir* **1999,** *15* (16), 5410-5413.

16. Cejka, J.; Zilkova, N.; Rathousky, J.; Zukal, A., Nitrogen adsorption study of organized mesoporous alumina. *Phys. Chem. Chem. Phys.* **2001,** *3* (22), 5076-5081.

17. Cejka, J.; Zilkova, N.; Rathousky, J.; Zukal, A.; Jagiello, J., High-resolution adsorption of nitrogen on mesoporous alumina. *Langmuir* **2004,** *20* (18), 7532-9.

18. Sayari, A.; Liu, P.; Kruk, M.; Jaroniec, M., Characterization of large-pore MCM-41 molecular sieves obtained via hydrothermal restructuring. *Chem. Mater.* **1997,** *9* (11), 2499-2506.

19. Broekhoff, J. C. P.; De Boer, J. H., Pore systems in catalysts. X. Calculations of pore distributions from the adsorption branch of nitrogen sorption isotherms in the case of open cylindrical pores. 2. Applications. *J. Catal.* **1967,** *9* (1), 15-27.

20. Broekhoff, J. C. P.; De Boer, J. H., Pore systems in catalysts. Ix. Calculation of pore distributions from the adsorption branch of nitrogen sorption isotherms in the case of open cylindrical pores. 1. Fundamental equations. *J. Catal.* **1967,** *9* (1), 8-14.

21. Broekhoff, J. C. P.; De Boer, J. H., Pore systems in catalysts. Xiv. Calculation of the cumulative distribution functions for slit-shaped pores from the desorption branch of a nitrogen sorption isotherm. *J. Catal.* **1968,** *10* (4), 391-400.

22. Broekhoff, J. C. P.; De Boer, J. H., Pore systems in catalysts. Xiii. Pore distributions from the desorption branch of a nitrogen sorption isotherm in the case of cylindrical pores. 2. Applications. *J. Catal.* **1968,** *10* (4), 377-90.

23. De Boer, J. H.; Linsen, B. G.; Broekhoff, J. C. P.; Osinga, T. J., Pore systems in catalysts. Xv. Influence of the geometrical factor on the thickness curve measured on aerosil. *J. Catal.* **1968,** *11* (1), 46-53.

24. Kruk, M.; Jaroniec, M.; Sayari, A., Adsorption study of surface and structural properties of MCM-41 materials of different pore sizes. *J. Phys. Chem. B* **1997,** *101* (4), 583-589.

25. Kruk, M.; Jaroniec, M.; Sayari, A., Application of large pore MCM-41 molecular sieves to improve pore size analysis using nitrogen adsorption measurements. *Langmuir* **1997,** *13* (23), 6267-6273.

26. Kruk, M.; Jaroniec, M.; Sayari, A., Structural and surface properties of siliceous and titanium-modified hms molecular sieves. *Micropor. Mater.* **1997,** *9* (3,4), 173-183.

27. Jaroniec, M.; Solovyov, L. A., Improvement of the kruk-jaroniec-sayari method for pore size analysis of ordered silicas with cylindrical mesopores. *Langmuir* **2006,** *22* (16), 6757-6760.

28. Orr, C.; Dalla Valle, J. M., *Fine particle measurement*. Macmillan: New York, 1959.

29. Pierce, C., Computation of pore sizes from physical adsorption data. *J. Phys. Chem.* **1953,** *57*, 149-52.

30. Huang, B.; Bartholomew, C. H.; Smith, S. J.; Woodfield, B., Facile solvent-deficient synthesis of mesoporous gamma alumina with controlled pore structures. *Micropor. Mesopor. Mater.* **2013,** *165*, 70-78.

31. Woodfield, B. F.; Liu, S.; Boerio-Goates, J.; Liu, Q. Preparation of uniform nanoparticles of ultra-high purity metal oxides, mixed metal oxides, metals, and metal alloys. 2007-US4279, 2007098111, 20070216., 2007.

32. Bartholomew, C. H.; Woodfield, B. F.; Huang, B.; Olsen, R. E.; Astle, L. Method for making highly porous, stable metal oxide with a controlled pore structure. 2011-US29472, 2011119638, 20110322., 2011.

33. Smith, J. S.; Liu, S.; Liu, Q.; Olsen, R. E.; Rytting, M.; Selck, D.; Simmons, C.; Boerio-Goates, J.; Woodfield, B. F., Metal oxide nanoparticle synthesis via a robust "solvent-deficient" method. *Chem. Mater.* **2012**.

34. Sing, K. S. W., *Surface area determination*. Butterworths: London, 1970.

35. Ball, P. C.; Evans, R., Temperature dependence of gas adsorption on a mesoporous solid: Capillary criticality and hysteresis. *Langmuir* **1989,** *5* (3), 714-23.

36. Neimark, A. V.; Ravikovitch, P. I.; Vishnyakov, A., Adsorption hysteresis in nanopores. *Phys. Rev. E Stat. Phys., Plasmas, Fluids, Relat. Interdiscip. Top.* **2000,** *62* (2-A), R1493-R1496.

37. Neimark, A. V.; Ravikovitch, P. I., Capillary condensation in mms and pore structure characterization. *Micropor. Mesopor. Mater.* **2001,** *44-45*, 697-707.

38. Monson, P. A., Contact angles, pore condensation, and hysteresis: Insights from a simple molecular model. *Langmuir* **2008,** *24* (21), 12295-12302.

39. Thommes, M., Recent advances in the characterization of mesoporous materials by physical adsorption. *Annu. Rev. Nano Res.* **2010,** *3*, 515-555.

40. Liu, H.; Zhang, L.; Seaton, N. A., Sorption hysteresis as a probe of pore structure. *Langmuir* **1993,** *9* (10), 2576-82.

41. Rojas, F.; Kornhauser, I.; Felipe, C.; Esparza, J. M.; Cordero, S.; Dominguez, A.; Riccardo, J. L., Capillary condensation in heterogeneous mesoporous networks consisting of variable connectivity and pore-size correlation. *Phys. Chem. Chem. Phys.* **2002,** *4* (11), 2346-2355.

42. Niemark, A. V., Percolation theory of capillary hysteresis phenomena and its application for characterization of porous solids. *Stud. Surf. Sci. Catal.* **1991,** *62* (Charact. Porous Solids 2), 67-74.

43. Parlar, M.; Yortsos, Y. C., Percolation theory of vapor adsorption-desorption processes in porous materials. *J. Colloid Interface Sci.* **1988,** *124* (1), 162-76.

44. Halsey, G., Physical adsorption on nonuniform surfaces. *J. Chem. Phys.* **1948,** *16*, 931-7.

45. Innes, W. B., Use of a parallel plate model in calculation of pore-size distribution. *Anal. Chem.* **1957,** *29*, 1069-73.

46. Wheeler, A., *Catalysis*. Reinhold: New York, 1955.

47. Hald, A., *Statistical theory with engineering applications*. Wiley: New York, 1964.

48. Nobe, K.; Hamidy, M.; Chu, C., Pore-size distributions of copper oxide-alumina catalysts. *J. Chem. Eng. Data* **1971,** *16* (3), 327-31.

49. Wefers, K.; Misra, C., Alcoa technical paper no.19. **1987**.

50. Jolivet, J.-P.; Cassaignon, S.; Chaneac, C.; Chiche, D.; Tronc, E., Design of oxide nanoparticles by aqueous chemistry. *J. Sol-Gel Sci. Technol.* **2008,** *46* (3), 299-305.

51. Jolivet, J.-P.; Froidefond, C.; Pottier, A.; Chaneac, C.; Cassaignon, S.; Tronc, E.; Euzen, P., Size tailoring of oxide nanoparticles by precipitation in aqueous medium. A semi-quantitative modelling. *J. Mater. Chem.* **2004,** *14* (21), 3281-3288.

52. Zhu, H. Y.; Riches, J. D.; Barry, J. C., Gamma-alumina nanofibers prepared from aluminum hydrate with poly(ethylene oxide) surfactant. *Chem. Mater.* **2002,** *14* (5), 2086-2093.

Chapter 4

Facile solvent deficient synthesis of mesoporous γ-alumina with controlled pore structures

4.1 Introduction

This chapter reports a novel one-pot, synthetic method for the preparation of high surface area mesoporous aluminas having a wide range of pore sizes with narrow pore-size distributions. In general, this method involves two simple, room temperature steps: (1) mixing an aluminum salt (*e.g.,* aluminum nitrate, chloride, alkoxide, etc.) with a base (*e.g.,* ammonium bicarbonate, or a small quantity of water in the case of aluminum alkoxides) to initiate a solvent deficient reaction followed by (2) calcining the intermediate at elevated temperatures to obtain an alumina support. Nanoparticles in this process typically crystallize during the precipitation or hydrolysis step to a Boehmite precursor of a specific morphology which is condensed to γ-alumina during calcination, while all of the byproducts escape either during mixing or subsequently during calcination in the form of simple, common gases that can be easily trapped. It is worth noting that no additional surfactant, template or structure-directing agent is used in this synthesis; this greatly reduces cost and environmental impact. The final product, after calcination at 700°C for 2 h, consists of nanostructured γ-alumina having a surface area from 210 to 320 m^2/g, a pore diameter in the range of 6-18 nm, a relatively narrow pore size distribution, and a pore volume ranging from 0.4 cm^3/g to 1.7 cm^3/g. These support materials have the potential of lowering catalyst cost and improving catalyst performance for many different catalytic applications,

including chemicals manufacture, petroleum refining, automotive emissions control, VOC emissions control, and Fischer-Tropsch and methanol syntheses.

4.2 Experimental Section

4.2.1 Materials

Aluminum nitrate nonahydrate ($Al(NO_3)_3 \cdot 9H_2O$), aluminum chloride hexahydrate ($AlCl_3 \cdot 6H_2O$), aluminum iso-propoxide ($Al(OCH(CH_3)_2)_3$), aluminum sec-butoxide ($Al(OCH(CH_3)CH_2CH_3)_3$), and ammonium bicarbonate (NH_4HCO_3) were purchased from Alfa Aesar and used as received without purification. Deionized water was used in all the synthesis. All glassware was cleaned with nitric acid, rinsed thoroughly and dried before use.

4.2.2 Support Synthesis

A typical synthesis involves formation of precursors followed by thermal treatment.[1-3] For inorganic sources, the solid metal salt (aluminum nitrate and aluminum chloride) and a stoichiometric amount of solid base ammonium bicarbonate (a NH_4HCO_3 to Al molar ratio of 3 to 1) were intimately mixed with a mortar and pestle to facilitate the initially solvent-free, solid-state reaction. Waters of hydration present in the starting materials were released and the mixture was wetted and assumes a pasty consistency. A small amount of water could be added to facilitate mixing of the slurry, but a solvent deficient environment must be maintained. For example, 22.516 g of $Al(NO_3)_3 \cdot 9H_2O$ and 14.235 g of NH_4HCO_3, were mixed in a mortar and ground vigorously by a pestle at room temperature for 20 minutes. The resultant intermediate, or precursor, was subsequently thermally treated in a muffle furnace in air at 700°C for 2 hours. A ramp rate of 2.33 °C/min was used to (1) avoid rapid dehydration to ensure uniform pore construction and (2) ensure uniform heat transfer to achieve better homogeneity and avoid rapid grain growth.

As for the aluminum alkoxides, such as aluminum iso-propoxide and aluminum sec-butoxide, these starting materials were hydrolyzed to obtain precursors by adding water, which was considered as a base in this procedure, with fixed water to aluminum molar ratio of 5 to 1 while grinding. For instance, 24.158 g of aluminum sec-butoxide was mixed with 8.83 ml of distilled water using a mortar and pestle for 15 minutes. The resultant white gel-like intermediate, or precursor, was subsequently thermally treated in a muffle furnace in air at 700°C for 2 hours with a ramp rate of 2.33 °C/min.

It is important to emphasize the solvent deficient environment used in our synthetic approach. When aluminnum nitrate and aluminum chloride are used as aluminum salts in a typical solvent system assisted by anionic or cationic surfactants, the water to aluminum molar ratios are reported to be at least 40 or 50 to 1.[4] In this study, however, the water to aluminum molar ratios were 9 and 5 for aluminum inorganic salts and aluminum alkoxides, respectively.

The final samples were labeled, starting with a prefix of Al followed by the type of aluminum salts (N, Cl, Iprop and Sbuto, which refer to aluminum nitrate nonahydrate, aluminum chloride hexahydrate, aluminum iso-propoxide and aluminum sec-butoxide, respectively). For example, Al-N refers to alumina sample prepared from $Al(NO_3)_3 \cdot 9H_2O$ calcined at 700°C for 2 hours in air.

4.2.3 Characterization

The structure of each sample was determined by powder X-ray diffraction (XRD) on a Panalytical X'Pert Pro X-ray diffractometer with Cu Kα radiation (λ=0.15418 nm) at a scanning rate of $0.02°s^{-1}$ in the 2θ ranges from 10° to 80°. A fixed power source was used (40 kV, 40 mA). All alumina precursors were dried at room temperature over night before the measurements. Crystallite sizes were estimated using the Scherrer formula for size-related peak broadening.

The morphology of the samples was observed with a FEI Philips Tecnai F30 transmission electron microscope (TEM) operating at 300 kV or a FEI Philips Technai F20 Analytical STEM operating at 200 kV. Specimens were prepared by dispersing samples in ethanol, sonicating in a water bath for 1 hour and then placing a drop of the diluted solution on a carbon film supported by a 200 mesh Cu grid (Ted-Pella Inc.).

Nitrogen adsorption analysis was carried out using a Micromerictics Tristar 3020 apparatus at -196 °C. Samples were degassed at 200 °C with nitrogen flow over night prior to the measurements. Specific surface area (SA) was calculated by the Brunauner-Emmett-Teller (BET) method, using a P/P_0 range between 0.05 and 0.2.[5] Pore volume (PV) was calculated from the adsorption isotherm at the relative pressure of 0.98 and mean pore diameter (MPD) were determined by the Barrett-Joyner-Helenda (BJH) method using either adsorption branch or desorption branch depending on the isotherm hysteresis type.[6] Thus, adsorption branch was used for Al-N and Al-Cl samples, whereas desorption branch was used for Al-Iprop and Al-Sbuto. Pore size distribution and mesopore volume were calculated from the adsorption and desorption data using a newly developed method involving slit geometry for the Kelvin equation and structural corrections for area and volume, while fitting the data to a log normal distribution function.[7-9]

Gases released during calcination of each precursor were identified though tandem TG/DTA-MS analyses. Thermogravimetric and differential-temperature analyses (TG/DTA) were performed using a Netzsch STA 409PC instrument. Mass spectrometry (MS) measurements were collected in tandem with the TG/DTA measurements by attaching a miniature quadrupole MS unit built in-house to the gaseous vent line of the Netzsch TG/DTA instrument.[10] For these experiments, roughly 50 mg of dried precursor material uncalcined was loaded onto a platinum

pan and heated from room temperature to 700°C under a 20 mL/min He gas flow with a temperature ramp of 3°C/min.

4.3 Results and discussion

The wide-angle XRD patterns of alumina precursors and calcined samples are shown in Figure 4.1. Ammonium nitrate (JCPDS card 00-001-0809) and ammonium chloride (JCPDS card 00-002-0887) peaks are readily observed in Al-N and Al-Cl samples, respectively, suggesting they are intermediates formed from aluminum nitrate and chloride during grinding and mixing

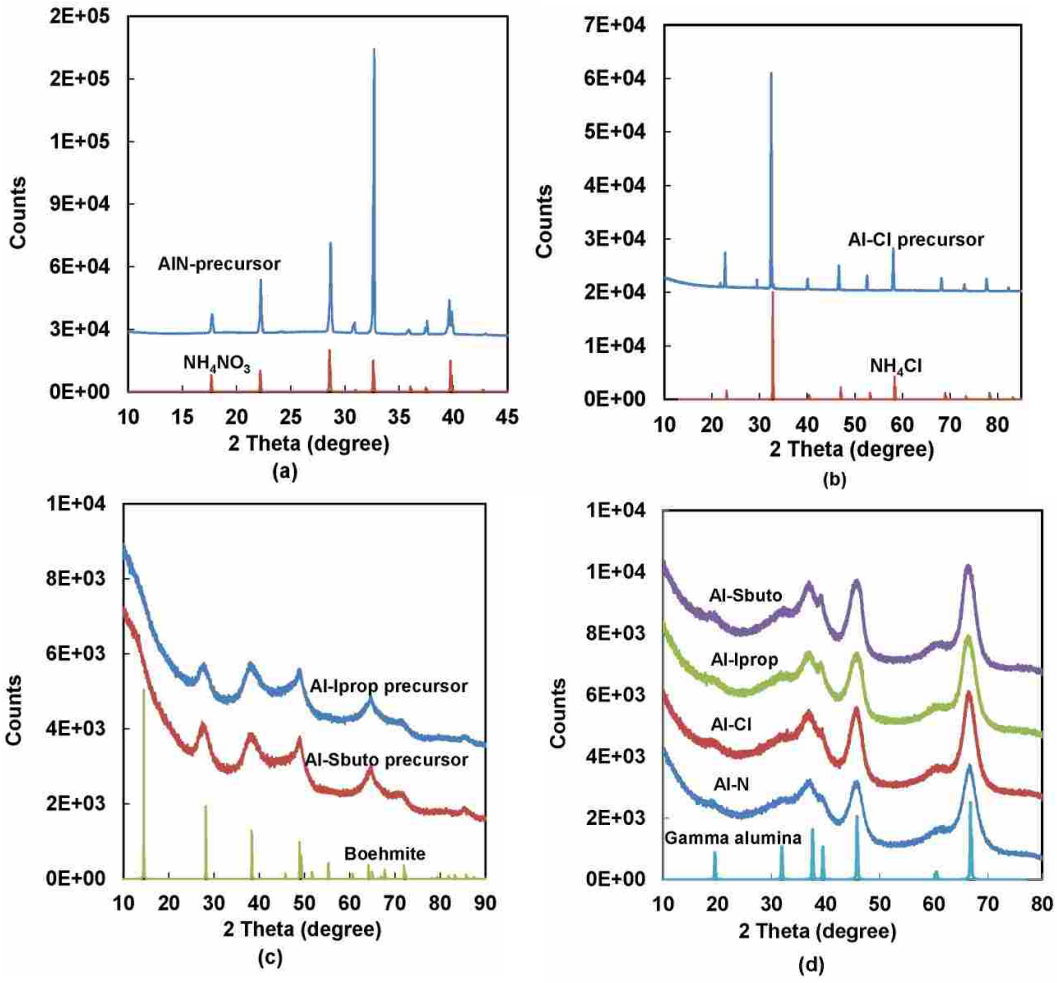

Figure 4.1 XRD patterns of Al_2O_3 precursors before calcination and sample after calcination at 700°C for 2h. (a) Al-N precursor, (b) Al-Cl precursor, (c) Al-Iprop and Al-Sbuto precursors (d) calcined alumina samples obtained from different aluminum salts.

(Figure 4.1a and 4.1b). For aluminas prepared from aluminum alkoxides, boehmite (AlOOH) (JCPDS card 04-013-2972) is the precursor after the hydrolysis but before thermal treatment (Figure 4.1c). After calcination at 700°C in air, the XRD patterns (Figure 4.1d) show peaks characteristic of γ-alumina (JCPDS card 00-029-0063). The seven peaks of gamma alumina can be indexed to the (111), (220), (311), (222), (400), (511), (440) reflections. The diffraction peaks of Al-N and Al-Cl are weaker and broader than the ones of Al-Iprop and Al-Sbuto, which suggest that the latter two have better crystallinity. The average diameters of these four samples calculated by the Scherrer formula based on the (440) peaks are all about 4 nm.

TGA-MS profiles for as-made alumina precursors provide insights into the reaction pathway. Figure 4.2a shows two-mass-loss steps for alumina precursor containing ammonium nitrate. The weight loss of around 30 wt.% between 50 and 100 °C is attributed to desorption of physically adsorbed water and CO_2 gas formed during the reaction, which is confirmed by the mass spectrum peaks (1,17,18 and 44 amu for H^+, OH^-, H_2O and CO_2, respectively) in the same temperature range. The second significant weight loss at around 250°C is due to the decomposition of ammonium nitrate formed in the reaction, which is also confirmed by the mass spectrum (30 and 44 amu for NO and N_2O gas, respectively)[1] and consistent with XRD results. The same trends are observed in Figure 4.2b for the Al-Cl precursor, however, the mass spectrum does not show a peak expected at appoximately 280 °C, which would be due to decomposition of ammonium chloride. This is explained by the re-formation of ammonium chloride in the capillary connection between the TGA and MS.

In the case of alumina alkoxides precursors, there is only one major weight loss peak. In Figure 4.2c, 18, 43 and 59 amu peaks for H_2O, $(CH_3)_2CH^+$ and $(CH_3)_2CHO^+$, respectively, are observed as isopropanol fragments; in Figure 3.2d, 18, 45, 59 and 73 peaks for H_2O,

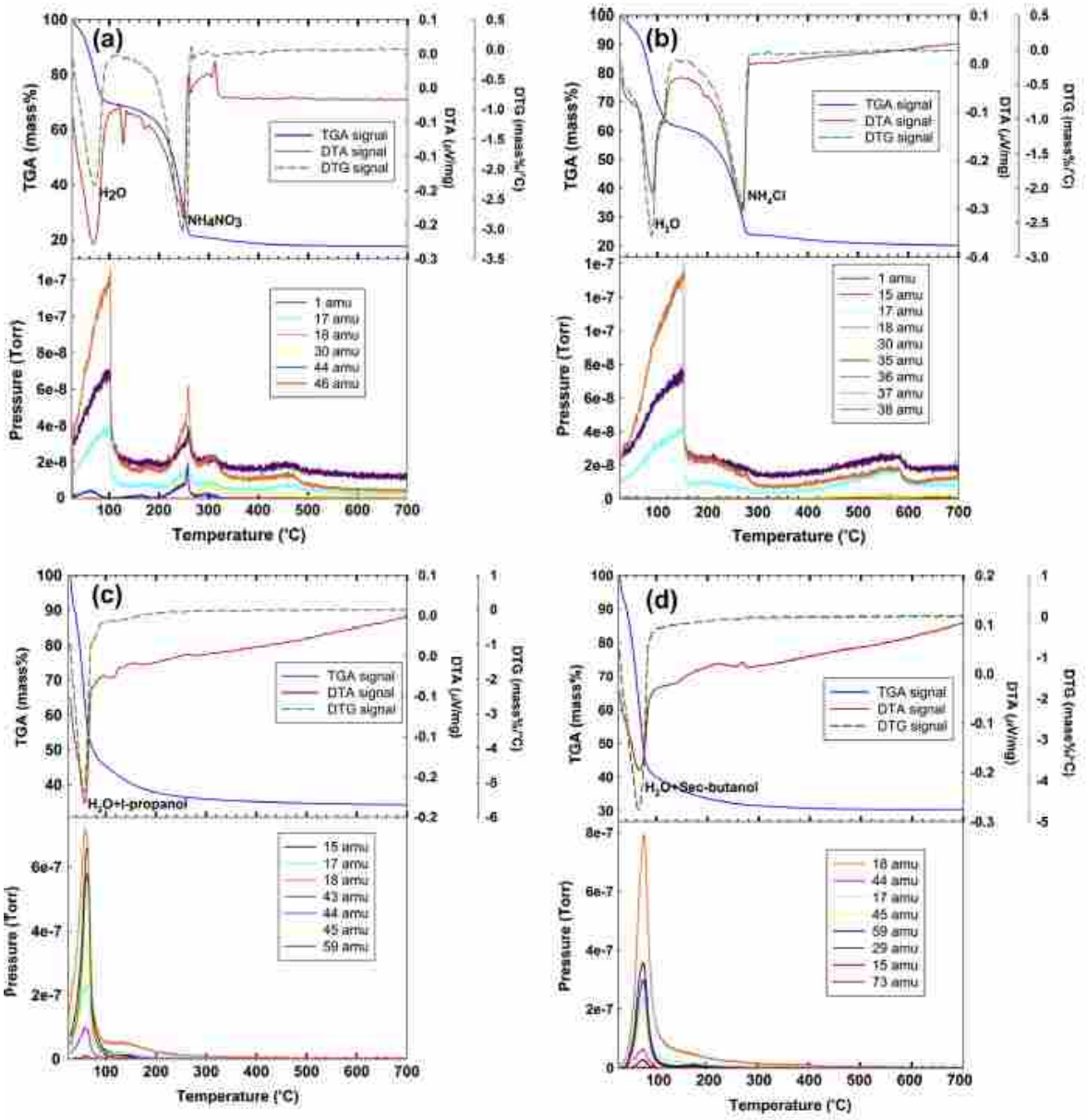

Figure 4.2 TGA–MS spectrum for precursors obtained from different aluminum salts. (a) Al–N, (b) Al–Cl, (c) Al–Iprop and (d) Al–Sbuto

CH_3CHOH^+, $CH_3CH_2CHOH^+$ and $CH_3CH_2CH(CH_3)O^+$, respectively, are observed as sec-butanol fragments, indicating that the weight loss is due to the evaporation of water and the corresponding alcohol from the hydrolysis. It is important to emphasize that if the calcination

were carried out under nitrogen flow using cold traps, the byproducts could be easily recovered. Commercially, this practice would substantially reduce operating cost and hazardous air emissions.

Table 4.1 Al_2O_3 samples made from different aluminum salts calcined at 700 °C for 2h [a]

Sample	Surface area (m^2/g)	Pore volume (cm^3/g)	Pore Diameter [b] (nm)		Peak Width [b] (nm)	
			Adsorp.	Desorp.	Adsorp.	Desorp.
Al-N	242	0.39	6.4	5.2	3.2	2.7
Al-Cl	227	0.52	10.4	7.9	3.3	2.7
Al-Iprop	314	1.72	29.3	18.7	3.1	2.9
Al-Sbuto	317	1.60	29.4	10.1 & 18.0	4.0	3.0

a. Data are averages of several runs determined by N_2 adsorption at 77 K
b. Calculated using a newly developed method involving slit geometry for the Kelvin equation and structural corrections for area and volume, while fitting the data to a log normal distribution function

Figure 4.3 shows the TEM images of alumina samples prepared from different aluminum salts. For samples prepared from aluminum nitrate and chloride, primary particles appear to be faceted hexagonal plates 8-12 nm in diameter, stacked fairly tightly. We hypothesize that the key to formation of such small, uniform γ-Al_2O_3 nanoparticles is a spatially constrained, solvent-deficient environment that controls the grain growth of the precipitate. Images for Al-Iprop and Al-Sbuto show that the primary particles are plate-like and loosely stacked. At lower magnification, their morphology looks like disordered nanofibers embedded in wormlike porous networks. The "fibers" appear to have a length of ca. 50 nm and a diameter ca. 4 nm, which is very similar to a fibrious γ-alumina prepared by block copolymer template[11] or by room temperature ionic liquids.[12] However, with increased magnification, plate-like or slit-like particles are clearly displayed. Thus, we conclude that what might appear to be fiber like shapes

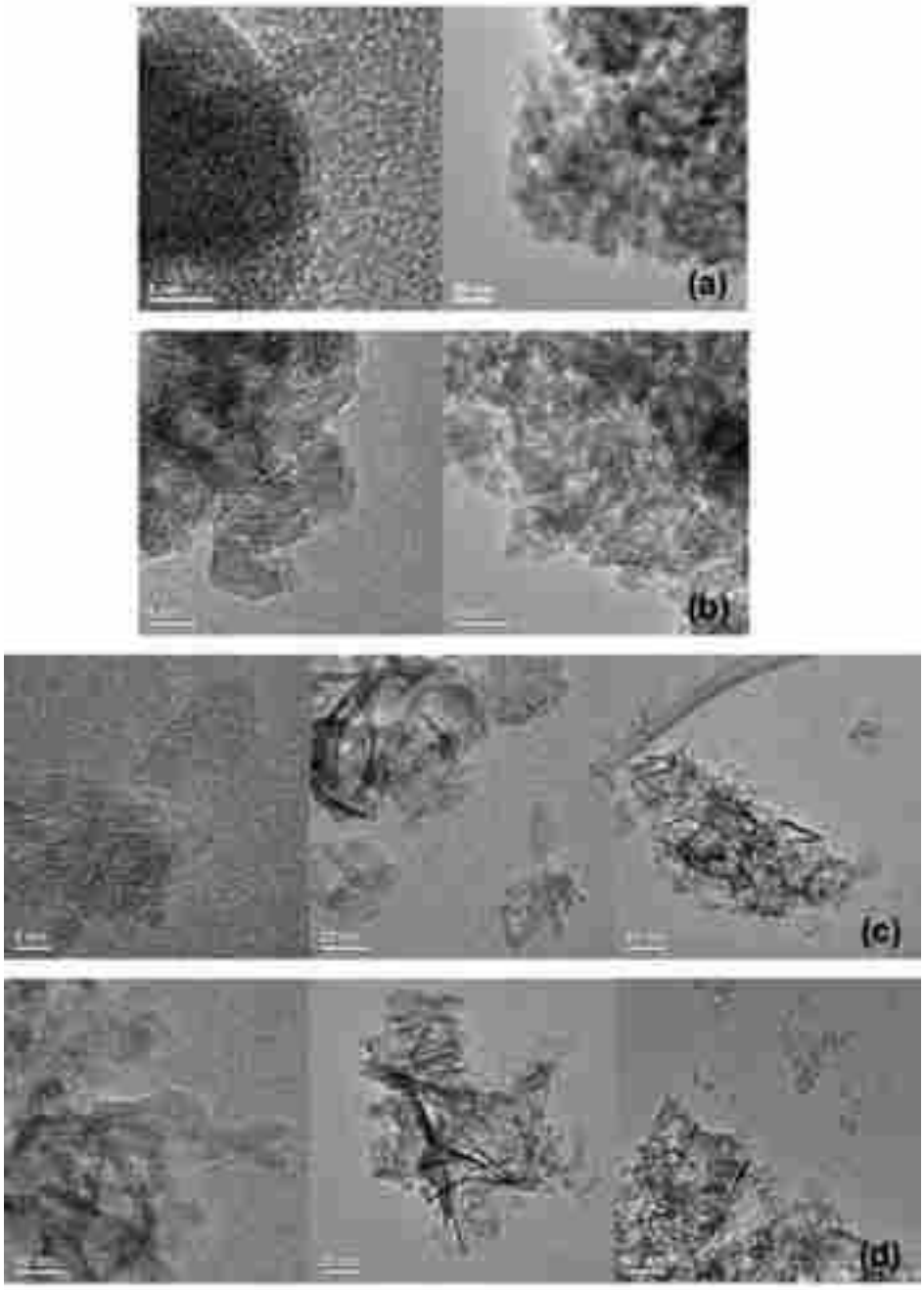

Figure 4.3. TEM images of γ-alumina sample after calcination at 700°C for 2h. (a) Al-N, (b) Al-Cl, (c) Al-Iprop and (d) Al-Sbuto.

are instead plate-like aggregates perpendicular to the electron beam, consistent with an open, randomly 3-D stacking effect and with their high pore volumes (see Table 4.1).

Figure 4.4 shows the nitrogen adsorption-desorption isotherms and pore size distribution curves of the calcined alumina samples obtained from different aluminum salts, while their textural properties are summarized in Table 4.1. It is noteworthy that the PSD calculation for Al-N and Al-Cl samples are based on the desorption branch of the isotherm because a hysteresis loop starting at a P/P_0 of 0.42 or less may be a result of an artifact.[13, 14] In the case of Al-Iprop and Al-Sbuto samples, the desorption branch is favored.[6] More detail and further discussion will be provided in our pore size calculation paper.[33] All the isotherms are type IV with a hysteresis loop indicating the presence of mesopores. For Al-N and Al-Cl samples, the hysteresis loops are a composite of H2 and H3, suggesting they may have pore connectivity with channel-like or ink-bottle pores. The pore sizes of these two samples are small (6 and 10 nm, respectively) and the pore size distributions are fairly narrow (peak widths of 3 nm), which are consistent with the uniform sized, tightly stacked plates observed in TEM. The hysteresis loops for Al-Iprop and Al-Sbuto are apparently a composite of H1 and H3, indicating that they have slit-shape pores or plate-like particles, consistent with the TEM results. The surface areas of Al-Cl and Al-N (227 and 242 m^2/g) are comparable with those of conventional Boehmite-derived aluminas heated to 700 °C for a few hours.[15] By contrast, BET surface areas of samples prepared from alkoxides (Al-Iprop and Al-Sbuto) are substantially higher (314 and 317 m^2/g). The N_2 adsorption capacities of Al-N and Al-Cl are in the range of 250 to 300 cm^3/g STP, whereas those for aluminas prepared from alkoxides are in the range of 1100 cm^3/g STP. N_2 adsorption capacity is, of course, proportional to pore volume.[5] Thus, the extraordinary large nitrogen adsorption uptakes by the alumina samples synthesized from aluminum alkoxides are consistent with their large pore volumes observed in this study. Indeed, the pore volumes of Al-Iprop and Al-Sbuto of approximately 1.7 cm^3/g, are comparable to the extraordinarily large pore volume of ordered

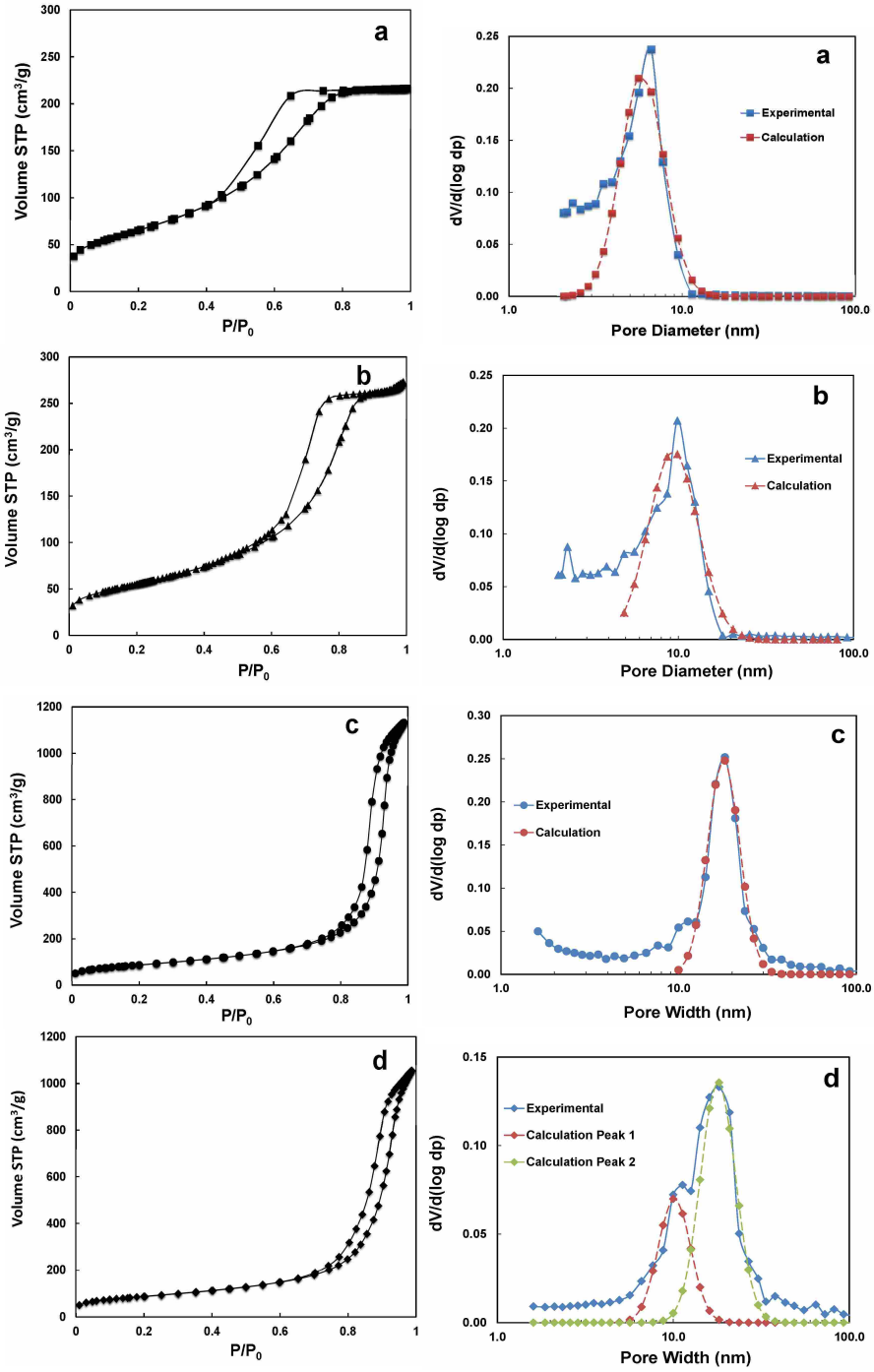

Figure 4.4. N_2 adsorption/desorption isotherms and pore size distributions of γ-aluminas after calcination at 700°C for 2h. (a) Al-N, (b) Al-Cl, (c) Al-Iprop and (d) Al-Sbuto. PSD for (a) and (b) are based on adsorption branch, PSD for (c) and (d) are based on desorption branch.

mesoporous alumina prepared by Zhu et al.[11] via surfactant-induced fiber formation (SIFF). We conclude similarly to Zhu et al., that the large pore volumes of this study can be attributed to intercrystallite voids created by randomly stacked alumina nanoslabs.

It is noteworthy that the bimodal distribution observed in this study for Al-Sbuto prepared using our simple one-pot procedure is similar to those prepared by a sophisticated ionic liquid synthesis,[12] which distribution was attributed to a scaffold structure of alumina consisting of a wormlike motif with intercrystallite voids. The large differences in pore sizes calculated from different branches of isotherms for aluminas prepared from aluminum alkoxides also indicate the presence of pore slit constrictions. The lower pore width of the desorption loop is expected, since the desorption process is limited by constriction diameters.[6] We postulate that given the absence of a surfactant additive in our synthesis, there could nevertheless be a self-templating effect induced by the alcohol formed in the hydrolysis. Thus, in a solvent deficient environment provided by low H_2O to Al molar ratio (5:1), these alcohols could act as surfactant or structure-directing agent, similar to that reported in the alumina synthesis using ionic liquids.[12] Alternatively, templating might occur via an alcohol-evaporation-induced self-assembly (EISA) mechanism.[16]

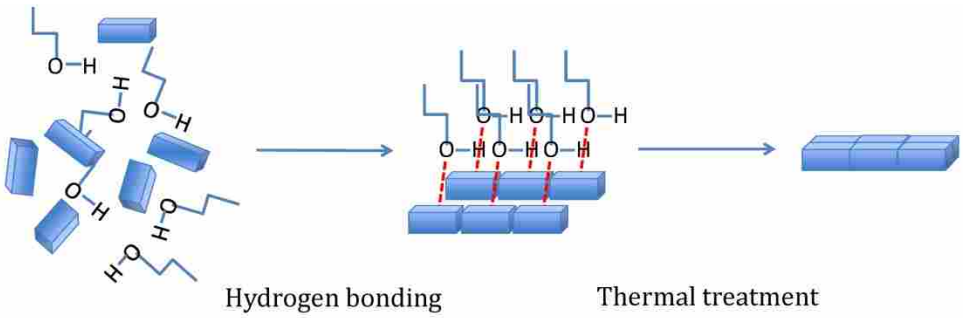

Figure 4.5. Schematic illustration of the self-templating mechanism. The oxide groups of the alcohol adsorb to and cover the surface of the layered boehmite crystallite, while the alky chains extended away from the surface, thus acting as a surfactant. The boehmite crystallites tend to grow in two dimensions and thus form larger γ-alumina nanoplates.

It should be emphasized that the mesopore diameters of Al-Iprop and Al-Sbuto are much larger than the molecular size of alcohols evolved in the synthesis, which is contrary to the conventional view of template synthesis. As shown in Figure 4.5, we speculate in a manner similar to the SIFF process, the oxide groups of the alcohol adsorb to and cover the surface of the layered boehmite crystallite, while the alky chains extended away from the surface, thus acting as a surfactant. It is believed that hydrogen bonding between oxide groups and the boehmite surface would reduce the free energy of the crystallite with low dimensions. Therefore, the boehmite crystallites tend to grow in two dimensions and are condensed to larger γ-alumina crystallites of similar shape after elimination of H_2O in the subsequent calcination.

Table 4.2 Al_2O_3 samples obtained from aluminum salts calcined at 1100°C for 2h [a]

Sample	Surface area (m^2/g)	Pore volume (cm^3/g)	Pore Diameter [b] (nm)
Al-N	9	0.07	-
Al-Cl	10	0.05	-
Al-Iprop	95	0.60	30
Al-Sbuto	100	0.56	22

a. Data are averages of several runs determined by N_2 adsorption at 77 K
b. Calculated based on desorption branch using a newly developed method involving slit geometry for the Kelvin equation and structural corrections for area and volume, while fitting the data to a log normal distribution function

Another advantage of the alumina samples obtained from aluminum alkoxides using our synthetic approach is their good thermal stability. It is well known that high temperature induced sintering causes serious reduction of surface area and pore volume. However, as shown in Table 4.2, the alumina samples prepared from aluminum alkoxides still exhibit surface areas of approximately 100 m^2/g and a pore volume of about 0.6 cm^3/g after calcining at 1100°C for two hours. These results are again comparable with the sample prepared using the SIFF mechanism.[11]

Figure 4.6 shows the morphology of alumina samples prepared by our method after calcination at 1100°C for 2h. It is clear that Al-N and Al-Cl sample sintered into large single crystals, indicating their transformation into thermally stable, low surface area and porosity alpha phase. This phase transition starts at a temperature about 50-100 degrees lower in the literature.[17] This might due to the high Al-O-Al connectivity resulted from the spatially constrained, solvent-deficient environment. On the other hand, Al-Iprop and Al-Sbuto samples still retained their plate-like shape, but those plates seem to pile together rather than into the random 3D stacking shown in Figure 3c and 3d, which contribute to the low sintering propensity due to the large porosity and low contact area between the nano-plates. Therefore, the loss of surface area and

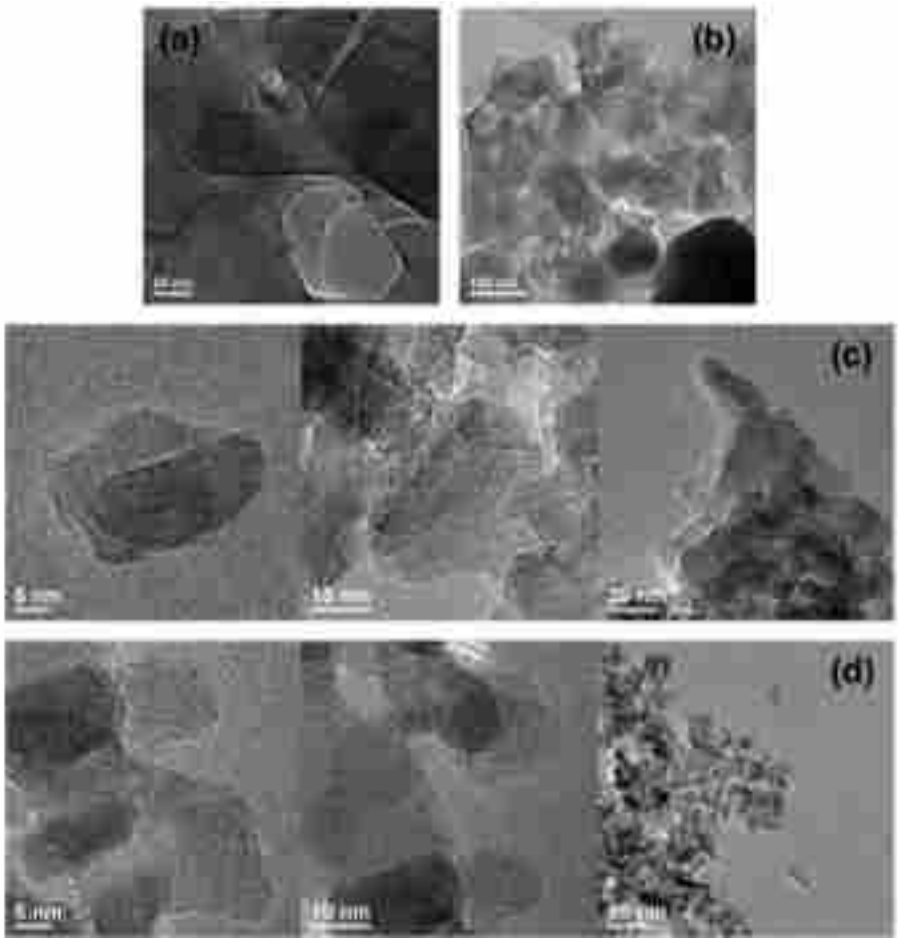

Figure 4.6. TEM images of γ-alumina sample after calcination at 1100°C for 2h. (a) Al-N, (b) Al-Cl, (c) Al-Iprop and (d) Al-Sbuto.

porosity is attributed to the collapse of scaffolding effects. The high resistance to sintering of Al-Iprop and Al-Sbuto samples is of great potential when they are used as catalyst supports in high temperature applications.

4.4 Conclusion

With this simple one-pot, solvent deficient synthesis strategy, we have successfully synthesized mesoporous γ-aluminas in several hours with different morphologies depending on the aluminum salts used. Closely packed uniform nanoparticles were obtained from aluminum inorganic salts, showing small pore size (6 and 10 nm) and a narrow pore size distribution. Randomly stacked nanoplates were obtained using aluminum alkoxides, showing large pore sizes (approximately 18 nm), large pore volumes (1.7 cm^3/g) and high resistance against sintering, which is comparable with aluminas prepared via SIFF or EISA mechanisms using triblock polymers or ionic liquids. Without any additional template or surfactant, our synthesis exhibits a self-templating effect and the alcohols formed in the hydrolysis reaction act as the structure directing agents. This time and cost effective approach not only contributes to the development of mesoporous alumina, but also offers an opportunity to control the pore structure and morphology. Furthermore, aluminas prepared by this method offer new possibilities for applications, such as automobile emission control, Fischer-Tropsch synthesis and oil-refining industry.

References

1. Smith, J. S.; Liu, S.; Liu, Q.; Olsen, R. E.; Rytting, M.; Selck, D.; Simmons, C.; Boerio-Goates, J.; Woodfield, B. F., Metal oxide nanoparticle synthesis via a robust "solvent-deficient" method. *Chem. Mater.* **2012**.

2. Bartholomew, C. H.; Woodfield, B. F.; Huang, B.; Olsen, R. E.; Astle, L. Method for making highly porous, stable metal oxide with a controlled pore structure. 2011-US29472 2011119638, 20110322., 2011.

3. Woodfield, B. F.; Liu, S.; Boerio-Goates, J.; Liu, Q. Preparation of uniform nanoparticles of ultra-high purity metal oxides, mixed metal oxides, metals, and metal alloys. 2007-US4279 2007098111, 20070216., 2007.

4. Cejka, J., Organized mesoporous alumina: Synthesis, structure and potential in catalysis. *Appl. Catal., A* **2003,** *254* (2), 327-338.

5. Gregg, S. J.; Sing, K. S. W., *Adsorption, surface area and porosity*. 2 ed.; Academic Press: London, 1982.

6. Rouquerol, F.; Rouquerol, J.; Sing, K., *Adsorption by powders and porous solids*. Academic Press: London, 1999.

7. Innes, W. B., Use of a parallel plate model in calculation of pore-size distribution. *Anal. Chem.* **1957,** *29*, 1069-73.

8. Nobe, K.; Hamidy, M.; Chu, C., Pore-size distributions of copper oxide-alumina catalysts. *J. Chem. Eng. Data* **1971,** *16* (3), 327-31.

9. Huang, B.; Bartholomew, C.; Woodfield, B., *Micropor. Mesopor. Mater.*

10. Selck, D. A.; Woodfield, B. F.; Boerio-Goates, J.; Austin, D. E., Simple, inexpensive mass spectrometric analyzer for thermogravimetry. *Rapid Commun. Mass Spectrom.* **2012,** *26* (1), 78-82.

11. Zhu, H. Y.; Riches, J. D.; Barry, J. C., Gamma-alumina nanofibers prepared from aluminum hydrate with poly(ethylene oxide) surfactant. *Chem. Mater.* **2002,** *14* (5), 2086-2093.

12. Park, H.; Yang, S. H.; Jun, Y. S.; Hong, W. H.; Kang, J. K., Facile route to synthesize large-mesoporous gamma-alumina by room temperature ionic liquids. *Chem. Mater.* **2007,** *19* (3), 535-542.

13. Groen, J. C.; Peffer, L. A. A.; Perez-Ramirez, J., Pore size determination in modified micro- and mesoporous materials. Pitfalls and limitations in gas adsorption data analysis. *Microporous Mesoporous Mater.* **2003,** *60* (1-3), 1-17.

14. Groen, J. C.; Perez-Ramirez, J., Critical appraisal of mesopore characterization by adsorption analysis. *Appl. Catal., A* **2004,** *268* (1-2), 121-125.

15. Bartholomew, C. H.; Farrauto, R. J., *Fundamentals of industrial catalytic processes*. 2 ed.; Wiley-AICHE: 2005.

16. Yang, P.; Zhao, D.; Margolese, D. I.; Chmelka, B. F.; Stucky, G. D., Generalized syntheses of large-pore mesoporous metal oxides with semicrystalline frameworks. *Nature (London)* **1998,** *396* (6707), 152-155.

17. Wefers, K.; Misra, C., Alcoa technical paper no.19. **1987**.

Chapter 5

Facile synthesis of mesoporous γ-alumina with tunable pore size: the effects of water to aluminum molar ratio in hydrolysis of aluminum alkoxides

5.1 Introduction

In Chapter 4, we reported a one-pot, facile solvent-deficient synthesis of MA without external SDAs.[1] In that synthesis, high surface area aluminas with 4-18 nm pores were obtained by varying the aluminum salt, although the method used was not capable of tuning pore structure from a single precursor. In this chapter, we report a new method for tuning average pore size of mesoporous γ-aluminas, prepared by the controlled hydrolysis of aluminum alkoxides. Calcined mesoporous γ-aluminas with high surface areas and large pore volumes are obtained, while average pore size can be tuned from 4 to 18 nm by varying the water to aluminum molar ratio in a solvent-deficient hydrolysis reaction. This simple method of preparing MA support materials has potential for lowering catalyst cost and improving catalyst performance for many different catalytic applications.

5.2 Experimental Section

5.2.1 Materials

Aluminum *sec*-butoxide ($Al(OCH(CH_3)CH_2CH_3)_3$) was purchased from Alfa Aesar and used as received without purification. Aluminumoxid C Degussa (denote as DC) was purchased from Sigma-Aldrich and used as reference materials for the comparative adsorption study. Deionized water was used in all the synthesis.

5.2.2 Supports Synthesis

A typical synthesis involves formation of precursors followed by thermal treatment.[2-4] For the aluminum alkoxides, the starting materials were hydrolyzed at room temperature to obtain precursors by adding water with different water to aluminum molar ratios (H_2O : Al = 2:1, 3:1, 5:1, 7:1, 10:1, 15:1) while grinding. For instance, 24.158 g of aluminum *sec*-butoxide was mixed with 8.83 ml of distilled water (H_2O : Al = 5:1) using a mortar and pestle for 15 minutes. The resultant white gel-like intermediate, or precursor, was subsequently thermally treated in a muffle furnace in air at 700 °C for 2 hours. A ramp rate of 2.33 °C/min was used to (1) avoid rapid dehydration and thus ensure uniform pore construction and (2) ensure uniform heat transfer to achieve better homogeneity and avoid rapid grain growth.

The final samples were labeled, starting with a prefix of Al followed by the type of aluminum salts (SB, which refers to aluminum *sec*-butoxide), calcination temperature and the corresponding water to aluminum molar ratio. For example, Al-SB700-3H_2O refers to the alumina sample prepared from aluminum *sec*-butoxide with a H_2O to Al molar ratio of 3:1 calcined at 700 °C for 2 hours in air. All the precursors are denoted without a calcination temperature. For instance, Al-SB-3H_2O refers to the precursor obtained from aluminum *sec*-butoxide with a H_2O to Al molar ratio of 3:1 before calcination.

5.2.3 Characterization

The structure of each sample was determined by powder X-ray diffraction (XRD) on a Panalytical X'Pert Pro X-ray diffractometer with Cu Kα radiation (λ=0.15418 nm) at a scanning rate of 0.02°s^{-1} in the 2θ ranges from 10° to 80°. A fixed power source was used (40 kV, 40 mA). All alumina precursors were dried at room temperature over night before the measurements. Crystallite sizes were estimated using the Scherrer formula for size-related peak broadening.

The morphology of the samples was observed with a FEI Philips Tecnai F30 transmission electron microscope (TEM) operating at 300 kV or a FEI Philips Technai F20 Analytical STEM operating at 200 kV. Specimens were prepared by dispersing samples in ethanol, sonicating in a water bath for 1 hour and then placing a drop of the diluted solution on a carbon film supported by a 200 mesh Cu grid (Ted-Pella Inc.).

Nitrogen adsorption analysis was carried out using a Micromeritics Tristar 3020 apparatus at -196 °C. Samples were degassed at 200 °C with nitrogen flow over night prior to the measurements. Specific surface area (SA) was calculated by the Brunauner-Emmett-Teller (BET) method, using a P/P_0 range between 0.05 and 0.2.[5] Pore volume (PV) was calculated from the adsorption isotherm at the relative pressure of 0.990 and average pore diameter (APD) were determined by the SPG model using either the adsorption branch or desorption branch depending on the isotherm hysteresis type.[6, 7] The adsorption branch was used for samples with a pore width lower than 10 nm, whereas desorption branch was used for those with a pore width above 10 nm. Pore size distribution (PSD) and mesopore volume were calculated from the adsorption and desorption data using a newly developed method involving slit pore geometry for the Kelvin equation and structural corrections for area and volume, while fitting the data to a log normal distribution function.[7]

Comparative adsorption method (CAM) or the α_s method was also employed to determine the total surface area, external surface area, and mesopore volume.[8] Since the aluminas in the present study were calcined at 700 °C, Degussa Aluminumoxid C was found suitable for the analysis of isotherms on porous γ-alumina because of its similar surface chemistry.[9-11]

Thermo gravimetric and differential-temperature analyses (TG/DTA) were performed using a Netzsch STA 409PC instrument. For these experiments, roughly 30 mg of dried precursor material uncalcined was loaded onto a platinum pan and heated from room temperature to 700 °C under a 20 mL/min He gas flow with a temperature ramp of 3 °C/min.

5.3 Results

5.3.1 XRD patterns

XRD patterns of as synthesized precursors and calcined alumina samples are shown in Figure 5.1. For as prepared precursors (Figure. 5.1a), characteristic peaks of boehmite (JCPDS card 04-013-2972) are shown. The six main peaks can be indexed to the (0 2 0), (1 2 0), (1 4 0), (0 5 1), (2 3 1), (2 5 1) reflections. With increased H_2O/Al ratio (up to 7), XRD peaks become narrower, indicating increased crystallite size. However, as the ratio is further increased, bayerite (JCPDS card 00-001-0287) peaks appear, suggesting that the precursor is a mixture of boehmite and bayerite. After calcination at 700 °C for 2 hours, all the precursors are transformed into γ-alumina. Characteristic peaks of γ-alumina (JCPDS card 00-029-0063) are observed. The seven peaks of gamma alumina can be indexed to the (1 1 1), (2 2 0), (3 1 1), (2 2 2), (4 0 0), (5 1 1), (4 4 0) reflections.

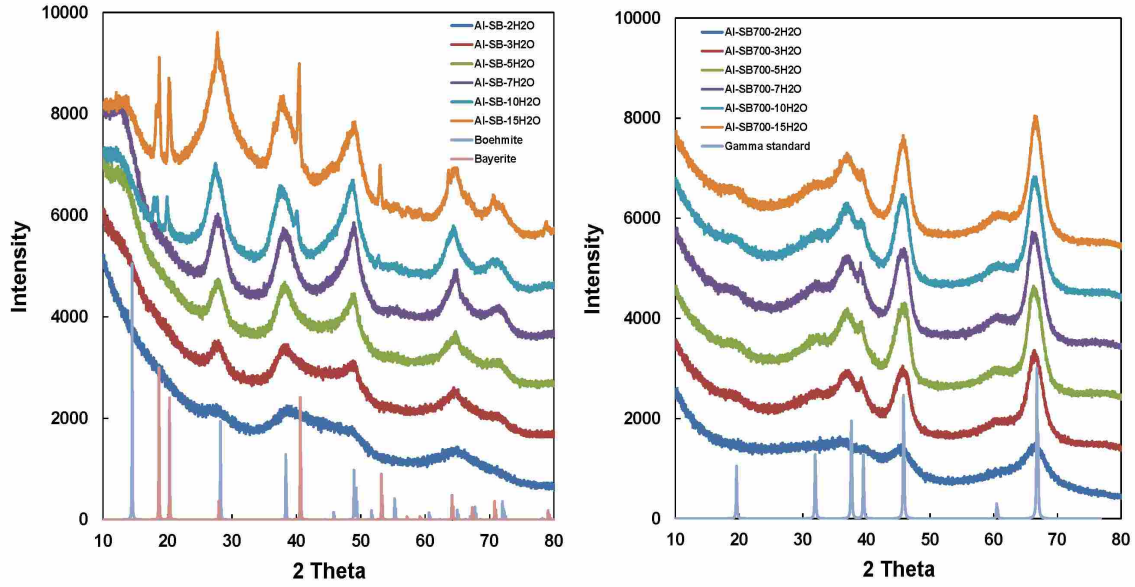

Figure 5.1 X-ray Diffraction patterns of (a) as synthesized precursors and (b) calcined alumina samples.

5.3.2 TEM images

Figure 5.2 shows the selected area electron diffraction (SAED) patterns of the precursor and calcined sample prepared with H_2O/Al molar ratio of 5. Characteristic ring patterns for boehmite and γ-alumina are observed for both precursor and calcined samples, respectively, consistent with the crystallinity observed in the XRD results.

The morphology of precursors prepared with different H_2O/Al molar ratios are shown in the TEM micrographs (Figure 5.3). For boehmite samples prepared with H_2O/Al = 2, aggregates of overlapping plates are observed. These plates have a length of 30-40 nm and a width of 20-30 nm. At higher magnification, these plates actually consist of smaller platelets with a particle size of 3-5 nm (Figure 5.3a). When the H_2O/Al ratio is increased to 5, plates and what appear to be rod-like crystallites with a length of *ca.* 50 nm are observed (Figure 5.3b). However, a careful examination of the micrograph at higher magnification shows a scaffold structure made of plates

with a length of *ca.* 50 nm, a width of *ca.* 30 nm, and edges of plates (not rods) perpendicular to the image plane of thickness of *ca.* 5-7 nm. When a large H_2O/Al ratio is used (H_2O/Al = 15), the obtained precursor shows a mixture of long fibers and thin sheets.

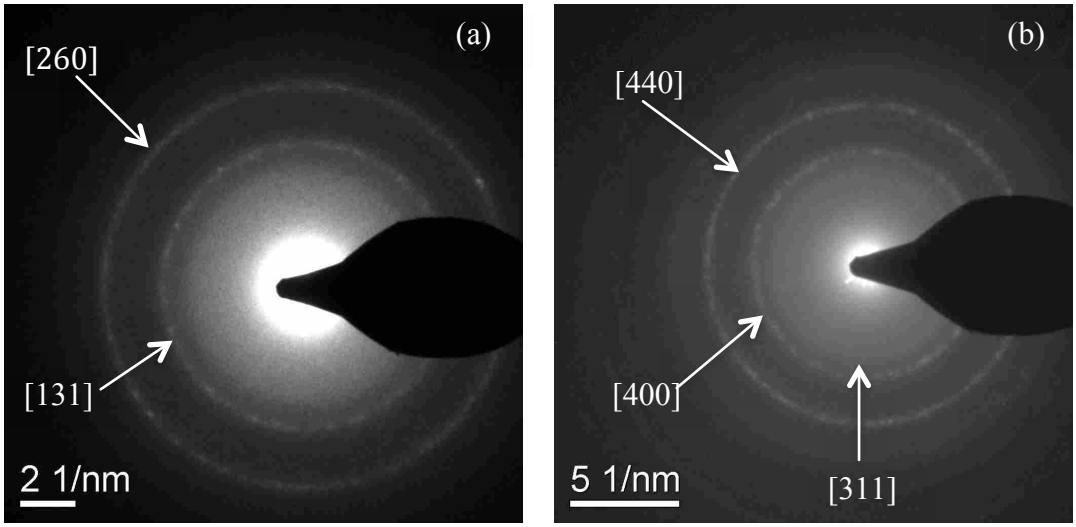

Figure 5.2 Selected area electron diffraction patterns of (a) as synthesized precursors and (b) calcined alumina samples prepared with H_2O/Al = 5.

Figure 5.4 shows the different morphologies of calcined γ-alumina samples prepared from aluminum *sec*-butoxide with different H_2O/Al molar ratios. For alumina obtained with an H_2O/Al molar ratio of 2 (Figure 5.4a), closely packed agglomerates of small slab-like boehmite crystallites having lengths and widths around 5-8 nm are observed. With a slightly increased H_2O/Al molar ratio (H_2O/Al = 3, Figure 5.4b), a lath-like morphology appears. Most of the lathes have a length of 8-10 nm and a width of 3-5 nm. When the H_2O/Al molar ratio is increased to 5 (Figure 5.4c), a rod-like morphology is suggested. Most of the "rods" have a length of *ca.* 30-40 nm and a width of *ca.* 3-5 nm. However, at higher magnification, a scaffold structure is observed similar to that of the corresponding precursors consisting of plates with a length of *ca.* 30-40 nm and edges of plates (not rods) perpendicular to the image plane of thickness of *ca.* 5-7 nm. At an H_2O/Al = 7 (Figure 5.4d), calcined γ-alumina samples are indeed rod-like with a

length of 20-30 nm and a width of 3-5 nm. However, with further increased H_2O/Al molar ratios (10 and 15, Figures 5.4e and 5.4f, respectively), the morphologies of the calcined samples resemble the ones observed from samples with small H_2O/Al molar ratios, *i.e.*, agglomerates of closely packed platelets.

.

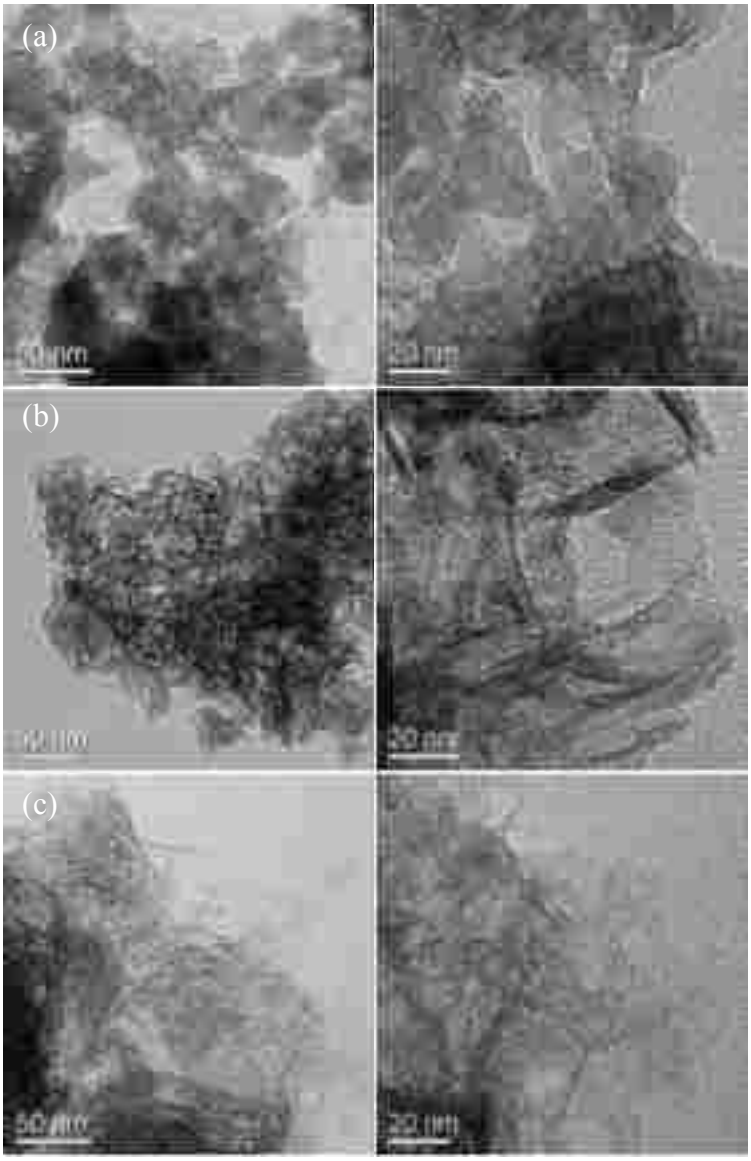

Figure 5.3. TEM images of boehmite precursors prepared with different H_2O/Al ratios: (a) H_2O/Al = 3; (b) H_2O/Al = 5; (c) H_2O/Al = 15.

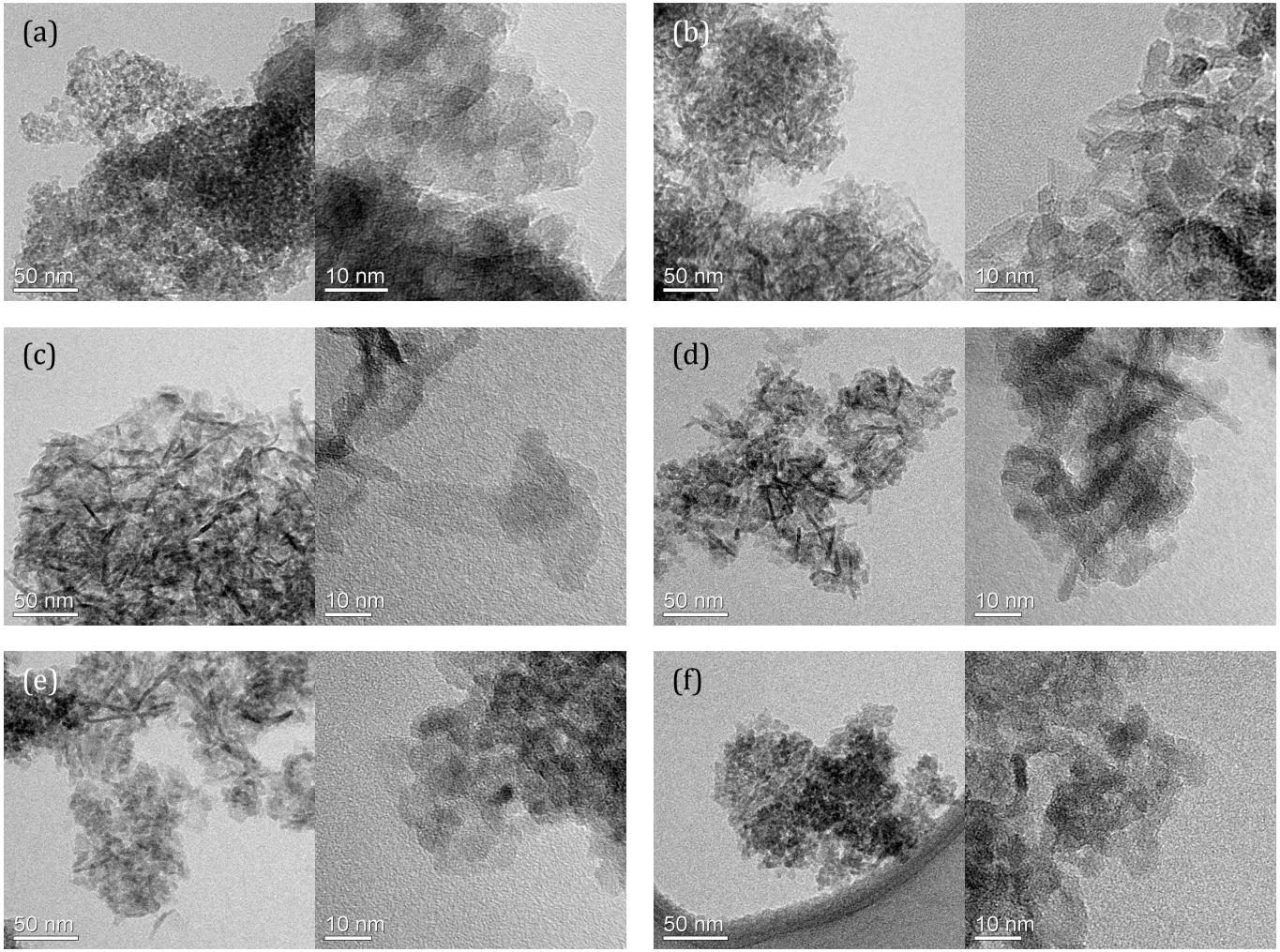

Figure 5.4 TEM images of γ-alumina samples prepared with different H_2O/Al ratios: (a) H_2O/Al = 2; (b) H_2O/Al = 3; (c) H_2O/Al = 5; (d) H_2O/Al = 7; (e) H_2O/Al = 10; (f) H_2O/Al = 15.

Table 5.1. Structural parameters of different Al_2O_3 samples calcined at 700 °C in air for 2 h [a]

Sample	S_{BET} [b] (m^2/g)	S_{tot} [c] (m^2/g)	S_{ext} [c] (m^2/g)	S_{meso} [c] (m^2/g)	V_{meso} [c] (m^2/g)	V_{sp} [d] (cm^3/g)	X_{SPG} [e] (nm)	σ [e]
Al-SB700-2H_2O	285	275	29	246	0.34	0.43	3.8	1.3
Al-SB700-3H_2O	316	311	106	205	0.88	1.16	13.8	1.4
Al-SB700-5H_2O	300	296	75	221	1.42	1.63	18.3	1.5
Al-SB700-7H_2O	308	305	66	238	1.36	1.54	14.9	1.3
Al-SB700-10H_2O	289	284	50	234	0.92	1.05	12.3	1.2
Al-SB700-15H_2O	239	234	20	214	0.47	0.53	6.5	1.1

a. Data are average values of several runs
b. BET surface area determined by N_2 adsorption at 77 K, calculated BET equation using P/P_0 ranges form 0.01-0.20
c. Total surface area, external surface area, mesopore area, mesopore volume calculated using α_s method, respectively
d. Pore volume obtained from single point method at $P/P_0 = 0.990$
e. Mean pore width and standard deviation obtained from slit pore geometry model using desorption branch

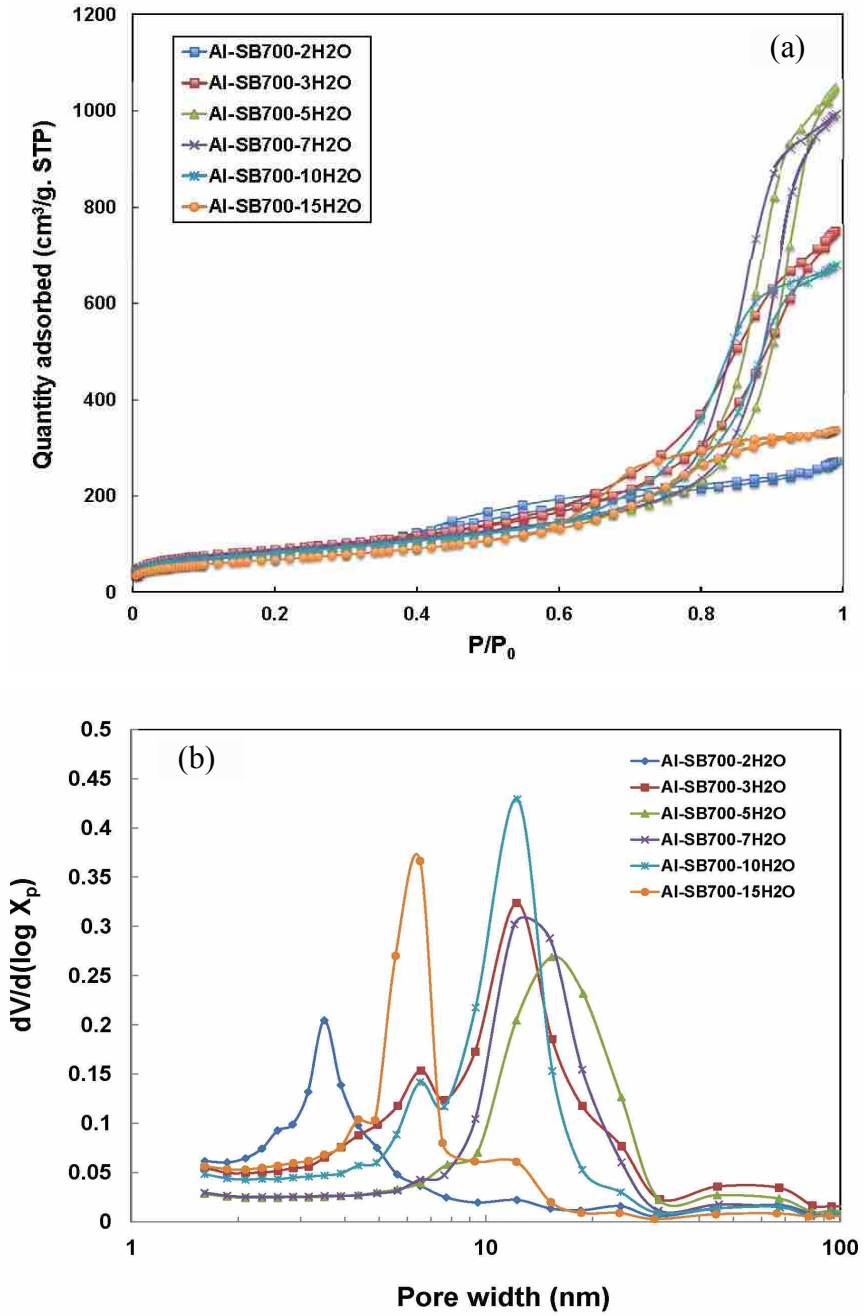

Figure 5.5 (a) N_2 adsorption/desorption isotherms of calcined alumina samples prepared with different H_2O/Al ratios; (b) Pore size distribution of calcined alumina samples prepared with different H_2O/Al ratios

5.3.3 N_2 adsorption

Figure 5.5 shows the nitrogen adsorption-desorption isotherms and pore size distributions of different calcined γ-alumina samples. Surface area, pore volume and pore size distributions of

the calcined γ-alumina samples are listed in Table 5.1. All isotherms are Type IV (IUPAC designation),[12] indicating the presence of mesopores. Hysteresis loops of all samples are apparently a composite of H1 and H3, indicating that they have slit-shape pores or plate-like particles.[6] The differences in H_2O/Al molar ratios induce significant changes in the textural characteristics of alumina. With a small increase in the H_2O/Al molar ratio (from 2 to 3), the hysteresis loops are shifted to higher P/Po indicating that capillary condensation occurs in larger mesopores and adsorption capacity increases markedly from 300 cm^3/g to 800 cm^3/g. As a result, the pore volume increases from 0.43 to 1.16 cm^3/g, and surface area increases from 281 to 316 m^2/g. Even more significant changes are observed by further increasing the H_2O/Al molar ratio to 5, the adsorption capacity reaches approximately 1100 cm^3/g and the pore volume is almost quintupled (1.63 cm^3/g). Above the limit of H_2O/Al = 5, water showed a detrimental effect on the adsorption capacity and pore volume. Pore volume shrinks from 1.63 cm^3/g (H_2O/Al = 5) to 1.54 cm^3/g at a H_2O/Al of 7, and further decreases to 1.05 and 0.53 cm^3/g for H_2O/Al = 10 and 15 respectively. Remarkable differences in pore size are also induced by the differences in H_2O/Al ratios. The mean pore width expands from 4 nm (H_2O/Al = 2) to 14 nm (H_2O/Al = 3) and reaches the maximum at 18 nm (H_2O/Al = 5). However, with further increased H_2O/Al molar ratios, average pore width of the calcined samples decreases.

5.3.4 Comparative adsorption method (CAM)

Figure 5.6 shows the comparative adsorption study (α_s plots) for the calcined alumina samples. For all samples, the low-pressure part of these plots exhibits excellent linearity starting from the lowest adsorption uptakes, and can be back extrapolated to the origin, indicating the absence of detectable micropores. The subsequent steep increase is due to the capillary condensation of nitrogen in mesopores. The onset of the steep increase for samples prepared with

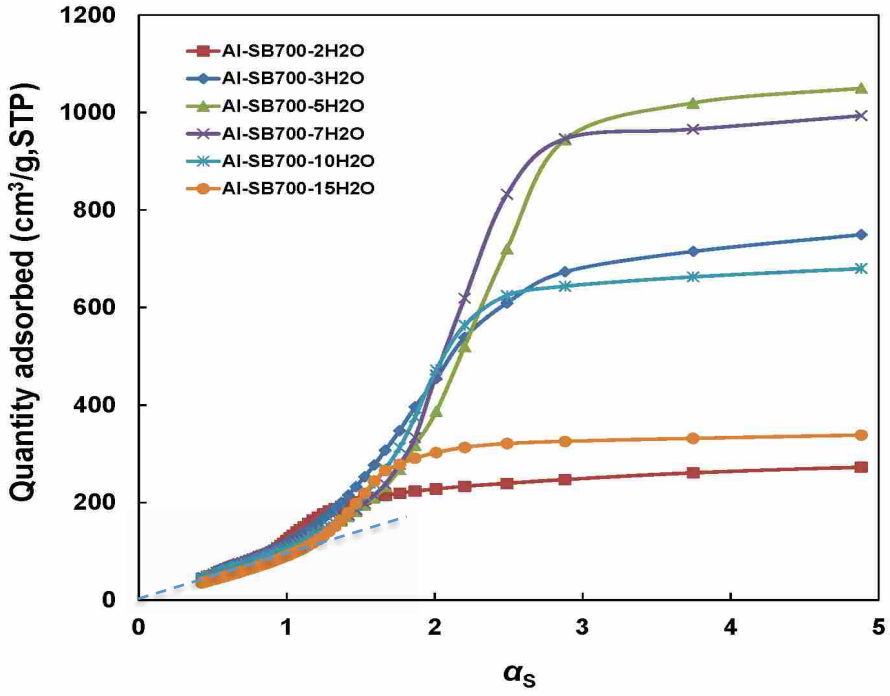

Figure 5.6 α_s plots of calcined alumina samples prepared with different H_2O/Al ratios.

H_2O/Al = 2 is approximately 0.9, indicating the presence of relatively small mesopores. With increased H_2O/Al ratios, the onset values for capillary condensation become larger, suggesting capillary condensation occurs in larger mesopores. At the high-pressure end of the plot, all the plots reach a plateau, indicating a small fraction of large mesopores (30-50 nm) or macropores (> 50 nm).

The slope of the linear part of the comparative plot also gives information about the mesoporous area and pore volume of calcined alumina samples. As listed in Table 5.1, the total surface area S_{tot} and BET surface area S_{BET} are in excellent agreement, which further confirms the absence of detectable micropores in all studied samples. Moreover, the mesopore volume and single-point pore volume are in very good agreements, confirming the validity of the CA analysis.

5.3.5 Thermal analysis

Figure 5.7 shows the TGA-DTA profiles for as prepared alumina precursors. Their mass losses in different temperature ranges are listed in Table 5.2. For all as-prepared precursors, a major mass loss between 25 and 100 °C is observed, which can be assigned to the evaporation of *sec*-butanol and physically adsorbed water, as indicated by the first endothermic peak in the DTA curve. The subsequent weight loss between 100 and 300 °C is attribute to the removal of interlayer or surface water molecules during the dehydration in boehmite to γ-alumina transition, as suggested by the second endothermic peak around 270 °C. The final weight loss from 300 to 700 °C is due to the removal of surface hydroxyl group of γ-alumina consistent with previous work.[13]

Table 5.2 TG weight loss (%) of as made precursors in different temperature ranges

Sample	ΔW1 (20-100 °C)	ΔW2 (100-300 °C)	ΔW3 (300-700 °C)
Al-SB700-2H_2O	55.82	12.57	1.31
Al-SB700-5H_2O	62.30	7.91	1.04
Al-SB700-10H_2O	76.78	3.58	1.30
Al-SB700-15H_2O	78.92	2.16	1.19

5.4 Discussion

The controlled, solvent-deficient hydrolysis of alkoxides discussed in an earlier paper[1] and used in this study as a function of H_2O/Al molar ratio has been demonstrated to be a facile, template-free route for the preparation of MAs of high surface area, large pore volume, and tunable pore size in the range of 4-18 nm. While aluminas of similar properties have been

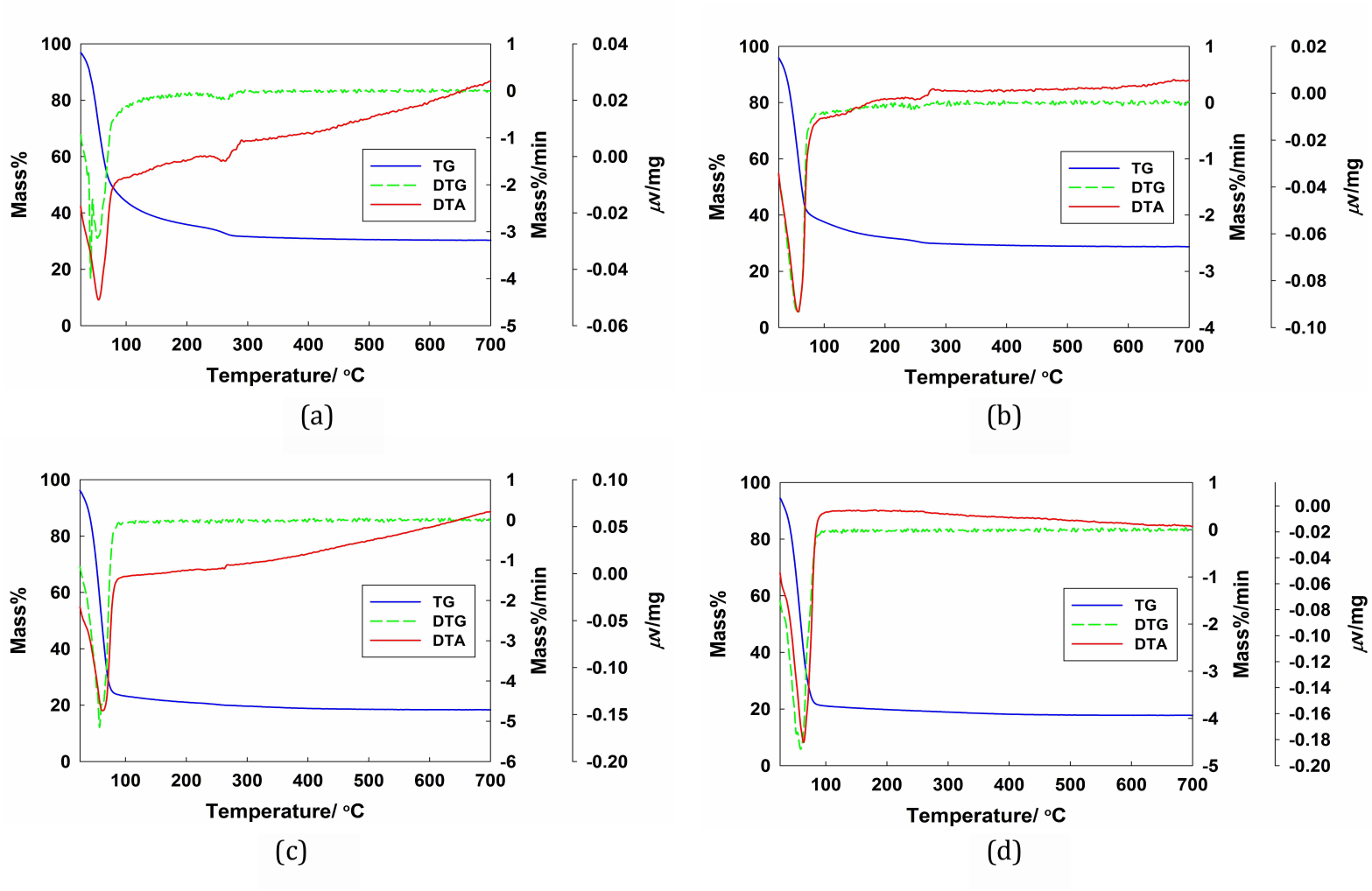

Figure 5.7. TGA-DTA curve for as made boehmite precursors prepared with different H_2O/Al ratios: (a) H_2O/Al = 2; (b) H_2O/Al = 5; (c) H_2O/Al = 10; (d) H_2O/Al = 15.

previously reported, their preparation required use of SDAs. [14-16] The results of this study provide new insights into the chemistry of formation of porous aluminas from hydrolysis of aluminum alkoxides and the effects of H_2O/Al ratio on pore structure of high surface area MAs.

5.4.1 Effects of H_2O/Al ratios on precursor morphology

It has been reported that the morphology of the primary crystallites and aggregates of boehmite strongly depends on the pH,[17-19] since acidity and ionic strength govern the protonation-deprotonation of the surface oxygen atoms and thus determine the electrostatic surface charge density. However, since the synthesis method in the present study involves only water and alcohols, all pH values measured in the preparation of the 6 samples are approximately 7. In addition, given that no external SDA is used, we postulate that the relative concentrations of water and alcohol from the hydrolysis reaction is the key factor controlling morphology of the boehmite precursors and, as will be shown later, that of the calcined γ-alumina samples.

When a solution of aluminum alkoxide in alcohol, benzene or other organic solvent is mixed with water, one of two hydrolysis reactions may occur depending upon the H_2O/Al ratio:

$$Al(OR)_3 + 2H_2O = AlOOH \text{ (boehmite)} + 3ROH \qquad (5.1)$$

$$Al(OR)_3 + 3H_2O = Al(OH)_3 \text{ (bayerite)} + 3ROH \qquad (5.2)$$

The results of this work show that at H_2O/Al ratios below 10, aluminum oxy-hydroxide (boehmite) formed via Reaction 1 is the only product. At higher H_2O/Al ratios, the aluminum hydroxide (bayerite) phase is observed to form by Reaction 2 to a small extent (See Figure 5.1). This chemistry is consistent with that reported in previous literature.[20, 21]

It is well known that in a dilute, acidic solution of aluminum salts, the prevailing ionic species is $[Al(H_2O)_6]^{3+}$. Due to possible polarization of the water molecules by the Al ion,[22] deprotonation can occur as follows:

$$Al(H_2O)_6^{3+} \rightleftarrows 2Al(OH)(H_2O)_5^{2+} + H^+ \qquad (5.3)$$

And the resultant complex will dimerize by condensation

$$2Al(OH)(H_2O)_5^{2+} \rightleftarrows Al(OH)_2(H_2O)_8^{4+} + 2H_2O \qquad (5.4)$$

As illustrated in Figure 5.8, further condensation/polymerization can proceed in one of two ways: (1) forming chains by linking octahedra through common edges or (2) forming hexagonal rings which further coalesce to large polynuclear complexes, depending on the chemical environment and temperature. According to Baker et al.,[23] "fast" polymerization resulting from high concentration of the hydroxyl intermediate leads to chain-like agglomeration whereas "slow" polymerization due to low hydroxide concentration or aging results in sheet-like aggregation.

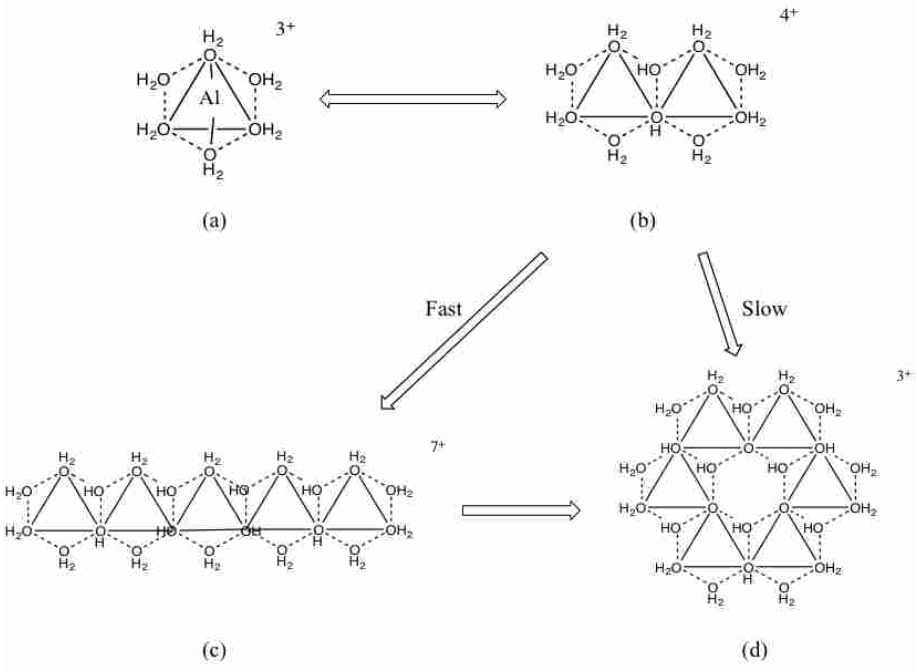

Figure 5.8 Polymerization of boehmite crystallite. (a) $Al(H_2O)_6^{3+}$, (b) $2Al(OH)(H_2O)_5^{2+}$, (c) chain-like boehmite polynuclear complex (d) plate-like boehmite polynuclear complex

In the present study, the different morphologies of the precursor prepared with varied water to aluminum ratio can be explained by the difference in the hydrolysis and polymerization rate induced by the different water contents. When the water content is low (H_2O/Al = 2), the hydrolysis and polymerization proceed relatively slow and therefore small plate-like crystallites are observed by TEM. Formation of small particles is likely a consequence of inhibited crystallization due to hydrogen bonding between alcohols produced during hydrolysis and the positively charged polynuclear complex. This inhibition was observed in previous studies[21, 24] and is consistent with our observation of a largely amorphous XRD pattern. Due to the solvent deficient environment, its low viscosity, the presence of unreacted alkoxide, cross-linking or end-to-end connection of platelets via residual alkoxide groups is favored.[25] In the cross-linked structure consisting of small boehmite platelets, small, irregular pores are observed (Figure. 5.3a); this morphology is sometimes referred to as "wormhole" boehmite. Following calcination and decomposition of the alkoxide groups these small platelets stack closely on and next to each other (Figure 5.4a).

With a small increase of water content from H_2O/Al of 2 to 5, since alcohol molecules are diluted by the excess water, there is less inhibition and polymerization of boehmite proceeds more rapidly, producing larger boehmite plates as observed by TEM (Figure 5.3b). According to the DFT study by Raybaud et al.,[26] the slab-like structure and distribution of different surface planes in boehmite is largely due to surface energy forces. Thus, in the agglomeration of primary boehmite crystallites, bonds are most likely to occur between surface planes of highest energy. The surface energy of the (010) basal plane in boehmite is the lowest of relevant surface planes as shown in Figure 5.9, whereas the (101) faceted plane has the highest surface energy. Thus the high-energy (101) plane adsorbs solvent molecules or bonds to other high-energy surfaces to

reduce its surface energy. As a consequence of its low surface energy and the preferential bonding of the faceted planes, the total surface area of the basal (010) plane is preferentially expanded. This is confirmed by the increased intensity of the (020) reflection centered at 2θ = 15° (Figure 5.1a) because the (010) boehmite surface has the lowest surface energy and tends to expand. In addition, the enriched water/alcohol environment enhances the mobility of the aggregates. During the early stage of the calcination, the evaporation of alcohol and loosely physical adsorbed water molecules induces the disordered 3-D stacking (Figure 5.3b), similar to the materials obtained via an evaporation-induced self-assembly mechanism.[27, 28]

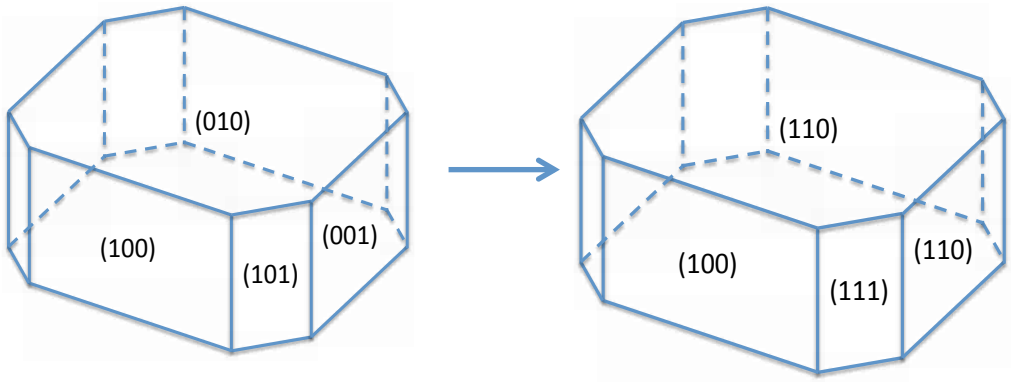

Figure 5.9 Schematic representation of a (a) boehmite nanoparticle exhibiting usual experimentally observed crystalline surfaces and (b) resulting γ-alumina

With further increased water content (H_2O/Al = 15), the hydrolysis and the polymerization proceed relatively rapidly, therefore long fibrillar boehmite is observed (Figure 5.3c), as well as a small fraction of thin sheet-like bayerite (via Reaction 5.2 due to excess of water). The observation by TEM of a boehmite-bayerite mixture is consistent with the XRD results.

Comparison of the TEM micrographs between precursors (Figure 5.3) and their corresponding calcined alumina samples (Figure 5.4) shows that the morphology of the former is preserved after calcination, consistent with the general conclusion that the transformation from boehmite to γ-alumina is topotactic.[13, 21, 26, 29] For the calcined alumina sample prepared at H_2O/Al =2 (Figure 5.4a), aggregates consisting of platelets with a particle size of *ca.* 5-7 nm are observed, consistent with the particle size determined by the XRD results and those of a previous study.[30] The morphology of the calcined sample is very similar to that of its precursor, although the edge of calcined sample is more clearly defined (comparing Figures 5.3a and 5.4a) due to better crystallinity after calcination. When the H_2O/Al ratio is increased to 5, both the precursor and the calcined sample exhibit almost the same morphology (Figures 5.3b and 5.4c). The basal planes, each with a length of *ca.* 30 nm and a width of *ca.* 20 nm are evident, which correspond to the (110) plane of γ-alumina apparently the same as the (010) basal plane of boehmite precursor, each structure having its own indexing[29, 31] as illustrated in Figure 5.9. What appear to be dark "fibers" with a thickness of 5-8 nm are actually (100) or (111) lateral edges of γ-alumina that are converted from (100) and (101) planes of the boehmite precursor, respectively.[17] This observation is similar to that for alumina prepared by introducing large molecular weight polymer molecules.[16, 32, 33] At a large H_2O/Al ratios (*e.g.* H_2O/Al = 15) the precursor is a composite of fiber-like boehmite and sheet like bayerite at lower magnification (Figure 5.3c). However, after calcination, closely packed platelets are observed in the TEM micrographs for the corresponding samples (Figure 5.4f). This transformation is due to the removal of interlayer or surface water during early calcination and of hydroxyl groups at elevated temperatures.

Thermal analysis also provides insights into the formation of boehmite with different morphologies. It is interesting that the intensity of the second peak in the DTA curve, as well as

the corresponding weight loss at intermediate temperatures due to the removal of the relatively strongly bonded interlayer or surface water, decreases with increased water content during hydrolysis. This behavior may be due to lower water content at the terminus of chains or on the surfaces of highly polymerized boehmite crystallites consistent with the observation by Baker et al.[23] The TGA results are consistent with the increased crystallite size observed in the TEM images of boehmite precursors prepared with increasing H_2O/Al ratios (Figure 5.3).

It is worth noting that the sample prepared with H_2O/Al = 5 showed the lowest weight loss at high temperatures (Table 5.2), which is explained by the low contact area resulted from its 3-D stacking morphology; low contact area is associated with the high thermal stability in previously reported studies.[1, 16]

5.4.2 Effects of H_2O/Al ratios on alumina pore structure.

Given the different morphologies of calcined γ-alumina samples, it follows that different pore structures are to be expected. The results of this work show that is indeed the case. As shown in the N_2 adsorption results (Figure 5.5 and Table 5.1), significant changes in pore volume and pore size distribution are induced by variations in H_2O/Al ratio during preparation. For calcined samples prepared with low water content, (H_2O/Al = 2 and 3), the small pore volume and average pore width are consistent with their corresponding small particle size and close-packed morphology (Figures 5.4a and 5.4b). As particles size increases with increasing H_2O/Al ratio (H_2O/Al = 5 and 7), small pores resulting from the spaces between the closely packed crystallites are replaced by larger voids created by the random stacking of nano-plates (Figures 5.4c and 5.4d), leading to larger pore volume and larger average pore width. The shift in the pore size distribution to larger size with increasing H_2O/Al ratio (Figure 5.5b) further confirms this observation. However with further increased water content (H_2O/Al ratio > 10) pore volume and

average pore width of the corresponding calcined samples decrease as a result of decreasing crystallite size and tighter agglomeration (Figures 5.4e and 5.4f).

As shown in the α_s plot (Figure 5.6), for all samples the low-pressure part of these plots exhibits excellent linearity starting from the lowest adsorption uptakes, and can be back extrapolated to the origin, indicating the absence of detectable micropores. This observation is largely consistent with the very small fractions in the micropore range observed in the PSD plot (Figure 5.5b). In addition, the span between the two linear regions at both low- and high-pressure ends of the α_s plots also provides information about the pore size distribution. For samples prepared with H_2O/Al = 2, the span is approximately from 0.9 to 1.4, whereas the corresponding range for samples prepared with H_2O/Al = 3 is from approximately 1.0 to 3.0. As a result, the width of the pore size distribution of the latter is broader, *i.e.*, 1.3 vs 1.4, respectively (Table 5.1 and Figure 5.5b). Similarly, above the limit of H_2O/Al = 5, spans between the two linear regions in α_s plots of samples prepared with higher H_2O/Al ratios become narrower, confirming narrower pore size distributions obtained from N_2 adsorption. In addition, it is worth noting that the external surface areas of samples with pore widths above 10 nm are relatively large (> 50 m^2/g), this is explained by their relatively large crystallite size and their stacking patterns observed in the TEM. In principle, large, randomly stacked alumina nanoplates tend to create larger voids and therefore are more likely to possess surface outside the pores, whereas closely packed aggregates of small alumina crystallite tend to produce small pores and therefore possess a higher of fraction of mesoporous surface relative to external surface.

5.5 Conclusion

In summary, we have successfully synthesized MA catalysts supports with controlled pore properties by varying the H_2O/Al molar ratios in the hydrolysis of aluminum alkoxides.

This time- and cost-effective approach not only contributes to the development of MA, but also offers an opportunity to control the pore structure and morphology without addition of structure directing agents.

The results in this study provide some insights into the mechanism of the nanostructure formation as follows:

(1) The compositions of water used in the hydrolysis and the resultant alcohol are keys to controlling morphologies of the boehmite precursor and corresponding calcined γ-alumina. The former determines the rate of the hydrolysis while the latter adsorbs to surface planes of the boehmite crystallite to reduce surface energies and inhibit the polymerization of the primary crystallites.

(2) The formation of the 3-D scaffolding structure is likely due to the evaporation induced self-assembly (ELSA) during the early stage of a controlled thermal treatment involving drying and calcination in air.

In terms of applications, alumina catalyst supports synthesized by this simple, new method have relatively high surface area (240~320 m^2/g), large pore volume (up to 1.6 cm^3/g) and tunable pore size (4-18 nm). Thus, these easily prepared materials with improved properties offer promise for improvements in a numbers of applications, including automobile emission control, Fischer–Tropsch synthesis and oil-refining industry.

References

1. Huang, B.; Bartholomew, C. H.; Smith, S. J.; Woodfield, B., Facile solvent-deficient synthesis of mesoporous gamma alumina with controlled pore structures. *Micropor. Mesopor. Mater.* **2013,** *165*, 70-78.
2. Smith, J. S.; Liu, S.; Liu, Q.; Olsen, R. E.; Rytting, M.; Selck, D.; Simmons, C.; Boerio-Goates, J.; Woodfield, B. F., Metal oxide nanoparticle synthesis via a robust "solvent-deficient" method. *Chem. Mater.* **2012**. Submitted.

3. Bartholomew, C. H.; Woodfield, B. F.; Huang, B.; Olsen, R. E.; Astle, L. Method for making highly porous, stable metal oxide with a controlled pore structure. 2011-US29472, 2011119638, 20110322., 2011.

4. Woodfield, B. F.; Liu, S.; Boerio-Goates, J.; Liu, Q. Preparation of uniform nanoparticles of ultra-high purity metal oxides, mixed metal oxides, metals, and metal alloys. 2007-US4279, 2007098111, 20070216., 2007.

5. Gregg, S. J.; Sing, K. S. W., *Adsorption, surface area and porosity*. 2 ed.; Academic Press: London, 1982.

6. Rouquerol, F.; Rouquerol, J.; Sing, K., *Adsorption by powders and porous solids*. Academic Press: London, 1999.

7. Huang, B.; Bartholomew, C. H.; Woodfield, B. F., Improved calculations of pore size distribution for relatively large, less-ordered slit-shaped mesopore structure. *Micropor. Mesopor. Mater.* **2013**.

8. Sayari, A.; Liu, P.; Kruk, M.; Jaroniec, M., Characterization of large-pore MCM-41 molecular sieves obtained via hydrothermal restructuring. *Chem. Mater.* **1997,** *9* (11), 2499-2506.

9. Sing, K. S. W., *Surface area determination*. Butterworths: London, 1970.

10. Cejka, J.; Zilkova, N.; Rathousky, J.; Zukal, A., Nitrogen adsorption study of organized mesoporous alumina. *Phys. Chem. Chem. Phys.* **2001,** *3* (22), 5076-5081.

11. Cejka, J.; Zilkova, N.; Rathousky, J.; Zukal, A.; Jagiello, J., High-resolution adsorption of nitrogen on mesoporous alumina. *Langmuir* **2004,** *20* (18), 7532-9.

12. Rouquerol, J.; Avnir, D.; Fairbridge, C. W.; Everett, D. H.; Haynes, J. H.; Pernicone, N.; Ramsay, J. D. F.; Sing, K. S. W.; Unger, K. K., Recommendations for the characterization of porous solids. *Pure Appl. Chem.* **1994,** *66* (8), 1739-58.

13. Tsukada, T.; Segawa, H.; Yasumori, A.; Okada, K., Crystallinity of boehmite and its effect on the phase transition temperature of alumina. *J. Mater. Chem.* **1999,** *9* (2), 549-553.

14. Zhang, Z.; Pinnavaia, T. J., Mesostructured γ-Al_2O_3 with a lathlike framework morphology. *J. Am. Chem. Soc.* **2002,** *124* (41), 12294-12301.

15. Zhang, Z.; Pinnavaia, T. J., Mesoporous γ-alumina formed through the surfactant-mediated scaffolding of peptized pseudoboehmite nanoparticles. *Langmuir* **2010,** *26* (12), 10063-10067.

16. Zhu, H. Y.; Riches, J. D.; Barry, J. C., Gamma-alumina nanofibers prepared from aluminum hydrate with poly(ethylene oxide) surfactant. *Chem. Mater.* **2002,** *14* (5), 2086-2093.

17. Jolivet, J.-P.; Cassaignon, S.; Chaneac, C.; Chiche, D.; Tronc, E., Design of oxide nanoparticles by aqueous chemistry. *J. Sol-Gel Sci. Technol.* **2008,** *46* (3), 299-305.

18. Jolivet, J.-P.; Froidefond, C.; Pottier, A.; Chaneac, C.; Cassaignon, S.; Tronc, E.; Euzen, P., Size tailoring of oxide nanoparticles by precipitation in aqueous medium. A semi-quantitative modelling. *J. Mater. Chem.* **2004,** *14* (21), 3281-3288.

19. Zhu, H. Y.; Gao, X. P.; Song, D. Y.; Ringer, S. P.; Xi, Y. X.; Frost, R. L., Manipulating the size and morphology of aluminum hydrous oxide nanoparticles by soft-chemistry approaches. *Micropor. Mesopor. Mater.* **2005,** *85* (3), 226-233.

20. Oberlander, R., Aluminas for catalysts-their preparation and properties. *Applied Industrial Catalysis* **1984,** *3*, 63-112.

21. Wefers, K.; Misra, C., Alcoa technical paper no.19. **1987**.

22. Hem, J. D.; Roberson, C. E.; Lind, C. J.; Polzer, W. L. *Chemical interactions of aluminum with aqueous silica at 25.Deg*; United States Geol. Surv., Washington, DC, USA.: 1973; p 57 pp.

23. Baker, B. R.; Pearson, R. M., Water content of pseudoboehmite. New model for its structure. *J. Catal.* **1974,** *33* (2), 265-78.

24. van Bronswijk, W.; Watling, H. R.; Yu, Z., A study of the adsorption of acyclic polyols on hydrated alumina. *Colloids Surf., A* **1999,** *157* (1-3), 85-94.

25. Hsu, P. H., Aluminum hydroxides and oxyhydroxides. *Soil Sci. Amer. Publ.* **1977**, 99-143.

26. Raybaud, P.; Digne, M.; Iftimie, R.; Wellens, W.; Euzen, P.; Toulhoat, H., Morphology and surface properties of boehmite (γ-AlOOH): A density functional theory study. *J. Catal.* **2001,** *201* (2), 236-246.

27. Yang, P.; Zhao, D.; Margolese, D. I.; Chmelka, B. F.; Stucky, G. D., Generalized syntheses of large-pore mesoporous metal oxides with semicrystalline frameworks. *Nature (London)* **1998,** *396* (6707), 152-155.

28. Brinker, C. J.; Lu, Y.; Sellinger, A.; Fan, H., Evaporation-induced self-assembly. Nanostructures made easy. *Adv. Mater. (Weinheim, Ger.)* **1999,** *11* (7), 579-585.

29. Chiche, D.; Chizallet, C.; Durupthy, O.; Chaneac, C.; Revel, R.; Raybaud, P.; Jolivet, J.-P., Growth of boehmite particles in the presence of xylitol: Morphology oriented by the nest effect of hydrogen bonding. *Phys. Chem. Chem. Phys.* **2009,** *11* (47), 11310-11323.

30. Alphonse, P.; Courty, M., Surface and porosity of nanocrystalline boehmite xerogels. *J. Colloid Interface Sci.* **2005,** *290* (1), 208-219.

31. Lippens, B. C.; de Boer, J. H., Study of phase transformations during calcination of aluminum hydroxides by selected area electron diffraction. *Acta Crystallogr.* **1964,** *17* (10), 1312-21.

32. Bai, P.; Wu, P.; Yan, Z.; Zhao, X. S., A reverse cation-anion double hydrolysis approach to the synthesis of mesoporous gamma-alumina with a bimodal pore size distribution. *Micropor. Mesopor. Mater.* **2009,** *118*, 288-295.

33. Bleta, R.; Alphonse, P.; Pin, L.; Gressier, M.; Menu, M.-J., An efficient route to aqueous phase synthesis of nanocrystalline γ-Al_2O_3 with high porosity: From stable boehmite colloids to large pore mesoporous alumina. *J. Colloid Interface Sci.* **2012,** *367* (1), 120-128.

Chapter 6

Facile structure-controlled synthesis of mesoporous γ-alumina: effects of alcohols in precursor formation and calcination

6.1 Introduction

In the previous two chapters, we reported a facile, solvent-deficient synthesis of mesoporous alumina without external SDAs, surfactants or templates.[1, 2] High surface area aluminas having 4-18 nm pore widths were obtained by varying the aluminum source or the water content in the hydrolysis of aluminum alkoxides. In this chapter, we have adapted this method to the synthesis of mesoporous γ-alumina, in which aluminum oxyhydroxide and/or aluminum hydroxide precursors from a controlled hydrolysis of aluminum isopropoxide are rinsed and gelled with low molecular weight monohydric alcohols. Following gelation and calcination of the precursors, mesoporous γ-aluminas with high surface areas and large pore volumes are obtained. Pore width can be tuned from 4 to 37 nm by changing the alcohol type during the gelation. The relatively simple preparation of these unique support materials has the potential of lowering catalyst cost and improving catalyst performance for many different catalytic applications. In addition, this chapter also contributes to a basic understanding of solvent/nanoparticle interactions and how they influence textural characteristics of mesoporous materials. This fundamental knowledge could be exploited in the design of tailored support materials.

6.2 Experimental Section

6.2.1 Materials

Aluminum *iso*-propoxide ($Al(OCH(CH_3)CH_3)_3$), ethanol, *iso*-propanol, *sec*-butanol, and *n*-hexanol were purchased from Alfa Aesar and used as received. Aluminumoxid C Degussa (denote as DC) was purchased from Sigma-Aldrich and used as reference materials for a comparative adsorption study.

6.2.2 Support Synthesis

A typical synthesis involves formation of precursors followed by thermal treatment.[1-3] Aluminum *iso*-propxoide was hydrolyzed at a water to aluminum molar ratio of 5 to 1 while grinding in a mortar and pestle; the resulting intermediate was rinsed with different low molecular weight alcohols (i.e. ethanol, *iso*-propanol, *sec*-butanol and *n*-hexanol, respectively) in a medium mesh filter under house vacuum. After 16 hours of aging, the obtained precursors were subsequently thermally treated in a muffle furnace in air at 700 °C for 2 hours. For example, 20.031 g of aluminum *iso*-propoxide was mixed with 8.83 ml of distilled water (H_2O : Al = 5:1) using a mortar and pestle for 20 minutes. The resulting white intermediate was placed in a filter and rinsed with 200 ml of ethanol under house vacuum with vigorous stirring. After 20 minutes, a two-phase system is observed: a gel-like mixture was formed in the bottom of filter and a layer of lighter alcohols was formed in the top. This mixture was left to age for 16 hours. The obtained precursor was then calcined in a muffle furnace in air at 700 °C for 2 hours. A ramp rate of 2.33 °C/min was used to (1) avoid rapid dehydration to ensure uniform pore construction and (2) ensure uniform heat transfer to achieve better homogeneity and avoid rapid grain growth.

The final samples were labeled, starting with a prefix of Al followed by the type of alcohol used. For example, Al-EtOH refers to an alumina sample prepared from aluminum *iso*-

propoxide treated with ethanol and calcined at 700°C for 2 hours in air. All the precursors before calcination are denoted with a suffix "pre", e.g., Al-Iprop-pre refers to the precursor treated with *iso*-propanol before calcination.

6.2.3 Characterization

The structure of each sample was determined by powder X-ray diffraction (XRD) on a Panalytical X'Pert Pro X-ray diffractometer with Cu Kα radiation (λ=0.15418 nm) at a scanning rate of 0.02 °s^{-1} in the 2θ ranges from 10° to 80°. A fixed power source was used (40 kV, 40 mA). All alumina precursors were dried at room temperature over night before the measurements. Crystallite sizes were estimated using the Scherrer formula for size-related peak broadening.

The morphology of the samples was observed with a FEI Philips Technai F30 transmission electron microscope (TEM) operating at 300 kV or a FEI Philips Technai F20 Analytical STEM operating at 200 kV. Specimens were prepared by dispersing samples in ethanol, sonicating in a water bath for 1 hour and then placing a drop of the diluted solution on a carbon film supported by a 200 mesh Cu grid (Ted-Pella Inc.). A rough particle size distribution is obtained by measuring the length and width of 150 primary particles. The average particle size are calculated by the equation[4]:

$$D_{average} = \frac{\sum n_i (D_{measured,i})^3}{\sum n_i (D_{measured,i})^2} \qquad (6.1)$$

Nitrogen adsorption analysis was carried out using a Micromeritics Tristar 3020 apparatus at -196 °C. Samples were degassed at 200 °C with nitrogen flow over night prior to the measurements. Specific surface area (SA) was calculated by the Brunauer-Emmett-Teller (BET) method, using a P/P_0 range between 0.05 and 0.2.[5] Pore volume (PV) was calculated from the

adsorption isotherm at the relative pressure of 0.99 and mean Pore size distribution (MPD) were determined using a newly developed method involving slit pore geometry (SPG) for the Kelvin equation and structural corrections for area and volume, while fitting the data to a log normal distribution function.[6] The adsorption branch was used for samples with a pore width lower than 10 nm, whereas the desorption branch was used for those with a pore width above 10 nm.

Comparative adsorption analysis, the α_s method, is also employed to obtain the total surface area, external surface area, and mesopore volume.[7] Since the aluminas in the present study are calcined at 700 °C, Degussa Aluminumoxid C has been found suitable for the analysis of isotherms on porous γ-alumina because of its similar surface chemistry.[8-10]

Thermogravimetric and differential-temperature analyses (TG/DTA) were performed using a Netzsch STA 409PC instrument. For these experiments, roughly 30 mg of uncalcined precursor material was loaded onto a platinum pan and heated from room temperature to 700 °C under a 20 mL/min Helium gas flow with a temperature ramp of 3 °C/min.

6.3 Results and discussion

6.3.1 Preparation and characterization of boehmite/bayerite precursor and γ-alumina phases

XRD patterns of as synthesized precursors and calcined alumina samples are shown in Figure 6.1. For as prepared precursors (Figure 6.1a), characteristic peaks of boehmite (JCPDS card 04-013-2972) are observed except for the one rinsed with *n*-hexanol. The four main peaks of boehmite are indexed to the (1 2 0), (1 4 0), (0 5 1), (2 5 1) reflections. For the precursor treated with *n*-hexanol, peaks of bayerite (JCPDS card 00-001-0287) are observed. After calcination at 700 °C for 2 hours, all precursors are transformed into γ-alumina. Characteristic peaks of γ-alumina (JCPDS card 00-029-0063) are observed (Figure 6.1b). However, the

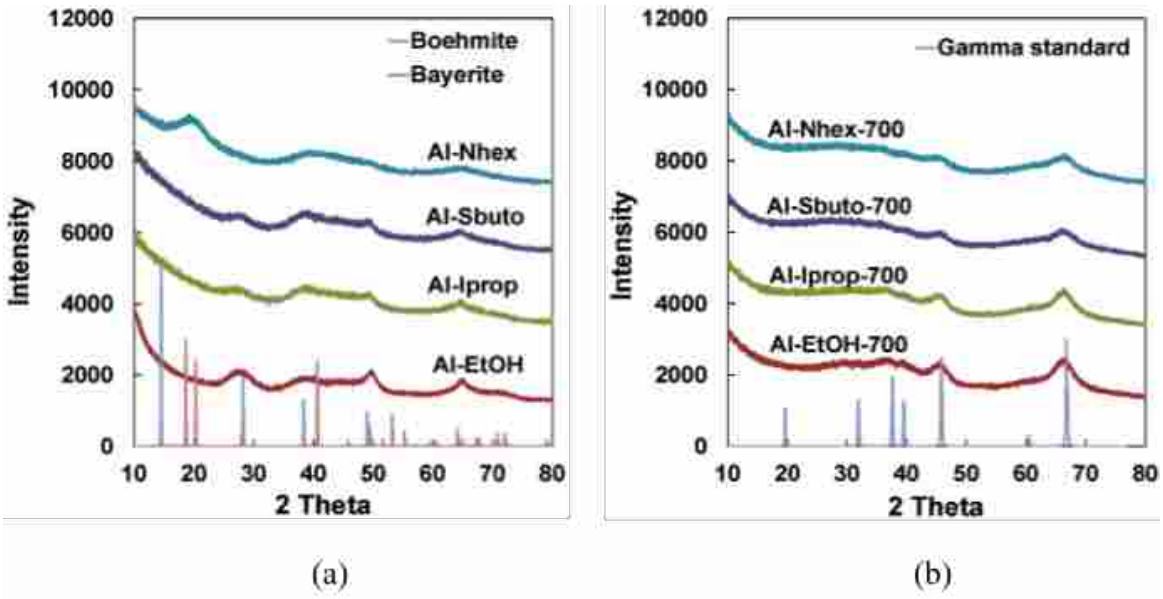

Figure 6.1 X-ray Diffraction patterns of (a) as synthesized precursors and (b) calcined alumina samples.

observed peaks are very broad, which can be attributed to a disordered arrangement of very small crystallites making up the pores. Indeed, the calculated average particle sizes for the platelet thickness based on the Scherrer formula are approximately 4-6 nm for the precursors and 3-5 nm for the calcined γ-alumina samples (Table 6.1). Both precursor and calcined particles in the present study are smaller than the those of aluminas prepared from a controlled, solvent-deficient hydrolysis of aluminum alkoxides in our previous study,[2] in which stoichiometric amount of alcohol produced during the hydrolysis reaction was reported to inhibit the polymerization of primary boehmite precursors via hydrogen bonding with boehmite surface. Since in the present study, primary boehmite crystallites are rinsed and gelled with a large excess of alcohol, a more significant inhibition effect is expected and observed. Therefore, the decreased particle size observed in this study can be explained by the alcohol-rich environment during rinsing and gelation, consistent with the general conclusion from earlier studies [11-14] that alcohol molecules act as crystallization inhibitors as described in Section 6.3.3.

Table 6.1 TG weight loss (%) during calcination of precursors

Sample	ΔW_{total} [a]	ΔW_{theo} [b]	$\Delta W_{alcohol}$ [d]
Al-EtOH-pre	41.5	15.0 [b]	26.5
Al-Iprop-pre	38.9	15.0 [b]	23.9
Al-Sbuto-pre	38.3	15.0 [b]	23.3
Al-Nhex-pre	50.7	34.6 [c]	16.1

a. Experimental total weight loss at 700 °C
b. Theoretical value of weight loss according to dehydration of boehmite: $2AlOOH(s) = Al_2O_3(s) + H_2O(g)$
c. Theoretical value of weight loss according to dehydration of bayerite $2Al(OH)_3 = Al_2O_3(s) + 3H_2O(g)$
d. Weight loss due to the removal of alcohol calculated by subtracting stoichiometric weight loss of water from experimental total weight loss at 700 °C

TGA–DTA profiles for alumina precursors provide insights into the phase transition from boehmite or bayerite to gamma-alumina. Figure 6.2 shows the TGA-DTA profiles for as prepared alumina precursors. For precursors rinsed and gelled with ethanol, *iso*-propanol and *sec*-butanol, a major weight loss peak occurs during the subsequent calcination due to the evaporation of alcohols and physically adsorbed water in the temperature range from 25 °C to *ca.* 150 °C. That this weight loss is due to evaporation of weakly held alcohol and water molecules is confirmed by the endothermic peak in the DTA curve in the same temperature range. The subsequent gradual weight loss and linearly increasing DTA signal from 150 °C to 350 °C can be attribute to the removal of chemically adsorbed water and alcohol molecules. This trend in a gradual weight loss at higher temperatures is consistent with observed behaviors of boehmite precursors during thermal treatments in previous studies.[15, 16] For the Al-Nhex sample of this study, an additional weight loss peak is observed from 200 to 350 °C, which can be assigned to

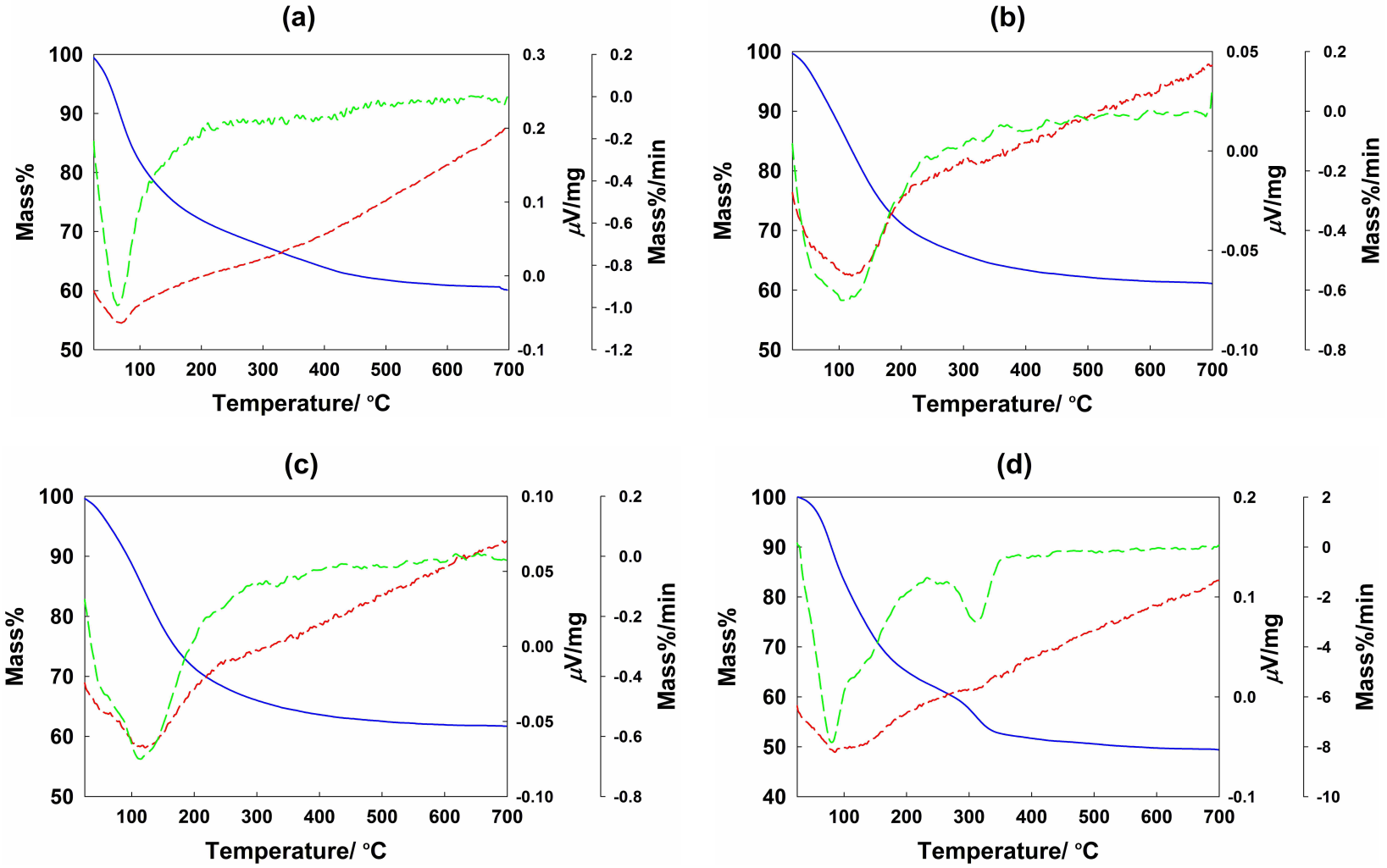

Figure 6.2. TGA-DTA curve for as made precursors rinsed and gelled with different alcohols: (a) Al-EtOH; (b) Al-Iprop; (c) Al-Sbuto; (d) Al-Nhex. (Blue: TGA curve; Green: DTG curve; Red: DTA curve)

the dehydration from bayerite to boehmite,[17] consistent with the XRD observation of bayerite in the corresponding precursor (Figure 6.1a).

It should be emphasized that the total weight loss for all four samples (Table 6.1) are much larger than theoretical values for the corresponding dehydration reactions, indicating that significant amounts of alcohol molecules are physically and/or chemically adsorbed on the surface of the precusors and subsequently desorbed at high temperatures. It should also be noted that the calculated amount of adsorbed alcohols decreases with increasing carbon chain length, which can be explained by the tendency toward decreasing hydrogen bonding of larger alcohols.

Table 6.2 Structural parameters of different g-Al_2O_3 samples calcined at 700 °C in air for 2 h

Sample	S_{BET} [a]	S_{tot} [b]	V_{sp} [c]	X_{SPG} [d]	σ [d]	Plate thickness (precursor) [e]	Plate thickness (alumina) [e]
	(m^2/g)	(m^2/g)	(cm^3/g)	(nm)		(nm)	(nm)
Al-EtOH	260	257	0.89	7.2	1.15	6.5	5.5
Al-Iprop	213	211	1.43	23.5	1.43	6.1	5.1
Al-Sbuto	185	183	1.18	32.7	1.77	5.7	4.1
Al-Nhex	208	207	0.85	6.1 & 37.0	1.82	3.5	2.9

a. BET surface area determined by N_2 adsorption at 77 K, calculated by BET equation using P/P_0 ranges form 0.01-0.20
b. Total surface area determined from α_s method
c. Pore volume obtained from single point method at $P/P_0 = 0.99$
d. Mean pore width and standard deviation obtained from SPG model using the desorption branch
e. Plate thickness determined using Scherrer formula from XRD results

6.3.2 Effect of alcohols on pore structures of *γ*-alumina

Figure 6.3 shows the nitrogen adsorption-desorption isotherms and pore size distributions of calcined *γ*-alumina samples. Their surface areas, pore volumes and pore size distributions are listed in Table 6.2. It is evident that by varying the alcohols used in the rinsing and gelation of boehmite/bayerite precursors from the controlled hydrolysis of aluminum alkoxides, alumina

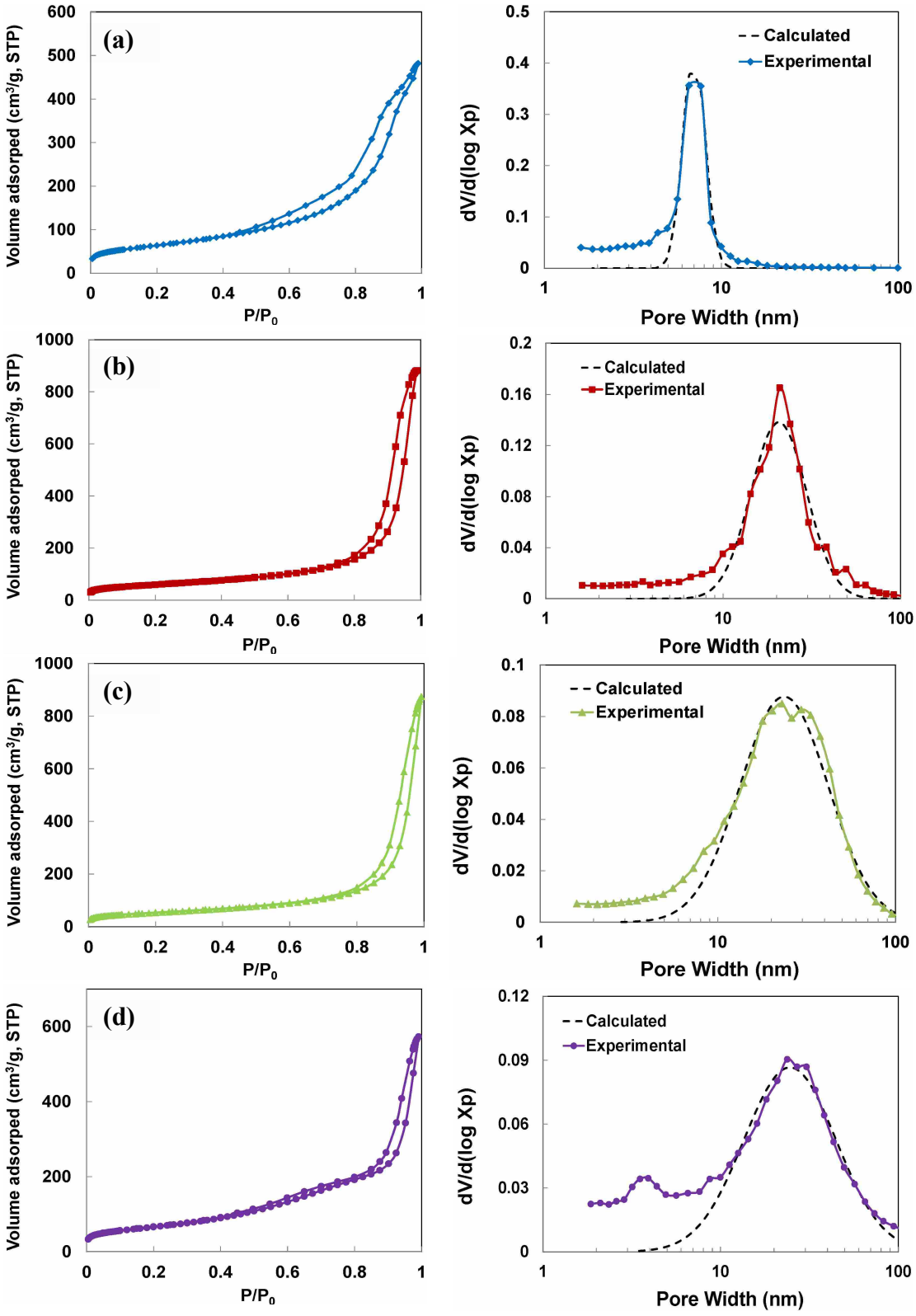

Figure 6.3 N_2 adsorption/desorption isotherms and corresponding pore size distributions of calcined alumina samples rinsed and gelled with different alcohols: (a) Al-EtOH; (b) Al-Iprop; (c) Al-Sbuto; (d) Al-Nhex.

catalyst supports with relatively high surface area (up to 260 m^2/g), large pore volume (up to 1.4 cm^3/g) and tunable pore size (7-37 nm) are prepared. It is also worth noting that average pore width increases with increasing chain length of the alcohol used in the rinsing and gelation.

For all four samples, isotherms are Type IV (IUPAC designation), confirming the presence of mesopores. For Al-EtOH (Figure 6.3a), a H3 type of hysteresis loop is observed, indicating the presence of slit-like pores. The average pore width is *ca.* 7 nm and a narrow pore size distribution is observed in the PSD plot. For Al-Iprop and Al-Sbuto (Figure 6.3b and 6.3c), hysteresis loops are apparently a composite of H1 and H3, indicating that they have slit-shape pores formed by uniformly distributed plate-like particles. It is worth noting that the N_2 uptakes for these two samples are approximately 900 cm^3/g STP, indicating very large pore volumes.[5] Accordingly, the calculated pore volumes of 1.32 and 1.52 cm^3/g for Al-Iprop and Al-Sbuto, are unusually large for γ-alumina. In addition, the hysteresis loops are shifted to higher P/P_0, indicating that capillary condensation occurs in larger mesopores. Indeed, the calculated mean pore widths are 23.5 and 32.7 nm, respectively. For Al-nHex (Figure 6.3d), the adsorption and desorption isotherms can be attribute to a mixed types of H2 and H1, occurring at middle- and near-saturation pressure stages, respectively. As a result, a bi-model pore size distribution is observed in the corresponding PSD plot and the calculated average pore widths are 6.1 and 37 nm. It should be stressed that for all four samples, pore size is much larger than the size of alcohols used in the present study, and pore size distributions are much broader than those would be anticipated for mesostructures formed through a super molecular pathway in which the pore size is determined by the size of the surfactant.[18] Indeed, pore sizes and pore size distributions of aluminas in this study are consistent with a particle assembly mechanism in which the role of the alcohol is primarily to mediate the size and intergrowth of the boehmite particles through

hydrogen bonding and interspacing, similar to the functions of amine or Brij 56 surfactants reported in previous studies.[19-22]

Comparative adsorption analysis provides further insights into the pore structures of our mesoporous aluminas. As shown in Figure 6.4, for all samples, the low-pressure part of these plots exhibits excellent linearity starting from the lowest adsorbed amounts, and can be back extrapolated to the origin, indicating the absence of detectable micropores, which is confirmed by the excellent agreement between the total surface area (S_{tot}) calculated from the slope of the linear part and BET surface area (S_{BET}) from N_2 adsorption (Table 6.2). The subsequent steep increase in nitrogen uptake for each plot is due to capillary condensation of nitrogen in mesopores. For the Al-EtOH sample, the onset of the jump is approximately 1.0, indicating the presence of relatively small mesopores. For Al-Iprop, the onset values for capillary condensation are shifted to approximately 1.2, suggesting capillary condensation occurs in larger mesopores. At higher α_s values, a plateau is observed for both Al-EtOH and Al-Iprop samples, indicating the absence of very large mesopores (30-50 nm), consistent with the BET results. For the Al-Sbuto sample, the steep increase observed in the α_s plot starts at approximately 1.5. However, the aforementioned plateau in the high α_s range is not observed in the high-pressure part of the plot, indicating that capillary condensation occurs in a wide range of large mesopores, which is consistent with the broad pore size distribution observed in the PSD plot. For the Al-Nhex sample, two increases are observed starting from approximately 0.9 and 2.5, respectively, indicating that capillary condensation occurs in two pore size ranges, which is in agreement with the PSD plot.

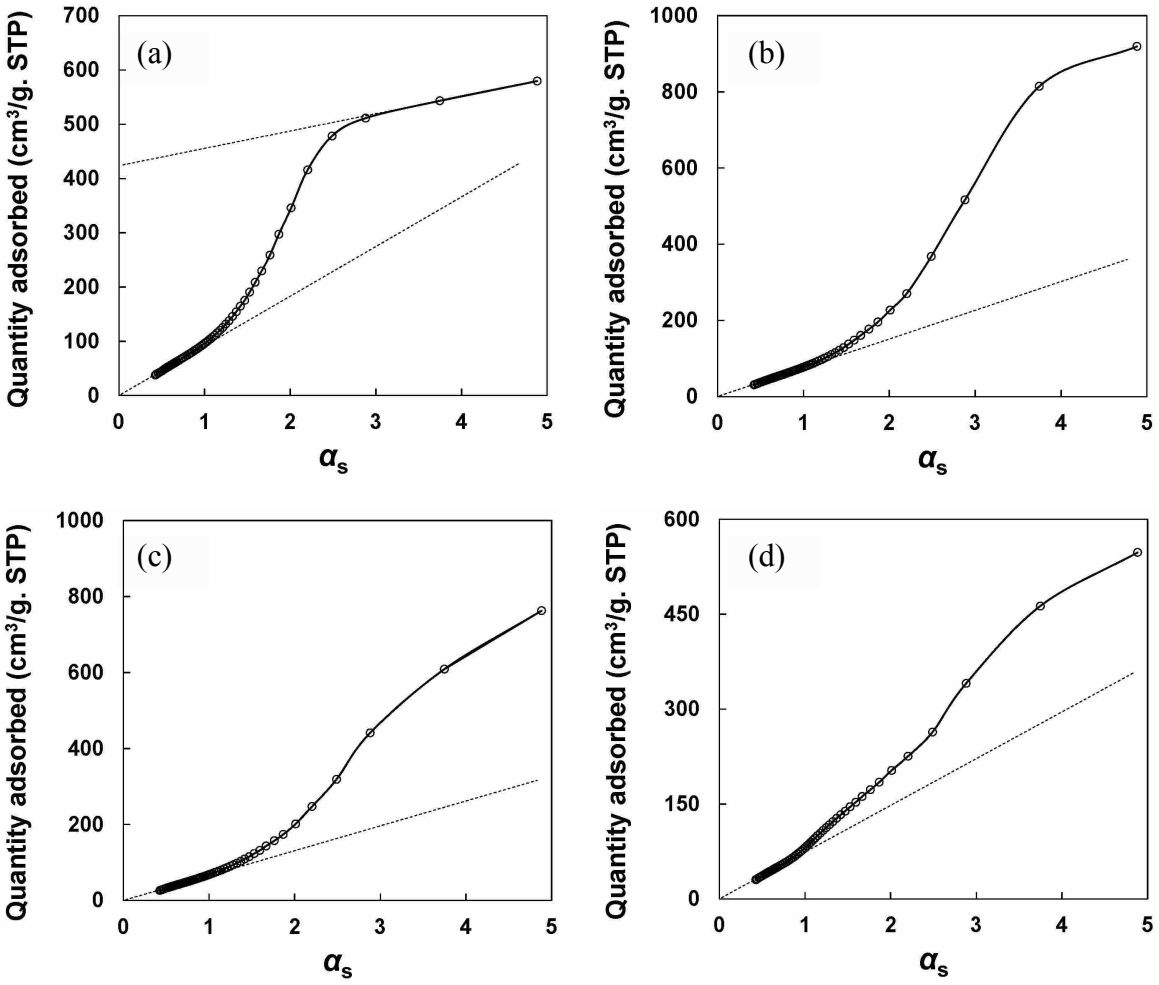

Figure 6.4. α_s plots of calcined alumina samples rinsed and gelled with different alcohols: (a) Al-EtOH; (b) Al-Iprop; (c) Al-Sbuto; (d) Al-Nhex.

6.3.3 Effects of alcohol structure on precursor and *γ*-alumina morphology.

The morphology of the precursors (pre) rinsed and gelled with different alcohols is shown in TEM micrographs (Figure 6.5). For all four precursors, plate-like primary crystallites with a length of 10-20 nm and a width of 5-15 nm are observed, consistent with the slab-like boehmite/bayerite primary crystallites reported in previous studies.[23-25] In addition, the sizes of the precursors rinsed and gelled with alcohols are smaller than those precursors without rinsing before calcination in our earlier study.[2] This reduction in precursor size is probably due to inhibition of the polymerization of primary crystallites, an effect similar to the that observed for

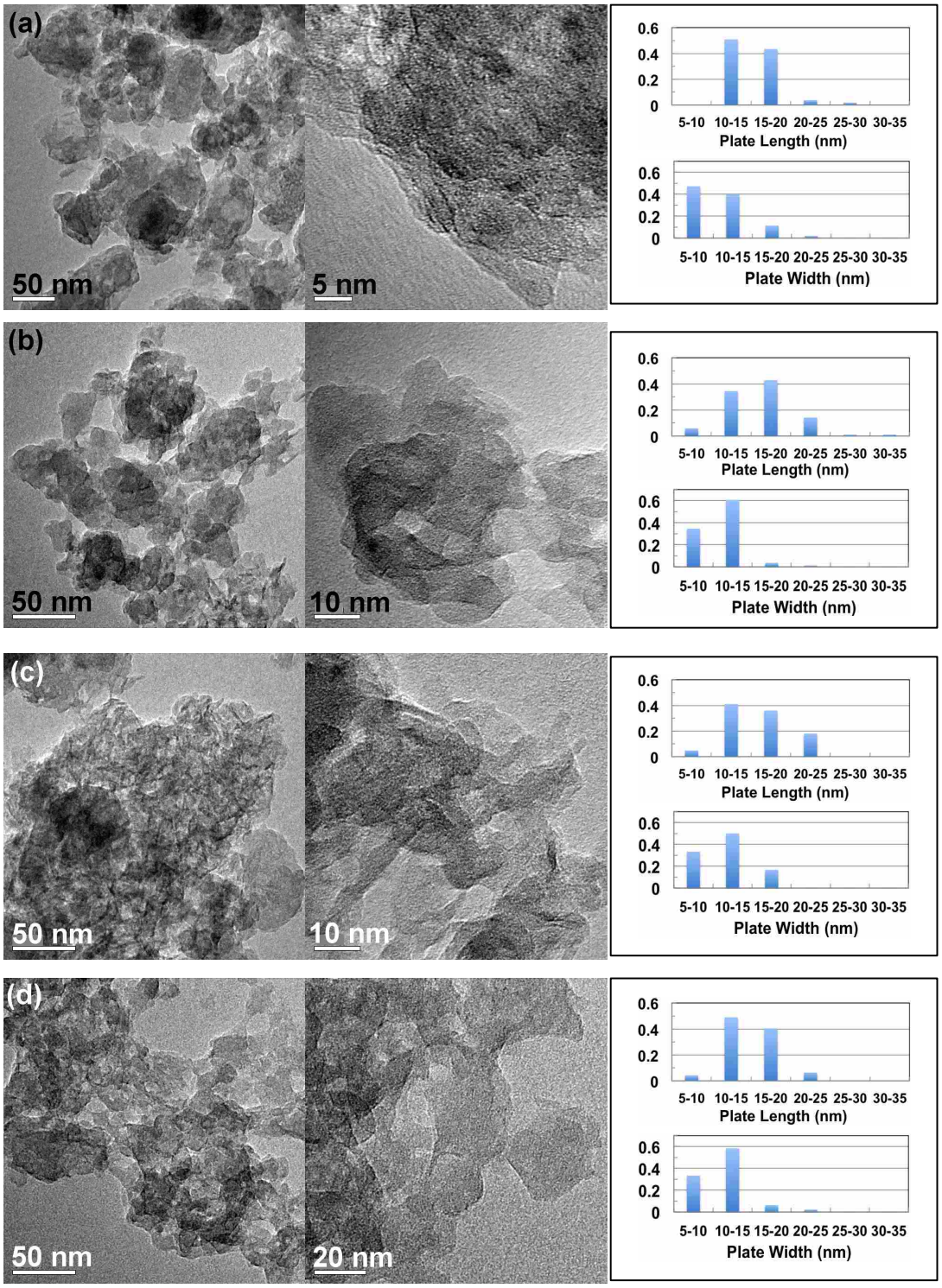

Figure 6.5 TEM images and particle size distribution of precursors rinsed and gelled with different alcohols: (a) Al-EtOH-pre; (b) Al-Iprop-pre; (c) Al-Sbuto-pre; (d) Al-Nhex-pre.

incorporation of polyols[26] and amine surfactants[19] in the preparation of nano-size aluminas. For Al-EtOH-pre rinsed and gelled with ethanol (Figure 6.5a), aggregates of tens to hundreds of nanometers in diameter are observed; at higher magnification, it is apparent that these aggregates are made of closely packed primary plates. For Al-Iprop-pre (Figure 6.5b), boehmite plates are loosely piled and form a more open structure. For Al-Sbuto-pre (Figure 6.5c), plates and fibers are observed; at higher magnification a scaffold structure is observed, consisting of plates with a length of 10-25 nm, a width of *ca.* 5-20 nm, and edges of plates (not fibers) perpendicular to the image plane of thickness of *ca.* 5 nm. For precursors rinsed and gelled with *n*-hexanol (Figure 6.5d), a loosely stacked open structure similar to Al-Iprop-pre is evident; however at higher magnification, plates of Al-Nhex-pre appear to be more connected, forming a network in which relatively large pores (30-50 nm) are observed.

It has been reported that boehmite and bayerite are layered structures linked through hydrogen bonding between surface hydroxyls.[27] When they are rinsed and gelled with surfactants, *e.g.* alcohols and amines, surfactant molecules are likely to interact with surface hydroxyls via hydrogen bonding and limit the bonding of the primary particles. Furthermore, the different stacking patterns of the nanoplates from different precursors, evident in the TEM micrographs of the precursors (Figure 6.5), are likely due to the stereo effect caused by the size of the alcohol molecules. Alcohol molecules with longer chain length may break or partially break the hydrogen bonds that hold the layers of the boehmite/bayerite crystallites and enhance their mobility and separation, rather than altering their intrinsic structure. During rinsing and gelation, these alcohol-bonded nanoplates are likely to self-orientate along certain directions, under the influence of alcohol evaporation, to reduce the overall energy of the system.

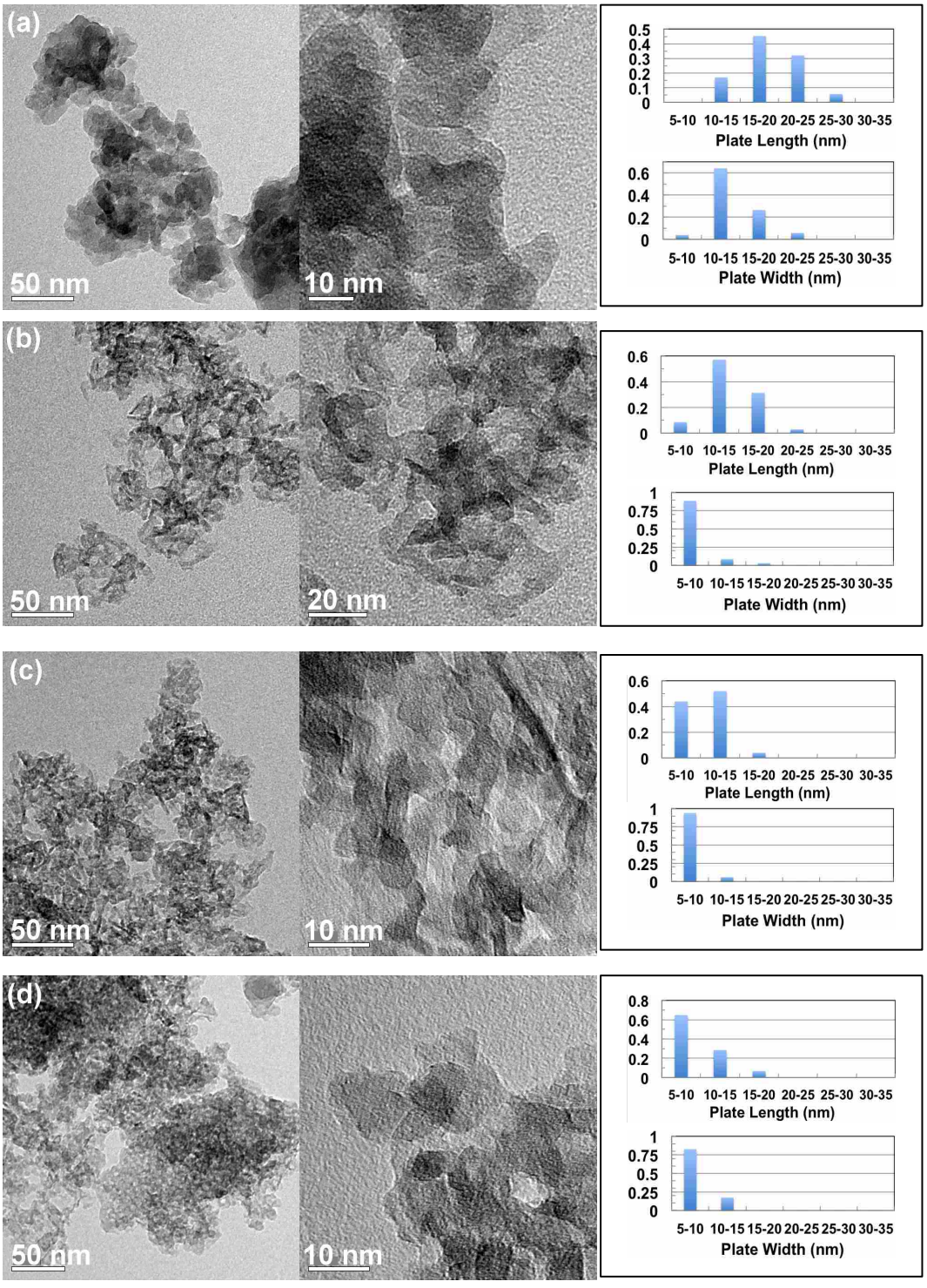

Figure 6.6 TEM images and particle size distribution of calcined γ-alumina samples rinsed and gelled with different alcohols: (a) Al-EtOH; (b) Al-Iprop; (c) Al-Sbuto; (d) Al-Nhex.

For Al-EtOH-pre, since the size of ethanol molecules is relatively small, the stereo effect is not significant. As a result, primary boehmite nanoplates are more likely to aggregate closely with each other. With longer chain alcohols (*iso*-propanol, *sec*-butanol), the stereo effect is more obvious. As observed from the corresponding precursors by TEM (Figure 6.5b and 6.5c), primary nanoplates are organized into 3-dimensional scaffold-like structures having large inter- and intra-particle voids, similar to those observed in the synthesis of mesoporous alumina in the presence of non-ionic surfactants.[19, 28] For Al-Nhex-pre (Figure 6.5d), primary plates are more separated than in other precursors. According to the DFT calculation by Digne et al,[29, 30] the hydrogen bonding between the layers of bayerite is weaker than that between the layers of boehmite. Therefore, the hydrogen bonding between Al-Nhex-pre layers are more likely to be broken by alcohol molecules. In addition, hexanol, the largest alcohol used in the study, further enlarges the distance between the primary plates.

Shown in Figure 6.6 are the different morphologies of calcined γ-alumina samples. For the calcined Al-EtOH sample, closely packed plates with a length of 15-25 nm and a width of 10-20 nm are observed (Figure 6.6a). The observation of plate-like particles is consistent with the H3 type of hysteresis observed in its corresponding isotherm (Figure 6.3a). In addition, the relatively small mesopores (7 nm) and narrow pore size distribution of Al-EtOH from N_2 adsorption can be attributed to the small interstices formed by these uniformly sized, tightly stacked plates. For calcined samples rinsed and gelled with *iso*-propanol and *sec*-butanol (Figure 6.6b and 6.6c, respectively), 3-D scaffolding structures consisting of plates with a length of 10-20 nm, a width of 5-10 nm and a thickness of *ca.* 5 nm are evident, similar to those observed in aluminas prepared via surfactant-induced fiber formation (SIFF)[31] and evaporation induced self assembly (EISA).[32] The scaffolding morphology observed in the TEM images (Figure 5b and 5c)

are consistent with large pore volumes and pore widths observed from N_2 adsorption techniques, i.e. large pore volumes arise from relatively large pores created by the voids between 3-D stacked alumina nanoplates. For the calcined sample rinsed and gelled with *n*-hexanol, a hierarchical structure made of smaller primary particles with a length and a width of 5-10 nm is observed. The primary crystallites aggregate to form secondary particles having diameters of roughly 50-300 nm, which further agglomerate to form a larger scale porous structure. The observation of hierarchical structure is in excellent agreement with the bi-model pore size distribution obtained from N_2 adsorption: small pores (6.1 nm) can be attribute to the interstice between closely packed plates, whereas large mesopores (37 nm) appear as large voids formed by secondary particles. These observations of 3-D scaffolding and hierarchical structure are similar to those of aluminas obtained using PEO surfactants[31] and triblock copolymers,[33] respectively, suggesting that alcohols act as structure-directing agents in the rinsing/gelation stage of the present preparation method.

A comparison between the TEM images of the precursor and corresponding calcined alumina samples (Figure. 6.5 and 6.6) confirms that the transformation from boehmite to γ-alumina is topotactic, i.e., the morphology of boehmite precursor is retained after calcination. However, crystallite sizes in the calcined samples have clearly changed. This is confirmed by the data in Figure 6.7 showing primary crystallite lengths and widths for precursors and calcined aluminas determined from an analysis of crystallite size distributions from TEM. For example, average crystallite length and width for the calcined γ-alumina Al-EtOH (Figure 6.7) are larger than for the corresponding precursor. For the other three calcined samples a trend of progressively decreasing length and width compared to their corresponding precursors is observed.

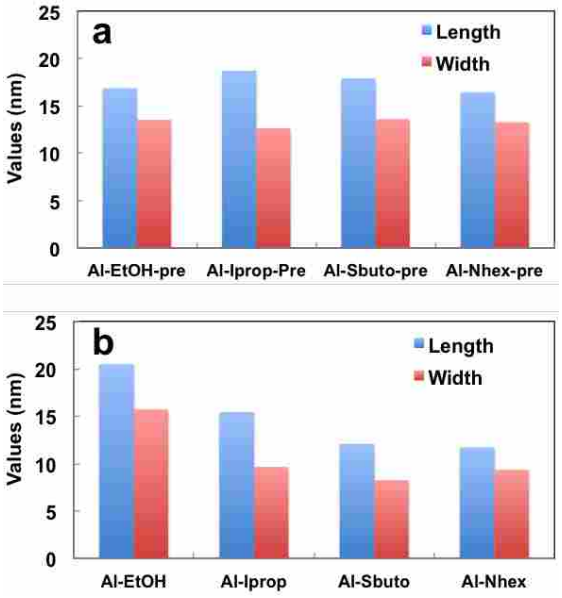

Figure 6.7 Calculated average primary plate length and width for (a) precursors and (b) calcined *γ*-alumina rinsed and gelled with different alcohols

These changes in crystallite size during calcination are likely due to a combination of (1) primary crystallite bonding and (2) shrinkage induced by dehydration, i.e., the removal of interlayer hydroxyls in the form of water and the creation of oxygen vacancies. Indeed, according to theoretical study of the dehydration of boehmite by Krokidis et al.,[34] a 30% shrinkage of the unit cell parameter *b* (supercell length) is predicted after the topotactic transformation from boehmite to *γ*-alumina. Based on the reported interlayer hydrogen bonding distances of boehmite and bayerite (0.1812 and 0.2024 nm, respectively),[30] the shrinkage is expected to be even larger for bayerite. As illustrated in the possible dehydration process shown in Scheme 6.1, after rinsing and gelation with alcohols, plates consisting of boehmite/bayerite layers are surrounded by alcohol molecules that are adsorbed on the surface of the plates via hydrogen bonding. During the calcination, interlayer hydroxyls are removed along the length and width of the supercell (approximately 7-8 by 10-11 boehmite layers for our primary plate) as water and *γ*-alumina primary plates of reduced size are formed. However, for precursors rinsed and gelled with ethanol, the interplate distance is shorter when compared to samples treated with longer chain alcohols. Therefore, adjacent plates of Al-EtOH-pre are more likely to be fused together and form larger plates. After calcination, the primary plates derived from different precursors act as building blocks to form different pore structures observed in their corresponding TEM images.

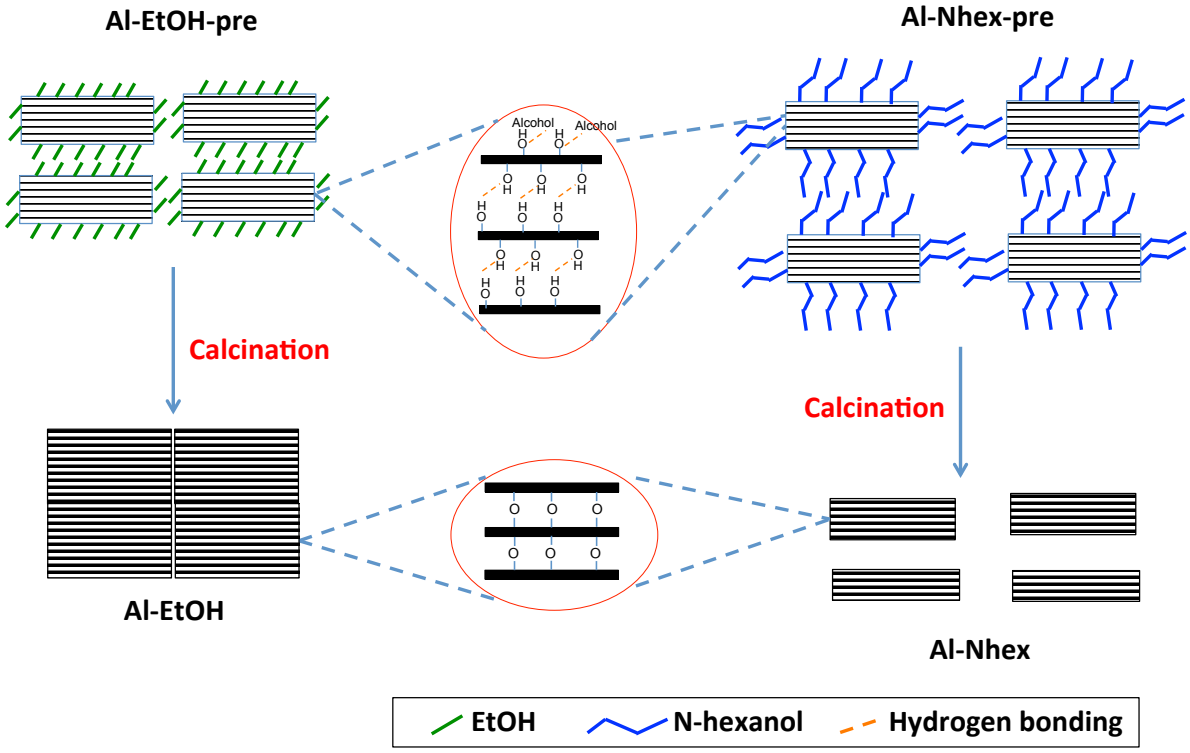

Scheme 6.1 Schematic illustration of possible calcination process.

6.4 Conclusion

In summary, γ-alumina catalyst supports with relatively high surface area (up to 260 m^2/g), large pore volume (up to 1.4 cm^3/g) and tunable pore size (7-37 nm) can be prepared by varying the alcohols used in the rinsing and gelation of boehmite/bayerite precursors obtained from controlled hydrolysis of aluminum alkoxides, These easily prepared materials with improved properties, especially the large mesopores (up to 37 nm), offer promise for a number of applications, including hydrotreating catalyst design where aluminas with different pore size ranges and/or bimodal pore size distributions are required for treatment of different feedstocks.

The results of this study also provides insight into the mechanisms of the formation of mesoporous aluminas having a variety of structures, as follows:

(1) Alcohol molecules apparently form hydrogen bonds with hydroxyls on boehmite/bayerite surfaces during rinsing and gelation and mediate the size and intergrowth of boehmite/bayerite primary crystallites.

(2) Crystallite sizes of calcined alumina samples are determined by primary crystallite bonding and shrinkage induced by dehydration during calcination.

(3) The unique mesoporous structures of precursors and corresponding calcined gamma-aluminas of this study are apparently formed by the assembly of primary plate building blocks, i.e. a particle assembly pathway.

However, further detailed experimental and computational investigations are needed to fully elucidate the mechanism of the formation of these nanostructures.

It is also should be stressed that these aluminas, as well as the ones prepared from aluminum alkoxides, it not stable in a water environment or in the presence of steam. Therefore, further stabilization of these aluminas is required to enhance their applicability in catalysis. This can be achieved by introducing dopants, such as transition metals (La, Mg, Ba) or silica materials.

References

1. Huang, B.; Bartholomew, C. H.; Smith, S. J.; Woodfield, B., Facile solvent-deficient synthesis of mesoporous gamma alumina with controlled pore structures. *Micropor. Mesopor. Mater.* **2013,** *165*, 70-78.
2. Huang, B.; Bartholomew, C. H.; Woodfield, B. F., Facile synthesis of mesoporous γ-alumina with tunable pore size: The effects of water to aluminum molar ratio in hydrolysis of aluminum alkoxides *Journal of Materials Chemistry A* **2013**. Submitted.
3. Bartholomew, C. H.; Woodfield, B. F.; Huang, B.; Olsen, R. E.; Astle, L. Method for making highly porous, stable metal oxide with a controlled pore structure. 2011-US29472, 2011119638, 20110322., 2011.
4. Mustard, D. G.; Bartholomew, C. H., Determination of metal crystallite size and morphology in supported nickel catalysts. *Journal of Catalysis* **1981,** *67* (1), 186-206.

5. Gregg, S. J.; Sing, K. S. W., *Adsorption, surface area and porosity*. 2 ed.; Academic Press: London, 1982.

6. Huang, B.; Bartholomew, C. H.; Woodfield, B. F., Improved calculations of pore size distribution for relatively large, less-ordered slit-shaped mesopore structure. *Micropor. Mesopor. Mater.* **2013**. Submitted.

7. Sayari, A.; Liu, P.; Kruk, M.; Jaroniec, M., Characterization of large-pore MCM-41 molecular sieves obtained via hydrothermal restructuring. *Chem. Mater.* **1997,** *9* (11), 2499-2506.

8. Sing, K. S. W., *Surface area determination*. Butterworths: London, 1970.

9. Cejka, J.; Zilkova, N.; Rathousky, J.; Zukal, A., Nitrogen adsorption study of organized mesoporous alumina. *Phys. Chem. Chem. Phys.* **2001,** *3* (22), 5076-5081.

10. Cejka, J.; Zilkova, N.; Rathousky, J.; Zukal, A.; Jagiello, J., High-resolution adsorption of nitrogen on mesoporous alumina. *Langmuir* **2004,** *20* (18), 7532-9.

11. Mueller, A.; Heim, O.; Panneerselvam, M.; Willert-Porada, M., Polyol method for the preparation of nanosized Gd_2O_3, boehmite and other oxides. *Mater. Res. Bull.* **2005,** *40* (12), 2153-2169.

12. Chiche, D.; Chaneac, C.; Revel, R.; Jolivet, J.-P., Size and shape control of γ-alooh boehmite nanoparticles, a precursor of γ-Al_2O_3 catalyst. *Stud. Surf. Sci. Catal.* **2006,** *162* (Scientific Bases for the Preparation of Heterogeneous Catalysts), 393-400.

13. Bleta, R.; Alphonse, P.; Pin, L.; Gressier, M.; Menu, M.-J., An efficient route to aqueous phase synthesis of nanocrystalline γ-Al_2O_3 with high porosity: From stable boehmite colloids to large pore mesoporous alumina. *J. Colloid Interface Sci.* **2012,** *367* (1), 120-128.

14. Grant, S. M.; Jaroniec, M., Effect of cosolvent organic molecules on the adsorption and structural properties of soft-templated ordered mesoporous alumina. *J. Colloid Interface Sci.* **2012,** *367* (1), 129-134.

15. Wilson, S. J., The dehydration of boehmite, γ-AlOOH, to γ-alumina. *J. Solid State Chem.* **1979,** *30* (2), 247-55.

16. Wilson, S. J.; McConnell, J. D. C., A kinetic study of the system boehmite/alumina (γ-AlOOH/Al_2O_3). *J. Solid State Chem.* **1980,** *34* (3), 315-22.

17. Du, X.; Su, X.; Wang, Y.; Li, J., Thermal decomposition of grinding activated bayerite. *Mater. Res. Bull.* **2009,** *44* (3), 660-665.

18. Sherrington, D. C.; Taskinen, K. A., Self-assembly in synthetic macromolecular systems via multiple hydrogen bonding interactions. *Chem. Soc. Rev.* **2001,** *30* (2), 83-93.

19. Hicks, R. W.; Pinnavaia, T. J., Nanoparticle assembly of mesoporous AlOOH (boehmite). *Chem. Mater.* **2003,** *15* (1), 78-82.

20. Blin, J.-L.; Leonard, A.; Yuan, Z.-Y.; Gigot, L.; Vantomme, A.; Cheetham, A. K.; Su, B.-L., Hierarchically mesoporous/macroporous metal oxides templated from

polyethylene oxide surfactant assemblies. *Angew. Chem., Int. Ed.* **2003,** *42* (25), 2872-2875.

21. Leonard, A.; Blin, J.-L.; Su, B.-L., One-pot surfactant assisted synthesis of aluminosilicate macrochannels with tunable micro- or mesoporous wall structure. *Chem. Commun. (Cambridge, U. K.)* **2003,** (20), 2568-2569.
22. Deng, W.; Toepke, M. W.; Shanks, B. H., Surfactant-assisted synthesis of alumina with hierarchical nanopores. *Adv. Funct. Mater.* **2003,** *13* (1), 61-65.
23. Cejka, J., Organized mesoporous alumina: Synthesis, structure and potential in catalysis. *Appl. Catal., A* **2003,** *254* (2), 327-338.
24. Oberlander, R., Aluminas for catalysts-their preparation and properties. *Applied Industrial Catalysis* **1984,** *3*, 63-112.
25. Wefers, K.; Misra, C., Alcoa technical paper no.19. **1987**.
26. Chiche, D.; Chizallet, C.; Durupthy, O.; Chaneac, C.; Revel, R.; Raybaud, P.; Jolivet, J.-P., Growth of boehmite particles in the presence of xylitol: Morphology oriented by the nest effect of hydrogen bonding. *Phys. Chem. Chem. Phys.* **2009,** *11* (47), 11310-11323.
27. Trimm, D. L.; Stanislaus, A., The control of pore size in alumina catalyst supports: A review. *Appl. Catal.* **1986,** *21* (2), 215-38.
28. Gonzalez-Pena, V.; Diaz, I.; Marquez-Alvarez, C.; Sastre, E.; Perez-Pariente, J., Thermally stable mesoporous alumina synthesized with non-ionic surfactants in the presence of amines. *Micropor. Mesopor. Mater.* **2001,** *44-45*, 203-210.
29. Digne, M.; Sautet, P.; Raybaud, P.; Euzen, P.; Toulhoat, H., Hydroxyl groups on γ-alumina surfaces: A dft study. *J. Catal.* **2002,** *211* (1), 1-5.
30. Digne, M.; Sautet, P.; Raybaud, P.; Toulhoat, H.; Artacho, E., Structure and stability of aluminum hydroxides: A theoretical study. *J. Phys. Chem. B* **2002,** *106* (20), 5155-5162.
31. Zhu, H. Y.; Riches, J. D.; Barry, J. C., Gamma-alumina nanofibers prepared from aluminum hydrate with poly(ethylene oxide) surfactant. *Chem. Mater.* **2002,** *14* (5), 2086-2093.
32. Brinker, C. J.; Lu, Y.; Sellinger, A.; Fan, H., Evaporation-induced self-assembly. Nanostructures made easy. *Adv. Mater. (Weinheim, Ger.)* **1999,** *11* (7), 579-585.
33. Suzuki, N.; Yamauchi, Y., One-step synthesis of hierarchical porous γ-alumina with high surface area. *J. Sol-Gel Sci. Technol.* **2010,** *53* (2), 428-433.
34. Krokidis, X.; Raybaud, P.; Gobichon, A.-E.; Rebours, B.; Euzen, P.; Toulhoat, H., Theoretical study of the dehydration process of boehmite to γ-alumina. *J. Phys. Chem. B* **2001,** *105* (22), 5121-5130.

Appendix

Computation procedures for PSD calculation based on slit-pore-geometry (SPG) model

Table A shows a excel worksheet for the computation of PSD. The procedures are described as follows:

1.Compute the Kelvin pore width x_k using Equation 1. For nitrogen as adsorbate, the surface tension γ= 8.85 × 10^{-5} N/cm. The value is record in Column 3.

$$x_k = -\frac{2*0.953}{\ln P/P_0} \qquad (1)$$

2. Compute the adsorbed layer thickness t using Equation 2. (Column 4)

$$t = 3.54\left(\frac{-5}{\ln P/P_0}\right)^{\frac{1}{3}} \qquad (2)$$

3. The amount Δt by which the adsorbed layer is thinned following a decrement in the amount adsorbed is calculated by finding the difference between successive values in Column 4.

4. Calculate the corresponding pore width x_p in Column 5 from:

$$x_p = x_k + 2t \qquad (3)$$

5. Q value in Column 9 is the conversion factor between Δv_k and Δv_p. It is defined as:

$$Q = \beta\left(\frac{x_p}{x_p - 2t}\right)$$

where β is volume structural factor.

6. $\Delta V_{liq,tot}$ in Column 12 is calculated by finding the difference between successive values in Column 11.

7. The amount desorbed due to thinning Δv_f in Column 13 is calculated by

$$\Delta V_f = \Delta A \Delta t$$

and then

$$\Delta V_k = \Delta V_{liq,tot} - \Delta V_f$$

8. ΔV_p in Column 15 is converted from ΔV_k by:

$$\Delta V_p = Q \Delta V_k$$

9. Cumulative pore volume $V_{pore,cum}$ in Column 16 is given by the previous $V_{pore,cum}$ plus ΔV_p in Column 15. For desorption, the beginning point is set to be zero.

10. The specific surface area ΔA_p corresponding to a volume ΔV_p is given by

$$\Delta A_p = \alpha \left(\frac{2 \Delta V_p}{X_{p,ave}} \right)$$

where α is the surface to volume ratio structural factor.

11. Cumulative surface area $A_{pore,cum}$ in Column 18 is given by the previous $A_{pore,cum}$ plus ΔA_p in Column 17. For desorption, the beginning point is set to be zero.

12. The maximum of $V_{pore,cum}$ and $A_{pore,cum}$ are set to match the experimental determined single point volume and BET surface area, respectively by varying the value of the two structural factor α and β. This is done by minimizing the difference between the calculated values and experimental values using Microsoft Excel Solver add-in.

13. The value in Column 23 is normalized volume density function based on the log normal distribution:

$$f = \frac{1}{(2\pi)^{1/2} \sigma} \frac{1}{D} \exp \left[- \frac{(\ln D - \mu)^2}{2\sigma^2} \right]$$

where D is the pore diameter, μ and σ are the mean value and standard deviation, respectively.

14. The value in Column 24 is the normalized experimental $dV/d\log(x_p)$ (Column 21) value.

15. RS value in column 25 is the difference between $f(\text{vol-den})_{cal}$ and $f(\text{vol-den})_{exp}$.

16. After f functions are normalized, the sum of the RS value is minimized using the Solver by varying μ and σ.

Table A. Excel worksheet for the computation of PSD based on SPG model.

1	2	3	4	5	6	7	8	9	10	11	12	13	14	15	16	17	18
P/P_0	volume	x_k	t	Δt	x_p	Δx_p	$x_{p,ave}$	Q	$n_{ad,tot}$	$V_{liq,tot}$	$\Delta V_{liq,tot}$	Δv_f	Δv_k	ΔV_p	$V_{pore,cum}$	ΔA_p	$A_{pore,cum}$
	cm^3/g	nm	nm	nm	nm	nm	nm		mmol/g	mm^3/g	mm^3/g	mm^3/g	mm^3/g	mm^3/g	mm^3/g	m^2/g	m^2/g
0.9867	1046.08	142.82	2.547														
0.9847	1042.09	123.74	2.428	0.119	128.60	17.682	137.44	0.93	46.49	1612.37	6.168	0.0000	6.168	6.168	6.168	0.0469	0.0469
0.9827	1038.05	109.31	2.330	0.098	113.97	14.634	121.28	0.93	46.31	1606.11	6.257	0.0046	6.253	6.257	12.426	0.0937	0.1406
0.9804	1033.83	96.39	2.234	0.096	100.86	13.104	107.42	0.94	46.12	1599.57	6.538	0.0090	6.529	6.538	18.963	0.1106	0.2512
0.9775	1028.19	83.57	2.131	0.104	87.83	13.034	94.35	0.94	45.87	1590.85	8.724	0.0115	8.713	8.189	27.153	0.1577	0.4089
0.9748	1023.39	74.67	2.052	0.078	78.77	9.056	83.30	0.94	45.66	1583.42	7.425	0.0124	7.412	6.997	34.150	0.1526	0.5614
0.9641	1004.42	52.08	1.820	0.232	55.73	23.048	67.25	0.95	44.81	1554.08	29.340	0.0354	29.305	27.806	61.955	0.7511	1.3126
0.9406	963.84	31.15	1.534	0.286	34.22	21.506	44.97	0.96	43.00	1491.29	62.797	0.2151	62.582	60.278	122.233	2.4350	3.7476
0.9253	933.07	24.55	1.417	0.117	27.39	6.833	30.80	0.99	41.63	1443.69	47.600	0.2847	47.316	46.768	169.001	2.7583	6.5058
0.9010	822.87	18.28	1.284	0.133	20.85	6.540	24.12	1.00	36.71	1273.18	170.508	0.3659	170.142	170.902	339.903	12.8743	19.3801
0.8763	622.81	14.44	1.187	0.097	16.81	4.034	18.83	1.03	27.79	963.64	309.539	1.2491	308.290	316.615	656.518	30.5489	49.9290
0.8498	435.44	11.71	1.107	0.080	13.92	2.887	15.37	1.05	19.43	673.73	289.909	2.4428	287.466	301.437	957.955	35.6341	85.5631
0.7984	275.15	8.47	0.994	0.113	10.46	3.468	12.19	1.07	12.28	425.72	248.013	4.0372	243.976	261.635	1219.589	38.9911	124.5542
0.7516	216.60	6.68	0.918	0.076	8.51	1.944	9.48	1.11	9.66	335.13	90.588	2.9517	87.636	97.542	1317.132	18.6843	143.2385
0.7008	180.28	5.36	0.854	0.065	7.07	1.443	7.79	1.15	8.04	278.93	56.196	1.2080	54.988	63.203	1380.335	14.7387	157.9772
0.6502	159.25	4.43	0.801	0.053	6.03	1.039	6.55	1.19	7.11	246.40	32.528	0.7769	31.751	37.724	1418.060	10.4645	168.4417
0.5998	144.55	3.73	0.757	0.045	5.24	0.787	5.64	1.23	6.45	223.65	22.754	0.4657	22.288	27.344	1445.404	8.8143	177.2560
0.5497	133.12	3.18	0.718	0.039	4.62	0.621	4.93	1.27	5.94	205.96	17.686	0.3412	17.345	21.960	1467.364	8.0900	185.3460
0.5003	123.96	2.75	0.684	0.034	4.12	0.501	4.37	1.31	5.53	191.79	14.172	0.2759	13.896	18.151	1485.514	7.5457	192.8916
0.4496	115.93	2.38	0.652	0.032	3.69	0.431	3.90	1.35	5.17	179.37	12.424	0.2403	12.183	16.417	1501.931	7.6399	200.5315
0.3996	108.86	2.08	0.623	0.029	3.32	0.365	3.51	1.39	4.86	168.44	10.929	0.2232	10.706	14.901	1516.833	7.7217	208.2532
0.3503	102.43	1.82	0.595	0.027	3.01	0.316	3.17	1.44	4.57	158.48	9.956	0.2103	9.746	14.022	1530.855	8.0474	216.3006
0.2995	96.24	1.58	0.568	0.027	2.72	0.290	2.86	1.49	4.29	148.90	9.579	0.2167	9.363	13.938	1544.793	8.8449	225.1455
0.2496	90.40	1.37	0.542	0.026	2.46	0.260	2.59	1.55	4.03	139.88	9.029	0.2303	8.799	13.596	1558.389	9.5430	234.6885
0.1998	84.71	1.18	0.516	0.026	2.22	0.243	2.34	1.61	3.78	131.07	8.808	0.2506	8.558	13.758	1572.147	10.6945	245.3830
0.1501	78.95	1.00	0.489	0.027	1.98	0.233	2.10	1.68	3.52	122.16	8.911	0.2923	8.618	14.478	1586.625	12.5290	257.9120
0.0998	72.57	0.83	0.458	0.031	1.74	0.239	1.86	1.77	3.24	112.28	9.880	0.3850	9.495	16.770	1603.394	16.3526	274.2646
0.0498	64.23	0.64	0.420	0.039	1.47	0.269	1.61	1.88	2.87	99.38	12.895	0.6300	12.266	23.012	1626.406	25.9841	300.2487

Table A. Excel worksheet for the computation of PSD based on SPG model (continued).

19	**20**	**21**	**22**	**23**	**24**	**25**
dV_p/dx_p	$\ln(x_p)$	$dV/d\ln(x_p)$	$xp*\Delta V_p$	$f(vol\text{-}den)_{cal}$	$f(vol\text{-}den)_{exp}$	RS
0.330	4.921					
0.428	4.797	50.43	757.45	0.000	0.0091	8.35E-05
0.465	4.676	50.27	655.28	0.000	0.0091	8.30E-05
0.643	4.547	63.82	773.27	0.000	0.0116	1.34E-04
0.758	4.424	56.55	583.68	0.000	0.0102	1.05E-04
1.209	4.209	129.49	1871.41	0.000	0.0235	5.43E-04
2.792	3.806	149.71	2710.92	0.006	0.0271	4.58E-04
6.871	3.427	123.37	1440.22	0.056	0.0224	1.15E-03
26.163	3.183	699.94	4121.79	0.143	0.1268	2.58E-04
78.307	2.935	1279.30	5961.84	0.238	0.2318	4.17E-05
104.555	2.732	1483.24	4632.34	0.262	0.2688	4.82E-05
75.348	2.501	1129.37	3189.07	0.204	0.2047	7.38E-07
50.230	2.249	388.44	925.04	0.101	0.0704	9.33E-04
43.796	2.053	321.45	492.35	0.043	0.0582	2.45E-04
36.332	1.879	217.49	247.14	0.016	0.0394	5.56E-04
34.687	1.729	181.98	154.04	0.006	0.0330	7.47E-04
35.369	1.596	164.46	108.29	0.002	0.0298	7.74E-04
36.210	1.475	150.28	79.33	0.001	0.0272	7.05E-04
38.032	1.362	145.44	64.09	0.000	0.0264	6.82E-04
40.887	1.254	138.63	52.29	0.000	0.0251	6.27E-04
44.448	1.152	137.33	44.35	0.000	0.0249	6.18E-04
48.039	1.052	138.67	39.89	0.000	0.0251	6.31E-04
52.400	0.951	134.80	35.21	0.000	0.0244	5.97E-04
56.780	0.849	134.84	32.14	0.000	0.0244	5.97E-04
62.092	0.742	135.00	30.40	0.000	0.0245	5.98E-04
69.972	0.622	140.29	31.21	0.000	0.0254	6.46E-04
85.714	0.476	157.09	37.05	0.000	0.0285	8.10E-04